PRE-GROWTH STRUCTURES FOR HIGH QUALITY EPITAXIAL GRAPHENE NANOELECTRONICS GROWN ON SILICON CARBIDE

A Thesis
Presented to
The Academic Faculty

by

James M. Palmer

In Partial Fulfillment
of the Requirements for the Degree
Doctor of Philosophy in the
School of Physics

Georgia Institute of Technology
December 2014

PRE-GROWTH STRUCTURES FOR HIGH QUALITY EPITAXIAL GRAPHENE NANOELECTRONICS GROWN ON SILICON CARBIDE

Approved by:

Professor Walt A. de Heer, Advisor
School of Physics
Georgia Institute of Technology

Professor Phillip N. First
School of Physics
Georgia Institute of Technology

Professor Edward H. Conrad
School of Physics
Georgia Institute of Technology

Professor Ramesh Mani
Department of Physics and Astronomy
Georgia State University

Professor Zhigang Jiang
School of Physics
Georgia Institute of Technology

Date Approved: 6 November 2014

Dedicated to Heather.

ACKNOWLEDGEMENTS

I want to offer the following people my sincerest appreciation and a heartfelt *thank you!* I did not arrive to the end of this program on my own. I would not have even begun on my own, but now I truly appreciate the experiences I have had.

Foremost, Heather, who risked coming out here with me and was by my side this entire time. I can't think a more patient person. Of course, to my parents, who are supportive of my attempts to educate myself – both now in a school and as a child doing experiments in a bedroom that could have burnt down. I appreciate the friendly help of the School of Physics staff, who kept our lab functioning. I appreciate all the help from my peers, Dr. Ming Ruan, Dr. Yike Hu, Dr. Jan Kunc, Dr. Lei Ma, Dr. Rui Dong, Dr. Jeremy Hicks, Dr. Zelei Guo, John Hankinson, and Jean-Philippe Turmaud. I also appreciate the help of the IEN cleanroom staff, particularly that of Devin Brown.

Thanks to my grandfather, Thomas Wilkinson, for encouraging me specifically to study physics, as well as having innumerable other conversations about technology. Thanks to Prof. Agnolet for insisting I go to graduate school, especially at a different school. It was worthwhile and and I have grown as a person for it. Thanks to the other faculty in the School of Physics, Professors Ed Conrad, Phil First, and Zhigang Jiang for their help throughout my research.

My appreciation especially goes out to my advisor, Prof. Walt de Heer, for inviting me to be part of an interesting environment. My thanks to him for being having the door open and being accessible. My thanks goes also to Dr. Claire Berger, for all her assistance in the laboratory and for editing my prose. Many thanks to them for their patience as I found my bearings.

TABLE OF CONTENTS

LIST OF TABLES

LIST OF FIGURES

SUMMARY

For graphene to be a viable platform for nanoscale devices, high quality growth and structures are necessary. This means structuring the SiC surface to prevent graphene from having to be patterned using standard microelectronic processes. Presented in this thesis are new processes aimed at improving the graphene as well as devices based on high quality graphene nanoribbons. Amorphous carbon (aC) corrals deposited prior to graphene growth are demonstrated to control SiC step-flow. SiC steps are shown to be aligned by the presence of the corrals and can increase SiC terrace widths. aC contacts deposited and crystallized during graphene growth are shown as a way to contact graphene without metal lift-off. Observation of the Quantum Hall Effect demonstrates the high quality of the graphene grown alongside the nanocrystalline graphite contacts. Continuing the ballistic transport measurements on sidewall graphene nanoribbons, the invasive probe effect is observed using an atomic force microscope (AFM) based technique that spatially maps the invasive probe effect. Cleaning experiments demonstrate the role of scattering due to resist residues and environmental adsorbates on graphene nanoribbons. Finally, switches based on junctions formed in the graphene nanoribbons are shown as a route toward graphene based devices.

CHAPTER I

INTRODUCTION

This thesis explores graphene, a topic at the confluence of several fields: electronic transport, surface science, and materials science, all working towards improved electronic devices. Modern technology, and research, requires integrating knowledge from all of these disciplines. This includes seeking higher device integration densities as a part of the push for following Moore's law. Other applications include higher operating speed transistors or other niche applications for extreme operating conditions. Attempts to provide a platform for answering basic questions about the electronic transport in graphene devices, particularly graphene nanoribbons, are covered by this thesis and this thesis attempts to show new direction for graphene based electronics.

1.1 Nanoelectronics

New electronic systems are being very actively developed to push Moore's law forward. Toward this end smaller and faster devices are broadly desired, as outlined by the International Technology Roadmap for Semiconductors[1]. As of 2014, the 14nm process node in Si-based microprocessors has reached state-of-the-art in mass production. By 2020 semiconductor device technology is expected to arrive at the 5nm, if the industry is able to keep up economically. Beyond ever-increasing device densities, higher operating speeds and lower power consumption in these processors are actively developed in a world that wants to do more with less power. Devices capable of operating in extreme conditions are sought after as well. Fundamental understanding of the physical mechanisms in small devices is critical to improving device engineering.

Conversely, development of micro- and nanoelectronics have revealed fundamental

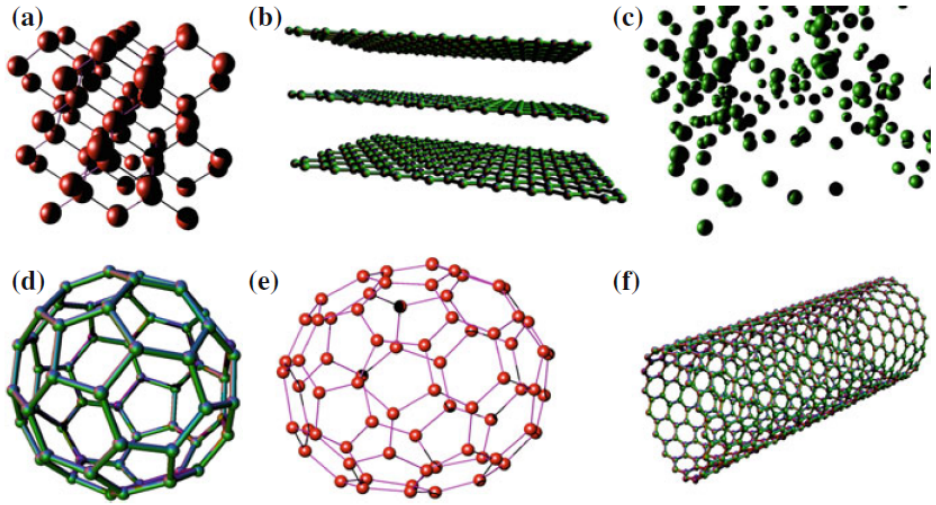

Figure 1: Well-known allotropes of carbon. (a) Diamond (b) Graphite (c) amorphous carbon (d) C_{60} fullerene (e) C_{70} fullerene. (f) Single-walled carbon nanotube. Reprinted from [3].

mechanisms of condensed matter physics[2]. Low-dimensional electronic transport is a good example of these effects. For examples, consider the quantum hall effect and mesoscopic transport. Much work in two-dimensional electron gases (2DEGs) has been done on GaAs and silicon MOSFETs. Atomic wire-like channels, like carbon nanotubes, show ballistic conduction through few conducting modes. Early studies of zero-dimensional like systems showed the presence atom-like behavior, as well as Coulomb blockade effects in small transistors, as well as molecular channel devices. Perhaps the best distinction between micro- and nanoelectronics is that quantum behavior is ever more dominant in nanoscale devices.

Carbon is a material that exhibits 0D, 1D, and 2D low-dimensional structures, in addition to bulk forms [3], as shown in Figure 1. Interest in the electronic properties of carbon began with bulk diamond, amorphous carbon, and graphite structures, which carried on through much of the 20^{th} century. However, the bulk allotropes were not considered for electronics. Diamond was not because of its large bandgap, low natural abundance, and expensive commercial production. Graphite, although useful as a refractory electrode and for nuclear reactor applications, was not considered

useful for electronics because as a semimetal it cannot be switched off-and-on like a semiconductor.

The attitude towards carbon changed as low-dimensional nanoscale allotropes of carbon were experimentally realized. Famously, C_{60} fullerenes, as a 0D carbon structure, were announced in 1985[4]. Carbon nanotubes, a 1D carbon structure, became more popular in the 1990's, beginning with an announcement by Ijima[5]. Carbon nanotubes may be thought of as a rolled-up graphene sheet, and this treatment is often used in electronic structure calculations of graphene. Much work has been done to create electronic devices from the nanotubes, but their synthesis and one-dimensional character present fundamental difficulties in their processing. This sets the background for studying graphene, where carbon structures and nano-electronics are studied together.

1.2 Graphene

At the time of writing of this thesis, graphene is now a very well known material. The last ten years of condensed matter research has seen advances in understanding its unique electronic transport properties. Graphene, being the primitive layer of graphite, has many connections with the science of graphite[6, 7]. Graphite is considered the most stable solid at standard laboratory conditions, having a melting point at 3000°C, which is attributable to the stability of its covalent sp^2 bonds. Relative to metals this means increased structural stability, but with a good conductivity. Typical metals, like gold, have a resistivity of $2\mu\Omega$cm, whereas graphite, depending on its purity, has a resistivity around $4000\mu\Omega$cm at 300K. Intrinsic germanium (E_{gap}=0.8eV) has a resistivity $4.5\times10^5\mu\Omega$cm at room temperature, and silicon (E_{gap}=1.12eV) has a resistivity around $2.3\times10^7\mu\Omega$cm at room temperature. Graphite, as a semimetal, has a resistivity between the metals and semiconductors.

Graphene as an electronically distinct material began to gain more appreciation

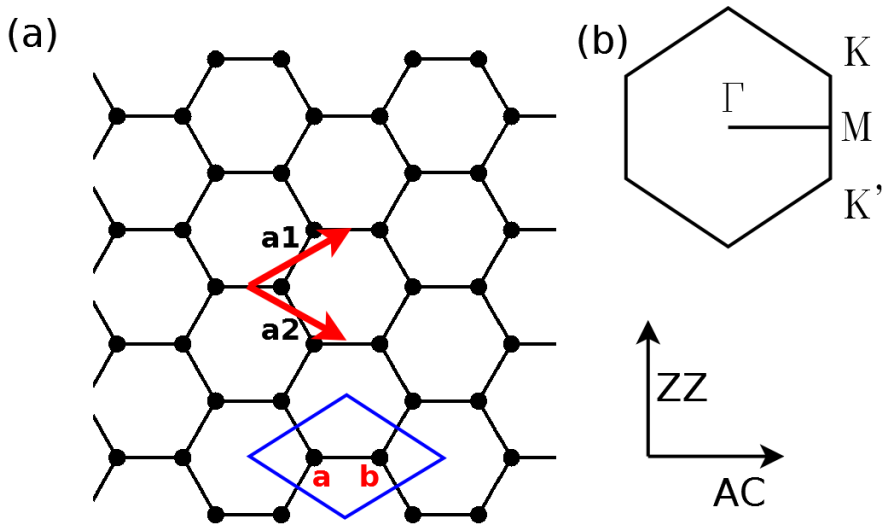

Figure 2: (a)The graphene lattice, defined by primitive vectors $\mathbf{a_1}$ and $\mathbf{a_2}$. Graphene's Wigner-Seitz primitive cell is outlined in blue. The axes define the zigzag (ZZ) and armchair (AC) directions of the graphene edge-termination. (b) The first Brillouin zone of graphene.

in the 1990's, when work was done on carbon nanotubes. Calculations on carbon nanotubes are based on the electronic structure of graphene, since carbon nanotubes may be thought of as rolled-up graphene. The π orbitals out-of-plane are electronically active, not the sp^2 in-plane bonds. See Figure 2 for an illustration of the lattice structure of ideal graphene. The graphene lattice is often called a honeycomb lattice. It has a basis of two atoms, the A and B sublattices.

The electronic structure of graphite was known as far back as 1947 from a tight-binding calculation [8]. Interestingly, a simple tight-binding calculation of the π electrons captures the essential electronic structure of ideal graphene. The nearest-neighbor interaction between the a and b atoms is what is considered here to obtain the essential electronic structure of graphene. See Figure 3 for plots of the electronic dispersion in ideal graphene. Within a single graphite layer the nearest-neighbor tight-binding solution takes the form:

$$E(\mathbf{k}) = \pm\gamma_1\sqrt{1 + 4\cos^2(\frac{k_y a}{2}) + 4\cos(\frac{k_y a}{2})\cos(\frac{\sqrt{3}k_x a}{2})} \tag{1}$$

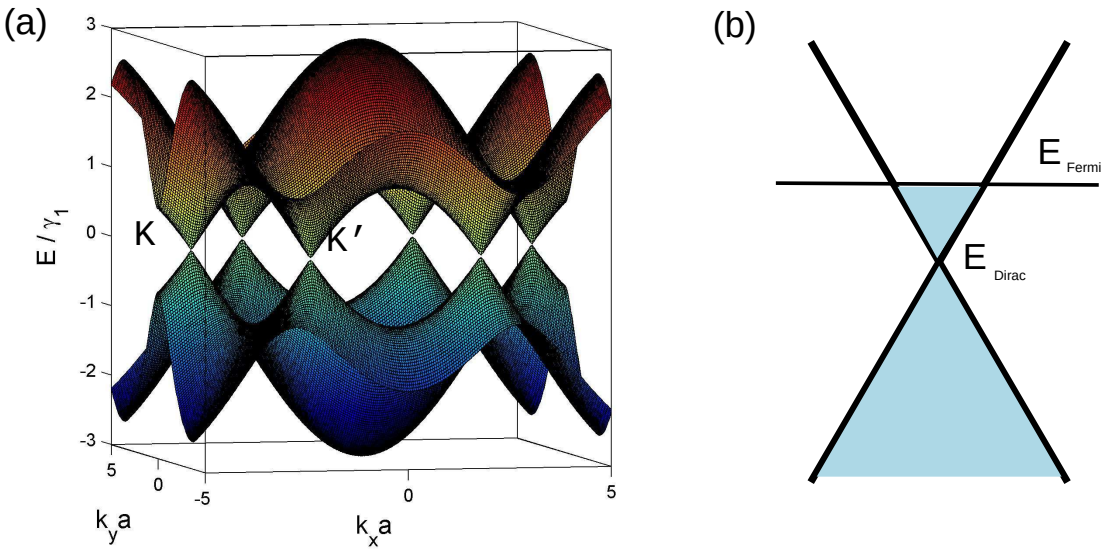

Figure 3: (a)Energy dispersion of the graphene π bands. (b)Illustration of the linear expansion of the energy dispersion around one of the K-points.

If this expression is expanded around one of the K-points you have this linear relationship:

$$E(\mathbf{k}) = \hbar v_F |\mathbf{k} - \mathbf{K}| \tag{2}$$

This linear expression of the electronic structure, valid at low energies, is what fundamentally sets graphene apart from graphite. Graphite has interlayer interactions that break the sublattice symmetry of graphene. The K-point in the graphene Brillouin zone is commonly referred to as the Dirac point, as the physics of linear band structure parallel that of relativistic particles described by the Dirac equation, rather than massive particles. The speed of the charge carriers, defined by $v_F = \frac{1}{\hbar}\frac{\partial E}{\partial k}$, is around $1{\times}10^8$cm/s[9]. The Fermi velocity in ideal graphene is unique because it does not change with energy, unlike in materials which have a parabolic energy dispersion. The density of states derived around the K point is given by:

$$N(E) = \frac{2|E - E_{Dirac}|}{\pi \hbar^2 v_F^2} \tag{3}$$

As can be seen from the linear expansion of the energy dispersion, graphene has a

low density of states at the Dirac point, as described by (3). The vanishing density of electronic states at the Dirac point gives the graphene its semimetallic character. It is conducting, like a metal, but its density of states is also tunable by the field effect, like a semiconductor.

One consequence of the wavefunctions peculiar to charge carriers in graphene is their property of pseudospin (also commonly known as isospin or chirality), which is related to the A and B sublattice symmetry. Pseudospin, like electronic spin, is a conserved quantity that can have a profound effect on interactions. Graphene pseudospin most noticeably prevents backscattering processes. This is one reason for graphene's higher electronic mobilities. Scattering processes typically must happen over a very small distance, on the order of the lattice constant, in order to scatter a charge carrier from one K sublattice to another.

Experimental evidence for pseudospin was first discussed for graphitic materials and indicated in carbon nanotube measurements [10, 11]. For graphene, evidence of pseudospin was found in epitaxial graphene on SiC[12]. Beyond pseudospin, graphene has other electronic properties that are very unique. Going beyond low charge density, the nature of the transport at zero charge density is very interesting and still subject to much debate. There are discussions of Fermi velocity renormalization. See the review by Das Sarma et al. for more about low charge density graphene[13].

1.3 Electronic Transport

Before describing production of graphene, particularly EG on SiC, in further detail, this section is intended to describe the electronic properties relevant throughout this thesis. Electronic transport in two-dimensional graphene follows the general approach for two-dimensional electron gases (2DEG's). In Chapter IV of this thesis I will spend more time discussing transport in one-dimensional graphene systems as pertaining to sidewall graphene nanoribbons.

1.3.1 Semiclassical Model of Conduction

A simple model for conduction in a solid is the Drude model[14]. The essence of the Drude theory is that there is some velocity distribution for charge carriers in an electric field, determined by the thermal and scattering processes affecting the charge carriers. This distribution we characterize by its average velocity. To first-order we may say the velocity is proportional to the applied electric field:

$$\mathbf{v_{average}} = \mu \mathbf{E} \tag{4}$$

We call μ the electronic (or hole if holes dominate the transport) mobility of the charge carriers in the conductor. We may define the current density in a solid to be equal to the integral charge of the carriers times the density of the carriers and their velocity. Therefore, Ohm's law is written:

$$\mathbf{J} = \rho \mathbf{v} = \sigma \mathbf{E} = q n_s \mu \mathbf{E} \tag{5}$$

where n_s is the sheet charge density and q is the carrier charge. To learn more about either the carrier mobility or the carrier density, measurement of the transverse resistance can be made in addition to the longitudinal resistance[15]. This is called a Hall effect measurement. The preferred geometry for this measurement is the Hall bar, as shown in Figure 4, where both transverse and longitudinal resistances may be measured simultaneously. The Hall bar is defined by its width W and length L. We find that the measured longitudinal resistivity is $\rho_{xx} = (V_{34}/I_{12})W/L$ is given by Ohm's law for 2D systems. We call W/L the *aspect ratio* of the channel. The transverse resistance, call the Hall resistance, is proportional to the applied magnetic field B. The key to understanding the transverse resistance it is to apply Newton's law to the charge carriers:

The carrier density can be determined from the off-diagonal resistance, measured by transverse contacts as in Figure 4. We call this the Hall resistance, and classically

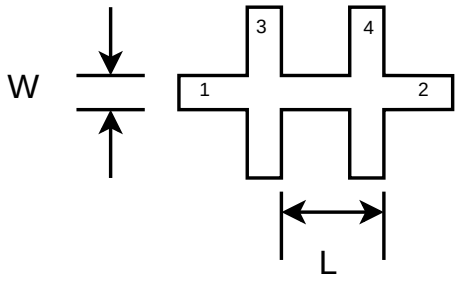

Figure 4: A basic hall bar sample configuration of width W and length L. Current is sent between contacts 1 and 2. The longitudinal voltage is V_{3-4}. The Hall voltages are either V_{3-5} or V_{4-6}.

it is a linear in B. With n_s determined from the Hall resistance, the sample mobility may then be separated from the measured conductivity. From ρ_{xx} the mobility for massive particles is related to the effective mass of the charge and its *scattering time*, τ:

$$\mu = \frac{qn_s\tau}{m^*} \tag{6}$$

The scattering time is interpreted as the average time between scattering events for the charge carrier. Of course, as I took the time to explain in section 1.2, charge carriers in graphene are massless. How then do we relate the scattering time and mobility for graphene? The answer is to write the conductivity in terms of the density of states at the Fermi level $N(E_F)$ and the charge carrier *diffusivity,* $D = v_F^2\tau/2$:

$$\sigma = e^2 N(E_F) D \tag{7}$$

Using (5) and (7), the mobility can be written:

$$\mu = \frac{ev_F\tau}{2\sqrt{\pi\hbar n}} \tag{8}$$

What is immediately clear from this relation is that, with all other parameters constant, the mobility explicitly depends on the charge carrier density, i.e. $\mu \propto 1/\sqrt{n}$. This means that any mention of graphene's mobility must be referenced to a charge density, if any material parameter such as scattering time τ or carrier mean-free-path $\lambda = v_F\tau$ is to be extracted.

The discussion and interpretation of this electronic transport data has surrounded much of the graphene literature. While the Drude model gives a basic understanding of the transport, solutions to the Boltzmann equation are required for a more comprehensive understanding of classical electronic transport, which is beyond the scope of this work[14, 16]. To include quantum effects requires other formalisms, especially to explain effect like the Quantum Hall Effect[17, 2]. Scattering rates are a defining electronic characteristic of a material, and their understanding is necessary for developing better sample growth or production.

1.3.2 Total scattering rate

From the Hall effect measurements alone we have some ideas of the total scattering rates. Based on Matthiessen's law we can separate scattering due to various effects[14]. Using the carrier mean free path λ, we may for example write:

$$\frac{1}{\lambda_{MFP}} = \frac{1}{\lambda_{impurities}} + \frac{1}{\lambda_{phonon}} + \frac{1}{\lambda_{LER}} \tag{9}$$

Included in this list are common scattering sources: impurities, phonons. Phonons are a source of scattering that is intrinsic to the material, i.e. they are present even in the perfect crystal. Once source of scattering that is particularly important to the topic of graphene nanoelectronics is line edge roughness scattering (LER)[18, 19]. LER from top-down patterned and etched graphene nanoribbons shortens λ_{MFP} to a few nanometers, leading to localization within the nanoribbons and poor mobilities.

If more information about the individual scattering processes is needed, then each process must be separated. The most common scattering mechanism to be probed is the phonon modes. Phonons are thermally activated, and as such can be removed (or introduced) by varying the sample's temperature. Commonly this is done with a cryogenic system to freeze out phonons. Impurity limited scattering may only be varied by changing the quality of the samples or doping density of the sample. Surface adsorbates on graphene have also been studied extensively.[20, 21] Finally,

LER scattering can be understood by varying the width of the nanoribbons since the bulk-to-edge ratio is affect by the width.

1.4 Graphene Production

This sections begins with a brief review of methods of producing graphene. Popular methods for synthesis of graphene have included chemical exfoliation[22], mechanical exfoliation (The "Scotch Tape" method), Chemical Vapor Deposition (CVD), metal-surface epitaxy, as well as thermal decomposition of SiC [23]. This thesis is about epitaxial graphene on SiC (EG on SiC), which as I will discuss has many advantages.

1.4.1 Exfoliation

Mechanical exfoliation is a technique that was suitable for basic electronic transport experiments in graphene, as more advanced to grow graphene were being developed. Exfoliation is feasible due to the layered structure of graphite and the weak van der Waals bonding between layers. A sample of highly oriented pyrolitic graphite (HOPG) is taken and adhesive tape is used to successively cleave and deposit layers of graphite/graphene onto a substrate. Silicon dioxide (SiO_2) has been preferred because phase-contrast optical microscopy enables detection of monolayers. The ability to produce high mobility samples led to its popularity. [24] Advances in the exfoliation method came about by improving the substrate that the graphene flakes were exfoliated onto. Silicon dioxide is not an ideal substrate due to a rougher surface and charge/impurity trapping. Graphene on boron nitride (BN) was found to be a better alternative. [27]. BN and graphene have very similar lattice constants and BN forms a very flat and clean interface to graphene, enabling very high carrier mobilities.

It is even possible to remove the effect of a substrate entirely, although unscalable mechanical exfoliation is still required. Philip Kim's group did this with suspended graphene[28, 25]. This is possible by chemically etching the silicon dioxide substrate beneath the graphene. The graphene remains attached to the contacts after etching

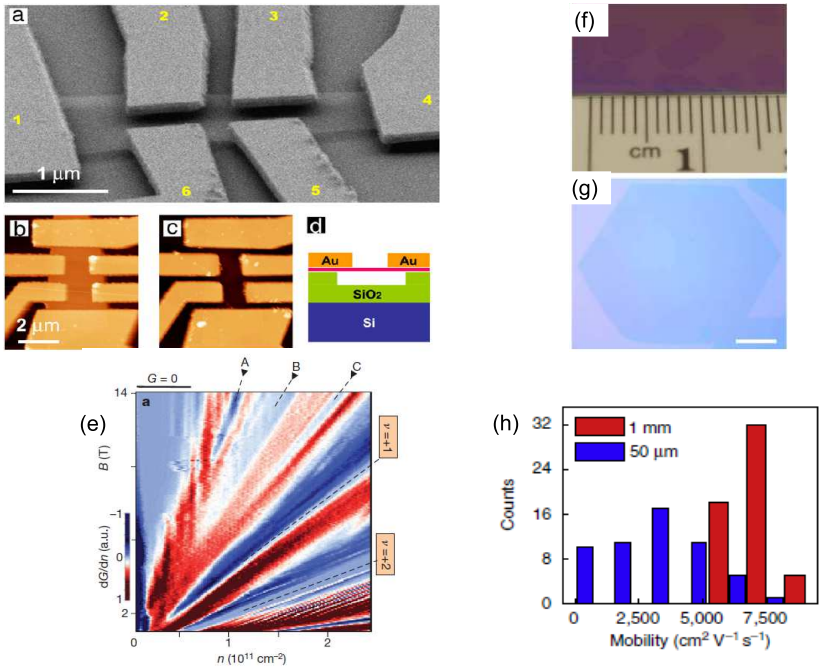

Figure 5: Examples of graphene. (a)-(d): Suspended graphene from Kim's group[25]. (e) Measurement of the fractional quantum Hall effect on suspended graphene (f)-(g): Optical images of millimeter-sized CVD on copper graphene. Images reprinted from [26] (h) Histogram of mobilities measured on the millimeter-sized CVD graphene.

by adhering to the metallic contacts. See Figure 5 for images of suspended graphene by Kim's group. They were able to observe the Fractional Quantum Hall state in these samples, which is an indication of electron-electron interactions and the high quality of the samples.

Attempts to scale the exfoliation of graphene flakes have been confined to ultrasonically and chemically induced methods. Repeated ultrasonication in a series of chemical baths is capable of producing small graphene platelets. However, the purity and ability to structure the locations of the samples is still not as good as CVD or epitaxial growth[29].

1.4.2 Chemical Vapor Deposition

Chemical Vapor Deposition (CVD) is a popular graphene growth method, rather than extracting from a bulk sample. Early results stemmed from production of graphene by diffusion of carbon through metal substrates, particularly, Ni[30, 31]. These experiments involved the carbon dissolve into solid Ni. This led to deposition of precursor gases on Ni [32, 33], which were found to have better growth control. However, since carbon is so soluble in Ni, to reliably grow a monolayer requires very fast cool-down rates.

Carbon is not as soluble in copper, and CVD methods based on copper are also available[30, 34]. Gas precursors, typically a hydrocarbon like methane, are flowed over a copper substrate around 1000°C. Various precursor sources have been used now. Basically any organic substance, such as sugar or an insect, has been used to demonstrate the point [35]. Optimization of the growth process has led growth of large single-crystal domains, up to 5mm in size [26] See Figure 5 for images of the large graphene domains.

For transport applications the CVD-grown graphene must be transferred to an insulating substrate. The most popular graphene transfer method to date, developed

at MIT [36], requires spin-coating PMMA (e-beam resist) and etching the copper substrate away with nitric acid. While this is convenient, it requires exposure to organic adsorbates and the oxidizing nitric acid.

1.5 Epitaxial Graphene on Silicon Carbide

Graphene on SiC has many advantages and will be the focus of my thesis, and so here I quickly review some facts about EG, though the space I have taken does not portray the depth and variety of the field. Graphitization of SiC at high temperatures was observed by Acheson[37] around the beginning of the 20^{th} century. Van Bommel found evidence for thin graphite layers using LEED on the Si-terminated (0001) face of SiC heated about 1000°C in UHV [38]. This work was followed in the 1990's by Forbeaux. Forbeaux studied the graphitization process further[39], and using inverse photoemission spectroscopy measured a graphite-like π^*-band energy dispersion. Growth of EG on SiC intended for electronic transport devices was first done at Georgia Tech starting in 2001, and the diffusion-limited Confinement Controlled Sublimation method was developed in 2004.[40] An alternative diffusion limited growth method based on argon pressure has been used by other research groups, but is not used in my work[41].

What is significant about the CCS method of graphene growth is that the graphene growth occurs nearly at thermodynamic equilibrium, as opposed to the UHV growth method. This means that the carbon atoms have more time to assemble into larger defect-free sheets. The near-equilibrium growth also requires elevated temperatures, typically at 1400°C or as high as 2000°C depending on the Si vapor pressure. CVD growth on copper or UHV growth on SiC occur between 1000°C and 1200°C. Depending on the pressure, higher growth temperatures allow greater growth kinetics and thus defect densities are expected to be lower.

EG on SiC has the advantage of graphene preparation directly on a well-ordered and insulating substrate. EG on SiC can be integrated with Si [42] electronics as

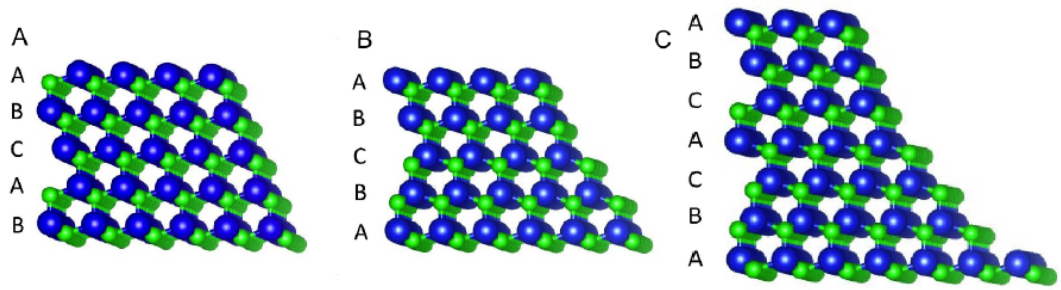

Figure 6: SiC polytypes, taken from [49] The polytypes represented are (a) 3C-SiC (b) 4H-SiC (c) 6H-SiC. 6H and 4H are by far the most commonly used polytypes, followed by 3C.

well as SiC electronics [43, 44]. Very long spin diffusion lengths are observed with EG on SiC. [45] High transconductance transistors and integrated circuits have been produced[46, 47], again showing its capacity for high quality electronics.

1.5.1 Silicon Carbide

SiC itself is a crystal of interest, with much research concerning high-power density devices and high temperature capable devices[48]. Standard hexagonal SiC morphologies are assembled into C-Si bilayers that are 2.5Åthick. Due to the bilayer structure there are two main polar faces, the Si terminated face (0001) and the carbon terminated face $(000\bar{1})$. There are over 200 polytypes of SiC known, made possible by many different stacking orders of the bilayers. This thesis exclusively uses 4H and 6H SiC, as those are the two most common polytypes. See Figure 6 for a diagram of the SiC unit cells.

For many surface studies, conducting SiC is preferred as a path to ground for incident radiation or for electronic currents. Typical conducting SiC is available in n-doped form with nitrogen doping densities around 10^{17}cm^{-3}. However, for transport studies it is important to have an insulating substrate. 4H- and 6H-SiC have a electronic energy gap of about 3.3eV. Since the band gap is fairly large and there are few electronic states in the band gap, the Fermi level can shift towards either the

valence or conduction bands depending on impurity concentrations, resulting in lower resistivities than desired, especially if graphene devices that are to be turned off are made on the surface. Typical impurities are nitrogen and boron, with background densities in the 10^{15}cm^{-3} range.

SiC wafers available from CREE corporation are available up to $10^{9}\Omega$cm resistivity using a defect-level method to pin Fermi level in the gap. Vanadium compensated SiC, available from II-VI corporation is also desirable for a semi-insulating substrate[48]. The vanadium trap states can act as either a charge acceptor or donor, and its density is not changed by graphene growth temperatures. V-doped SiC is more insulating than defect pinned SiC, with a typical resistivity of $10^{11}\Omega$cm.

1.5.2 Silicon Face Graphene

Much of the literature on EG on SiC has focused on Si-face (0001) graphene, which has a slower growth rate. It is not known why the growth rate on the Si-face is slower. Graphene layers on the Si-face are AB(Bernal) stacked, meaning that many layers on the Si-terminated face are electronically like graphite, as previously discussed.

A buffer layer forms on the silicon terminated face below the first electronically active graphene layer. This is also referred to as an interface layer and it forms at a lower temperature than the first graphene layer. More will be said about the buffer layer in Chapter 5. The highest electronic mobilities measured on the Si-face are around 10,000cm^2/V·s at charge densities between 10^{11} and 10^{12}cm^{-3}.[20, 21]

The graphene on both faces is known to drape over the steps and sidewalls on the surface of the SiC. This is directly confirmed by STM imagery. [50] Graphene that is draped over the sidewall steps can be electronically different from the buffer layer. This provides the technique of sidewall nanoribbon growth [51], which is discussed in more detail in Chapter IV. Semiconducting states have been observed in ARPES on the bent portion of the graphene on the step edge.[52] The first observation of the

quantum Hall effect was on Si-face graphene[53], followed by the C-face[54].

1.5.3 Carbon Face Graphene

As mentioned previously, graphene grows faster on the carbon face, which means that multiple layers are easier to grow. See Figure 7(b) (c) and (d) for images of C-face graphene. Rotationally stacked layers on the C-face are in fact multiple graphene layers, due to the preservation of graphene's A-B sublattice symmetry, which is altered by Bernal stacking.[55]

The growth mechanism for MEG rotational stacking forming versus A-B stacking on the Si-face are still not known. It is known that arbitrarily many layers can be produced on the C-face, with films having over 100 layers having been produced at the time of this thesis. Several or more layers of carbon face graphene are also known to have pleats (also called puckers or ripples, see Figure 7(d))[50]. The pleats are formed because the SiC has a greater thermal coefficient of expansion than the graphene, causing the graphene to gather as pleats as the EG on SiC cools after growth. Low Energy Electron Diffraction (LEED), a surface sensitive structural measurement, is used to characterize the graphene and it confirms the rotational stacking of the graphene, as shown in Figure 7(b) by the arcs[56]. STM experiments show interesting moiré effects on the rotated graphene layers[57]. Interaction between commensurate graphene layers produces new periodicities in the electronic structure, seen as moiré patterns.

The CCS growth method has a high enough Si vapor pressure to slow down the growth so that monolayers on the carbon face can be reliably grown[58], which is not possible with other growth methods. Electron mobilities exceeding 40,000$\mathrm{cm}^2/\mathrm{V}\cdot\mathrm{s}$ have been measured on carbon face[59, 54] monolayers and multilayers, with charge density as low as $5\times10^9\mathrm{cm}^{-2}$ within multilayer graphene. High frequency operating

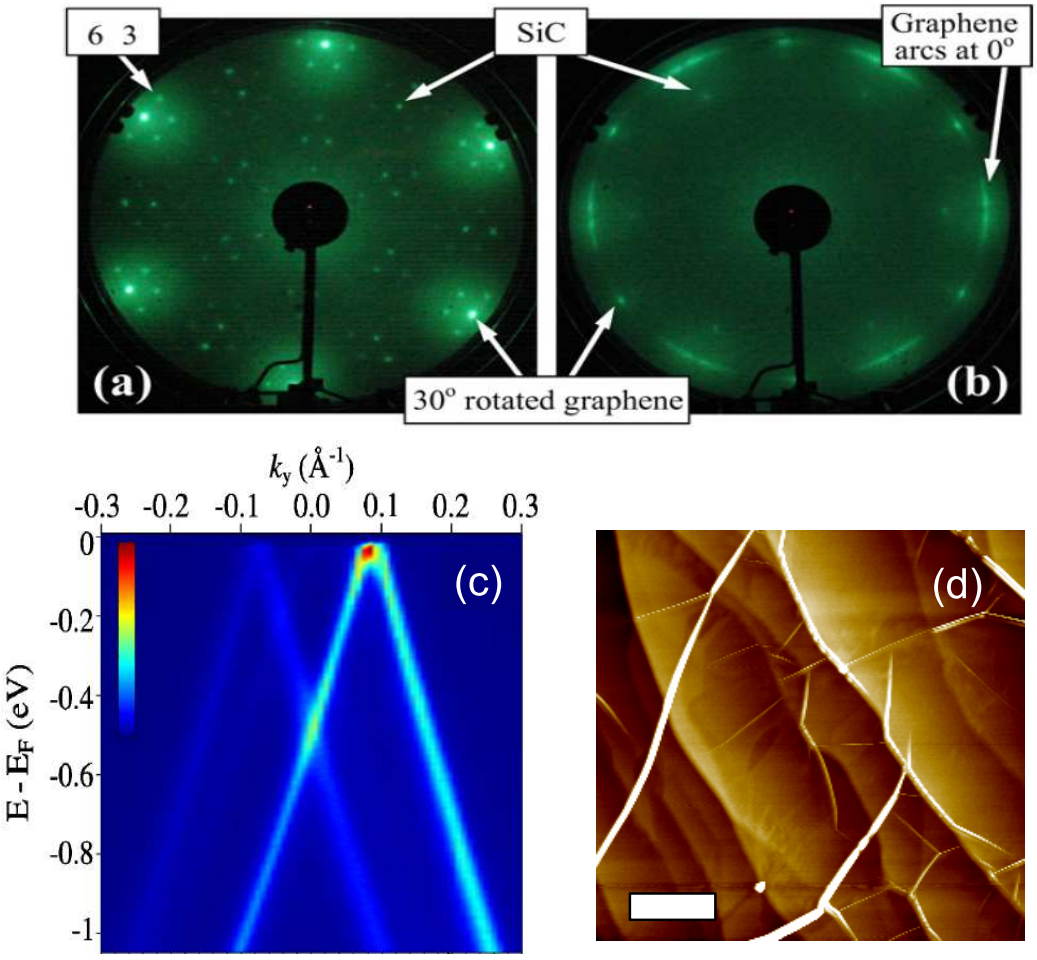

Figure 7: (a) LEED from Si-face graphene (b) LEED from C-face multilayer graphene. (c) ARPES taken on MEG, taken from [55] (d) AFM image of several-layer C-face graphene, showing graphene pleats traversing SiC steps. The scale bar is 2μm.

graphene RF transistors are also made on C-face monolayers with world record maximum oscillation frequencies f_{max}[60]. The mobility is thought to be higher because of the lack of a buffer layer on the C-face.

The charge density for graphene on both faces of the SiC is typically 0.1 to 1x10^{13}cm^{-2}. This is normally attributed to charge-transfer due to differing work functions between the graphene and the SiC. The spontaneous polarization of the SiC itself has also been thought to partially responsible for the intrinsic doping of the graphene on SiC. [61].

1.6 Thesis Outline

In Chapter II the main experimental tools, including characterization tools, growth and processing tools, as well as electronic transport are discussed as the experimental background for the rest of the thesis. In Chapter III, I present evaporated amorphous carbon as a new material that is useful for graphene growth. As I will show, the carbon may used as a step-flow barrier or as a robust contact to the graphene. In Chapter IV, I study the processing of sidewall graphene nanoribbons and conclude that these ribbons must be protected from resist residues and environmental exposure. I also develop a new kind of microscopy to based on the invasiveness of a voltage probe on a graphene nanoribbon. Finally, in Chapter V I present two methods to produce switches based on epitaxial graphene, either by growing the buffer layer between two graphene contacts or by placing a tunnel barrier in between two sidewall graphene nanoribbons.

CHAPTER II

GRAPHENE GROWTH, CHARACTERIZATION, AND DEVICE FABRICATION

This chapter describes the most important fabrication procedures and measurements in detail as background information for the rest of this thesis. Many graphene procedures build on standard microelectronic procedures, and as such standard microelectronic tools can be used. Almost every measurement or process tool used is maintained by myself and my group in the School of Physics. The graphene furnace and contact mask aligner I personally set up for use in the research presented in this thesis. A few process tools maintained by the Georgia Tech Institute for Electronics and Nanotechnology (IEN) were also used in this thesis, as I will mention.

A key distinction in the processing of graphene is that the conducting channel is exposed on the surface. This means that any process step has to done in a way that will not unnecessarily damage the graphene or leave undesired residues on its surface. However, in contrast to buried conducting channels the advantages to having the channel exposed are that the channel is easily accessed for surface measurements, it is easily modified, and the channel is lithographically defined. Lithographic definition, as opposed to electrostatic, is advantageous because fewer biasing potentials are needed to define the conducting areas.

2.1 Graphene Furnace Design

This section is to introduce the graphene furnace system I built and used for most of the samples in this thesis. This generation of furnace design reduces the complexity of the growth environment, with the new design aimed at improving the reliability of

Table 1: Measured power compared with measured temperature, the power output expected from the Stefan-Boltzmann law, as well as the wavelength predicted by Wien's law.

T[°C]	P_{S-B}[W]	$P_{measured}$ [W]	$\lambda_{Wien}[\mu m]$
800	40	15	2.70
1210	140	64	1.96
1540	311	264	1.59
1660	400	410	1.50
1710	444	495	1.46

the growth. All the concepts introduced in the Confinement Controlled Sublimation (CCS) method are retained.

In this furnace, shown in Figure 8(a), the graphite confinement enclosure is supported directly by the quartz tube, where the graphite crucible acts as its own RF induction susceptor. Direct contact of graphite to quartz at high temperature is not problematic because the reaction between quartz and graphite is negligible, and in fact graphite is used as a glassblowing tool. The quartz is able to support the hot graphite due to its very small coefficient of expansion. (For quartz it is 5.5×10^{-7}/°C, which is 10 times lower than Pyrex glass.) This means that the temperature of the quartz glass may be below its melting point of 1600°C and sustain a temperature gradient across the points of contact with the crucible that approach 1000°C.

Another added advantage of this design is the small furnace volume, which allows greater pumping speed and a lower ultimate pressure. Pumping speed is improved by preventing water vapor from reaching the vacuum chamber walls by fast exchange of samples, and flowing argon gas to displace air. 10^{-7} mbar is achievable in 20 minutes, whereas previous designs required closer to an hour to reach this pressure.

Control of the power into the furnace is maintained using an infrared ratio pyrometer. Fused quartz glass is opaque to wavelengths longer than 3 μm [62], as shown in Figure 8(b). See Figure 8(c) for an illustration of the two-color measurement. Ratio pyrometry involves two wavelengths, centered around 1μm in the infrared band

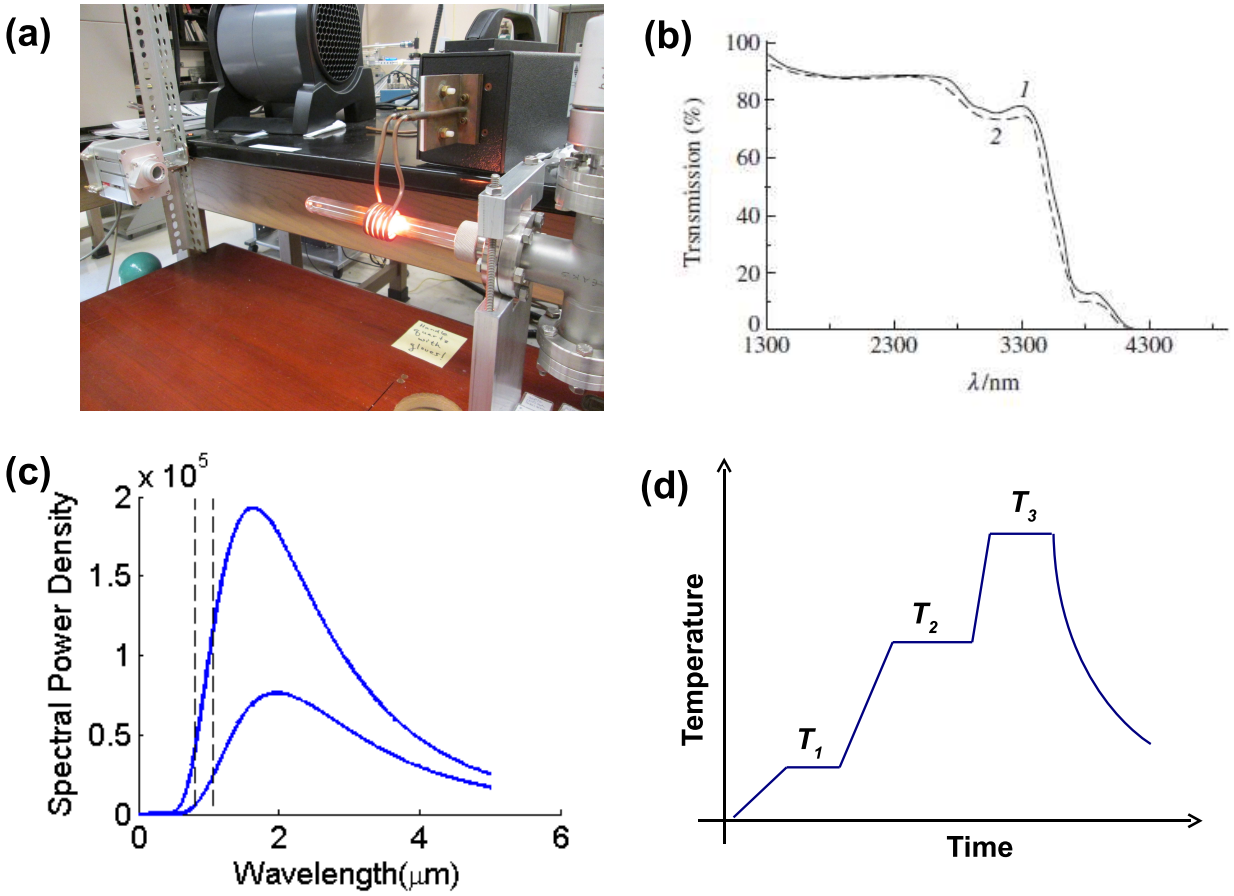

Figure 8: (a) Graphene furnace in operation. Pictured at the left is the infrared ratio pyrometer. (b) Transmittance of fused quartz taken from [62]. (c) Illustration of the measurement made by the infrared ratio pyrometer at two wavelengths, marked by dashed lines. (d) Typical temperature profile for graphene growth.

which is within the passband for quartz. The temperature is determined by the ratio of measured intensities at the two wavelengths. The ratio is known from Planck's law for blackbody thermal radiation. The advantage of two wavelengths, vs. one, is that the measurement is less sensitive to absorption, such as from the quartz glass. Based on the measured temperature, standard PID programming is used to program the power input to the crucible by the RF induction power supply.

Temperatures exceeding 2100°C were sustained for longer than twenty minutes with no damage to the quartz tube, directly demonstrating the viability of the

method. For sustained temperatures above 1600°C, it is recommended to have cooling air flowing around the tube, although no evidence for loss of structural stability for a tube has ever been observed in two years of operation. See Table 1 for a listing of the measured power vs. temperature, where it is compared to the Stefan-Boltzmann T^4 law. There is a deviation from the Stefan-Boltzmann law, which could be attributed to either absorption and re-radiation of radiation with $\lambda > 3.3\mu$m, conduction by the quartz tube, or inaccurate power readings by the induction power supply. Nevertheless the power does roughly scale as T^4, as would be expected for radiation dominated heat transfer.

See Figure 8(d) for a typical growth profile. The step at T_1, between 100°C and 800°C, is to desorb water and other loosely bound adsorbates from the sample and crucible surfaces. Temperature T_2, between 1100°C and 1200°C, is to desorb the silicon dioxide formed on the SiC surface and allow mass-flow on the sample surface (if desired). Temperature T_3 is the graphene growth temperature, which can occur above 1300°C. Cooling can occur naturally or with a pre-programmed cooling ramp.

One question that remains is the time for gas pressure equilibration during growth. This is important to know because otherwise the number of samples in the crucible would effect the graphene growth rate. Solid vapor pressure is an intensive property that does not scale with surface area when in equilibrium. See Appendix D for the details of a kinetic gas theory calculation, which estimates that the gas pressure is steady within 5μs, which is many orders of magnitude shorter than a typical growth time. This confirms that growth occurs very close to equilibrium and that the exposed area of SiC does not affect the growth rate.

2.2 Hydrogen Etching

Good graphene growth requires a flat SiC surface, and many SiC wafers are available with only a rough mechanical polish on their surface. Hydrogen etching is used to

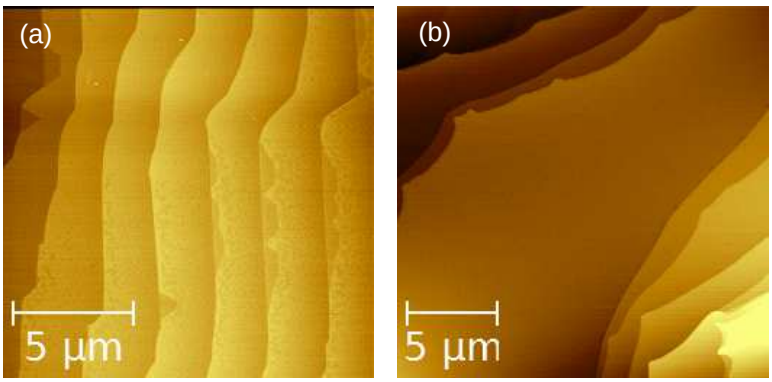

Figure 9: Non-contact AFM images of a (a) hydrogen etched SiC surface at 1400°C. and at (b)1540°C.

make the silicon carbide surface to be active without graphene growth pinning the steps. [63] This is possible because highly reactive hydrogen gas is available to react with free carbon atoms on the surface, as well as with outgassed Si atoms. Sample surfaces may reach thermodynamic equilibrium within half an hour at an etching temperature of 1400°C. As shown in Figure 9(a), these surfaces form into a step-terrace array with atomically flat terraces.

It is worth mentioning that broader terraces and higher steps tend to have lower free-energy. This free energy minimum can be more easily reached by increasing the hydrogen etching temperature.[64] Typical samples hydrogen-etched at 1400°C have terraces about 1μm wide on on-axis wafers. As shown in Figure 9(b), by hydrogen etching at 1540° up to 10μm wide terraces were observed with massive step-bunching.

2.3 Sample Characterization

All device building starts with careful characterization of the patterned structures, as well as that of the graphene itself. Raman spectroscopy and AFM-based scanning-probe methods are the two most common and useful characterization tools.

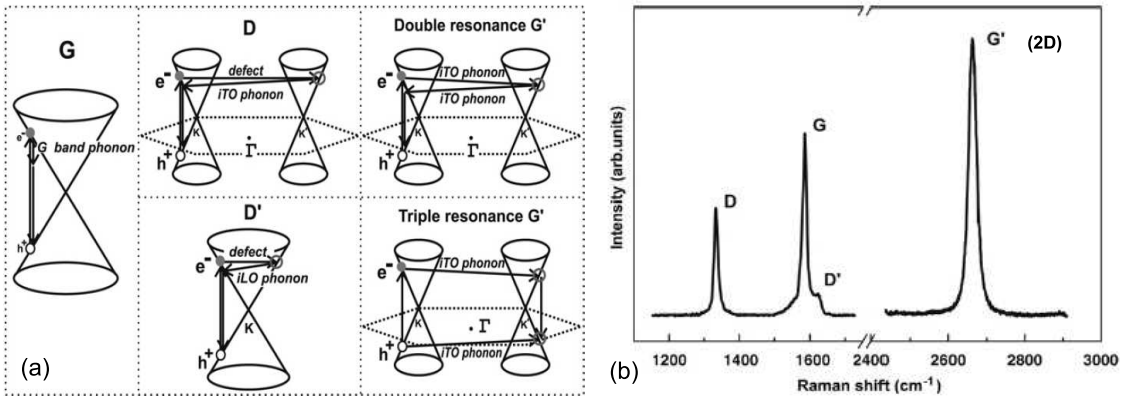

Figure 10: (a) Scattering processes behind the typical graphene Raman peaks. (b) Major peaks in a typical graphene Raman spectrum. Reprinted from [65]

2.3.1 Raman Spectroscopy

Raman spectroscopy is an extremely important characterization tool for graphene. Careful use of the Raman spectra gives information about the presence of disorder, grain size, doping or strain in the graphene lattice. Raman peaks are generated by the inelastic scattering of incident photons with the phonons in the sample's lattice. Incident light is provided by laser, and the work presented in this thesis uses a 532nm laser wavelength.

Different peaks are characteristic of different phonon modes [65, 66]. The most important peaks for graphene characterization are the D, G, and 2D (sometimes called G') peaks. See Figure 10 for a diagram of the scattering processes, as well as representative Raman peaks.

A difficulty with EG on SiC is that the SiC substrate has a powerful Raman signal as well [67]. Taking a SiC background spectra and subtracting it from the SiC+graphene spectra is possible, but there are errors present in this procedure. Kunc[68] developed an alternative method to separate the Raman spectra of the graphene from the SiC adapted from signal-processing techniques, called the Non-Negative Matrix Function decomposition. By specifying that two or more orthogonal

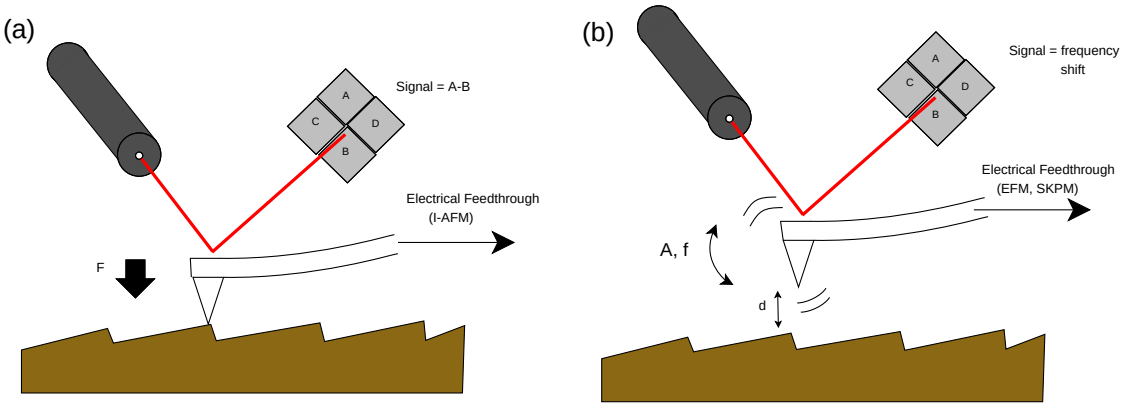

Figure 11: Measurement setup for (a) contact mode and (b) noncontact mode AFM.

basis spectra are present in a set of measurements, the algorithm will find the graphene and SiC spectra as these basis functions.

2.3.2 Scanning Probe Microscopy

Scanning probe microscopy is an extremely powerful set of techniques. Developed after the scanning tunneling microscope (STM) in the late 1980's, scanning probe systems are capable of measuring various surface properties and material properties. While the STM is designed to be sensitive to a tunneling current, Atomic Force Microscopy (AFM) is sensitive to the van der Waals (near-range) forces on the sample surface.

AFM

Contact and non-contact modes are available. See Figure 11 for a diagram of the setup for (a)contact mode and (b) non-contact mode. Non-contact mode AFM is generally less invasive and tips are longer-lasting since they are not constantly wearing against the sample surface.

Contact mode AFM is defined by a force setpoint. Typical setpoint values for contact mode imaging are between 2nN and 10nN. The contact mode topographic signal is measured directly by the signal difference between photodetectors, viz. A-B in Figure 11(a). Additional information about the sample surface may be obtained

by the C-D signal. This is known as Lateral Force Microscopy (LFM) and it contains information about the friction forces between the tip and the sample surface. The LFM signal is dependent on the tip scanning speed as well as the force setpoint. A typical force constant for a contact-mode tip is 0.5 N/m.

Non-contact mode AFM requires additional electronics and set-up parameters, but is ultimately capable of very high resolutions. The main parameters are the frequency of oscillation,, the typical distance of approach, known as the *setpoint*, as well as the amplitude of oscillation. For an NCHR tip typically f_0 =300kHz, the setpoint is -13nm, and the amplitude of oscillation is 20nm. Force constants for non-contact tips are high, often 50N/m, but at the expense of the tip being more stiff and unable to flex if it is forced into contact with the sample surface.

The ultimate resolution for AFM topography is generally defined by the diameter at the end of the tip. Tip production has improved to where tip diameters are almost always around 10nm for standard topographic tips. Special extra-sharp noncontact tips are available with a 2nm tip diameter.

EFM

If the van der Waals forces are known, as it is encoded in the sample's topography, this can be subtracted from the total forces acting on the AFM probe. That leaves the effect of electrostatic forces, which do not fall away as quickly. This is accomplished by having the scanning probe first measure topography, and then re-trace it with the tip raised a few nanometers. This mode is known as Electrostatic Force Microscopy (EFM). EFM is useful for probing charging density and work function changes. EFM is typically measured using an AFM tip that has been especially coated with a conductive coating. The electrostatic force on the tip may be written[69]:

$$F_{DC} = \frac{1}{2}\frac{dC}{dz}[(V_{dc} + V_{cp})^2 + \frac{1}{2}V_{ac}^2] \tag{10}$$

where V_{dc} is the applied DC bias, V_{cp} is the contact potential difference, and V_{ac} is the applied AC bias. Scanning Kelvin Probe (SKPM) is achieved by nulling the potential difference between the tip and the sample surface ($V_{dc} = -V_{cp}$). This is accomplished by running a separate feedback loop in the AFM system. The DC offset corresponds to the contact potential difference between the tip and the sample. Comparing the contact potential difference between the tip and a known reference material, such as gold or HOPG, will determine the exact work function of the tip which can vary depending on how the end of the tip is faceted. This in turn allows exact measurement of the local work function of the sample surface.

With SKPM, the potential flow across a planar device is visible if information about potential distribution on a conducting surface is desired, as it is it is included in the contact potential difference. It should be noted that recently a new mode, frequency modulated SKPM, was made known. [70] It has higher spatial resolution but was not available for the samples measured in this thesis.

EFM and SKPM have less spatial resolution than AFM. This is in part due to the longer range of the electrostatic force, and because the 10nm thick conductive coating on the cantilever increases the tip diameter at least 30nm.

Conducting AFM

If in contact-mode AFM a conducting tip is used, current can be passed through the tip, yielding local information about the conductivity of the sample surface. This is called conducting AFM (also known as I-AFM or C-AFM). Usually platinum coated tips or heavily doped diamond tips, which are more robust, are used. Higher setpoints than for topographic imaging are necessary, typically at least 10nN, in order to have good contact. The currents measured are usually small, around 10pA and up to 1mA on very conducting samples. A special current preamplifier is used inline with the tip. Worn platinum coated tips may be re-coated using e-beam evaporation of pure

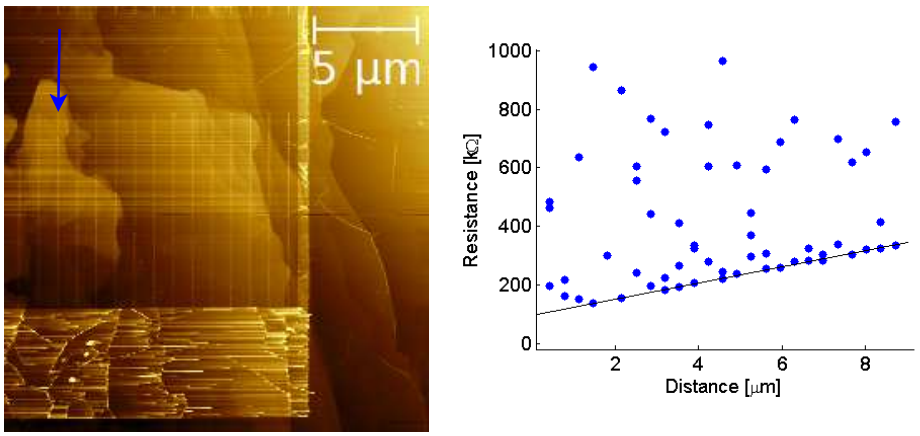

Figure 12: Conducting AFM on a nanoribbon, indicated by the arrow, patterned from bulk C-face graphene. The left image is the topography. The plot on the right is the 2-point resistance measured vs. distance, with the resistance per length $R(L)$ designated by the line.

platinum. 25nm total deposition of Pt evaporated at 1Å/sec. yields favorable results for extending the life of conducting AFM tips.

See Figure 12 for an example of how conducting AFM can be used to measure the resistance of a top-down patterned nanoribbon. Few layer carbon face graphene was used, consistent with the pleats in the carbon pad, that were patterned and etched into 40nm wide ribbons. We expect there to be a minimum contact resistance between the tip and nanoribbon, which falls on a line. The linear fit gives $R(x) = 47x$ kΩ/μm+137kΩ. Note that these ribbons are not expected to be good ballistic conductors, unlike the sidewall graphene nanoribbons I describe in Chapter IV.

It is important to mention the contact resistance of the C-AFM tip, which is given by the linear intercept of 137kΩ. This may be thought of as a point-contact resistance.[71] We might simply estimate the resistance from Maxwell's formula $R_{contact} = \rho/(2a)$ where a is the area of contact. If we take $\rho = 500\mu\Omega$cm (that of graphite, perhaps reasonable on graphene) and $a = 1$nm we get 250kΩ, which is not so different from what is measured. This contact resistance is in agreement with others' work of platinum on HOPG[72].

2.4 Graphene Device Production

Graphene device production takes many steps from standard top-down microelectronic fabrication processes. The most important consideration in these processes is that graphene is a surface conductor, and is therefore sensitive to any process that is damaging or any process that leaves scattering centers on the surface. Another advantage that EG on SiC based nanoelectronics has is the high temperature stability of the SiC and the graphene. This means any temperature normally used during microelectronic processing will not be a problem. This section begins with describing lithography, which defines the geometry for processes being used.

2.4.1 Spin-coating

Spin-coating is the first step in the lithographic process. Ignoring the effects of evaporation, the spin coating thickness h is given by [73]:

$$h \propto \left(\frac{\mu}{t\omega^2}\right)^{\frac{1}{2}} \tag{11}$$

The most important factors in determining resist thickness are coating speed ω, time t, and the viscosity μ of the polymer. Choosing an appropriate molecular weight, which influences μ, is the first choice in determining a resist. Time is usually kept constant, at about one minute, while the spin coating speed is used to fine-tune the film thickness.

This model assumes good adhesion between the resist and the substrate. Poor adhesion may result in heterogeneous films. Pre-coating the substrate with a thin (10nm) molecular film will give a favorable contact by changing the surface energy. A commercial adhesion promoter is available for this process, SurPass 3000$^{\text{TM}}$, particularly when coating graphene or SiC with HSQ negative e-beam resist.

Once the resist is spin-coated, it is baked to cross-link the polymers in the resist and then the sample can be exposed. After patterning the resist is developed and is

ready for either an etch or metal liftoff step. An AFM profile may used to measure film thickness.

2.4.2 Electron Beam Lithography

Lithography is the spatial basis for all micro- and nano- fabrication. E-beam lithography uses a finely focused electron beam to either polymerize or decompose the resist. The two types of resist are classified as either positive or negative. Positive resist becomes more soluble in the developing solution after exposure, whereas negative resist is more soluble if it is not exposed. By locally exposing the resist and developing a pattern is created in the resist. With e-beam lithography very fine line pitches are achievable, below 20nm. Perhaps most important of all about e-beam lithography is its flexibility; you can change the mask each time as you learn more about the experiment.

Achieving ultimate resolution involves reducing scattering mechanisms: forward scattering and backscattering. Forward scattering is influenced by the energy of electron, and the forward scattering cone can be narrowed by increasing its energy. Most experiments in this thesis were patterned with a JEOL 5910 SEM, with 30keV energy, modified for e-beam lithography using the NPGS software package, others were patterned with JEOL JBX-9300 system (available in the IEN cleanroom). The advantage of the 9300 is the 100keV acceleration energy, as well as very stable electronics. With 100keV, forward scattering is no longer the dominant mechanism, and electron back-scattering effects are the more dominant scattering mechanism.

A special case of scattering involves long-range electrostatic repulsion due to accumulation of charge during the exposure, which is important on an insulating substrate like SiC. Charging effects are most notable at high beam currents (e.g. 6nA) and for large exposed areas, i.e. large values of charge. To an extent the charging effect is reduced if the write order of the pattern is not contiguous or the beam current is

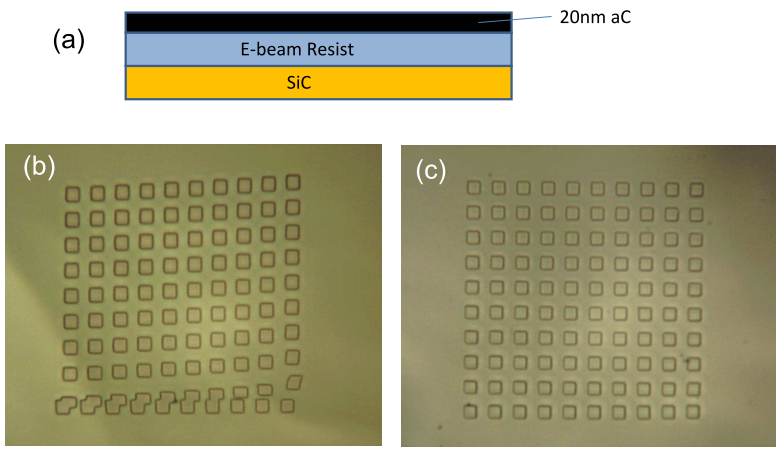

Figure 13: (a)Setup for aC as an anti-charging layer for e-beam lithography. (b)PMMA on V-doped SiC with no anti charging overlayer. (c)with 20nm aC on top.

reduced. The contrast between having a charging effect or not is quite visible with EG on SiC depending on the presence of graphene or contacts throughout a given process.

A conducting layer is necessary on the surface of the e-beam resist if the substrate is too insulating and standard exposure currents and write orders are desired to reduce processing times. ESPACER^{TM} is a commercially available polymer used for this purpose. We find that amorphous carbon overlayers work well. See Figure 13 for an exposure with and without an aC overlayer. Other groups use thin layers of gold or aluminum. Gold is not as desirable for an anti-charging layer because its high Z nucleus more easily scatters electrons.

2.4.3 Optical Lithography

Optical lithography (also called photolithography) has the advantage of mass parallel production as well as fast processing time overall. The three most popular kinds of optical lithography are contact, proximity, and projection lithography. In contact lithography the mask directly contacts the resist, whereas in proximity the mask is held about 3μm away, and in projection mode the pattern is projected through a set

Figure 14: Manual contact mask aligner set for mercury I-line (365nm) UV exposure. At the left is the microscope for viewing alignment. In the center at the top is the UV source. Beneath is the mask alignment fixture. At the right is the UV source shutter control and mercury lamp power supply.

of lenses. Contact lithography, although no longer as popular in industry due to its low resolution, is used for our processes and is a straightforward research tool.

The writing resolution is mainly determined by the resist thickness and the exposure wavelength[74]:

$$W_{min} \approx \sqrt{k\lambda t} \tag{12}$$

where λ is the wavelength, t is the resist thickness, and k is a process condition parameter, typically near 1. For the mercury I-line, with UV wavelength $\lambda = 365$nm, and resist thickness $t = 1\mu$m we have $W_{min} = 600nm$, consistent with proven process parameters.

Generally alignment accuracy is limited by the mechanical control of the system and the microscope resolution. Typically 25 mW/cm^2 intensity is used from a mercury-arc lamp. Standard photoresists are exposed with a dose between 100 and 200mJ/cm^2, meaning an entire wafer or chip can be exposed in 4 to 8 seconds, as opposed to roughly 20 minutes for a typical e-beam exposure over a single chip.

The trade-off for high throughput is that design flexibility is more limited by having a fixed mask. Care must be taken to have a clean interface between the

sample and the mask for good and reproducible alignment. For a typical contact lithography process, residues will build up on the mask surface after a few exposures so that cleaning the mask is necessary. Finally, like e-beam resists, negative and positive tone resists are available.

2.4.4 Metal Deposition

The standard method to produce contacts to graphene is by lift-off of deposited metal. Evaporation of the metal to be deposited is preferred over sputtering. This is because sputtering metal films may etch or severely damage the graphene to be contacted. The lift-off method provides a way to form contacts from many different materials, including nickel, aluminum, palladium, gold, and titanium, to name a few commonly evaporated materials during these processes.

Single layer e-beam resist may be used for thinner metal films that require higher feature resolution. More reliable lift-off is achieved by using MMA/PMMA e-beam resist bilayers. First MMA is spin coated onto the sample, and then PMMA is spin coated onto the MMA layer. The lower MMA layer is more sensitive to the electron beam radiation and therefore develops into a wider feature width, whereas the PMMA has a narrower feature width. This creates an overhang in the sidewall profile of of the resist. For optical lithography, a negative resist will achieve the same overhang structure as the bilayer resist structure. This is due to the shadow effect of the photomask. Bilayer photoresists are available if lift-off of positive resist is needed.

Metal evaporation is typically done using e-beam or thermal evaporation at high vacuum with a directional source.[75]. A point-like source of metal vapor is directional if the metal evaporants do not scatter. Since almost all metal evaporants stick to the chamber walls at room temperature, only collisions with the background gas will scatter the metal evaporants and reduce directionality. The mean-free-path λ of a

particle as a function of the gas pressure is given by:

$$\lambda = \frac{k_B T}{\sqrt{2}\pi d^2 P} \tag{13}$$

$k_B T$ is related to the thermal energy of the gas, d is the molecular size, and P is the gas pressure. If we take d = 2Å at 300K, then λ =160m at 10^{-6}Torr, whereas λ is only 20nm at atmospheric pressure. Since the vacuum chamber is on the order of 1m in size, directional evaporation typically takes place around 10^{-6}Torr or lower.

By immersing the coated sample in acetone, the resist will dissolve and lift-off the unneeded metal film. The lift-off procedure can be the most failure-prone step of the whole process, because the entire metal film and resist stack may not delaminate. A failed metal lift-off leaves a portion of the sample useless at best, and wastes an entire sample in the worst case. Therefore care must be taken to not let the sample be prematurely removed from acetone and that the right resist is chosen.

2.4.5 Plasma Etching

The other primary use for lithographic masks is to selectively etch certain portions of a sample. Depending on the depth and the material to be etched, there is a proper plasma process to be used. Plasma etching is also known as dry etching, and it is used to pattern graphene and SiC. There are two main plasma etches used, RIE and ICP, with the main difference being the amount of power that is injected into the plasma.

A plasma etch is defined by the gases, the power input into the plasma, and the operating pressure. The outcome of the plasma etch is defined by the etch rate, selectivity of the etch, and the anisotropy of the etch. The etch rate is simply how fast the target material is removed. Selectivity is the relative etch rate between the resist and the target material. Anisotropy determines the steepness of the sidewalls. Etch rates and anisotropy are directly related to the power input. The pressure sets the mean-free-path of the constituent etch gas, as in equation 13, with lower gas

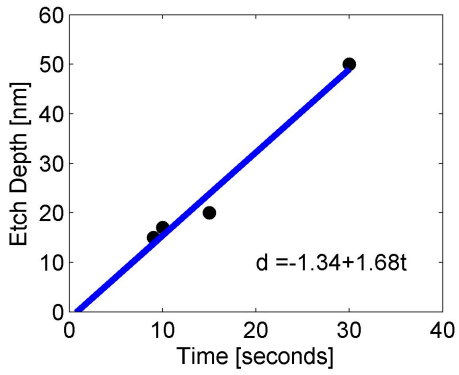

Figure 15: Etch test for 100W SF_6 based SiC etch using the SAMCO RIE.

Table 2: SF_6 based SiC etch test data used in Figure 15

Time [seconds]	Etch Depth [nm]
9	15
10	17
15	20
30	50

densities yielding steeper sidewalls. Finally, higher power and lower pressure etches tend to be sputter-dominated, which has a 1:1 selectivity between most materials. Lower power and higher pressure etches tend to be more selective, and are based on chemical etching mechanisms rather than sputtering, but have less anisotropy.

RIE

Reactive Ion Etching (RIE) has only one RF power source, with the most common modern configuration being the parallel-plate reactor, that is capacitively coupled to the plasma. Oxygen plasma etches graphene and amorphous carbon. Oxygen plasma may also be used to remove resist residue, which is known as 'descum' processing. Typically a 16W O_2 plasma with 4sccm O_2 flowing etches graphene. This etch is chemically based, as at 16W not as much sputtering occurs.

For etches less than about 50nm in the SiC, an SF_6 based RIE works well. See Figure 15 for an example of where I determined the etch rate for SiC with an SF6 plasma. This is using 100W with 3.2sccm SF_6 flowing and 0.8sccm O_2 gas flowing.

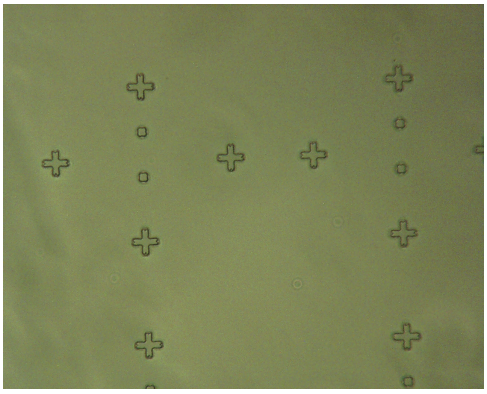

Figure 16: Optical micrograph of 600nm high alignment markers etched into SiC using a CF_4 based ICP etch, used to create SiC features compatible with graphene growth and visible for e-beam lithography.

Unlike the graphene etch, this etch is based on the sputtering mechanism of heavier SF_6 molecules. Experimentally, it is possible to determine the etch rate in the SiC by etching a series of samples for various times. Using the AFM topography, the etch depth may then be determined and plotted to determine the linear etch rate. From the fit to the slope, 1.7nm/sec of SiC is etched. Note that the x-intercept of the fit is at about 0.8 seconds. This is interpreted as the time it takes for the plasma to come to full etching power.

Finally, it is important to consider the selectivity of the resist to the material being etched. The etching selectivity between SiC and most e-beam and photo resists is about 1:5 to 1:10. This permits RIE etching of up to 100nm of SiC using polymer resists before completely etching through the resist.

ICP

Inductively Coupled Plasma's (ICP) has an additional, higher power, RF source that increases the speed of the etch and increases the anisotropy of the etch. This is a coil (hence inductive coupling) around the chamber, in addition to the parallel plate capacitive coupling in the primary power source. Much deeper etches into SiC are available with this method. The sidewall profile angle will approach 90° with an ICP

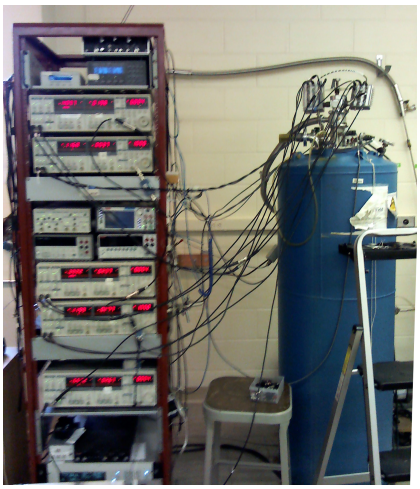

Figure 17: LHe^4 cryostat, pictured at the right. On the rack at the left are temperature controls for the variable temperature insert, cryogen level monitors, a 9T superconducting magnet power supply, and lock-in amplifiers for measuring voltages and currents on the sample.

etched sample due the increased anisotropy of the higher etch power.

A hard mask, like nickel, is necessary because of the greater amount of material removed, since polymer based masks are insufficiently selective. See Figure 17 for an example of 600nm alignment markers prepared into the SiC using a CF_4 gas based ICP available using the Plasma-Therm ICP in the IEN cleanroom. The SiC ICP etch recipe is described by Hicks in his thesis.[76]

2.5 Electronic Transport Measurements

Transport measurements are the final part of many EG experiments. Samples may either be wirebonded to a chip carrier for measurement or measured on a probe station. Samples to be measured in the cryostat must be wirebonded using the ultasonic manual WestBond wedge bonder in our lab. The probe station is used to contact samples for testing prior to wirebonding, as well as for experiments were wirebonding is not necessary or undesirable because the sample requires further processing.

Electrical noise is present in all transport measurements and care must be taken to know its magnitude and how to reduce its extent. Phase-sensitive lock-in amplifiers

are capable of measuring microvolts, and further noise can be removed with isolation transformers and grounding. Current preamplifiers can increase the sensitivity of the lock-in amplifier to small input currents, down to picoamps. Typical lock-in operating frequencies used in this thesis are between 13Hz and 20Hz. Typical measurements made in this thesis are precise to about one part in 10^{-4} (0.01%).

Some measurements involve freezing out the vibrations in a sample, as mentioned in Chapter I,and therefore temperatures approaching 0K are desirable. Liquid nitrogen (LN2) and liquid helium (LHe) are available for cooling to low temperature. LN_2 has boiling point of 77K and LHe has a boiling point of 4K. Intermediate temperatures between 4K and room temperature are achieved by using a low power heater attached to the sample dipstick. The boiling point of LHe can be lowered to 1.4K by reducing the pressure in the sample space with a suitably powerful vacuum pump. LHe is not as abundant as LN_2 and is therefore more expensive to use. For a less expensive measurement, cooling the sample to liquid nitrogen temperature is sufficient.

In addition to varying the temperature, a $\pm$9T superconducting magnet is available for further transport measurements on samples. For many experiments it is worthwhile to measure magnetic field sweeps at a variety of temperatures. As described in Chapter I, this provides information about different scattering processes by measuring the Hall voltage.

CHAPTER III

AMORPHOUS CARBON

The purpose of this chapter is to introduce new techniques I developed with evaporated amorphous carbon and its uses during and after growth with EG on SiC. Here I show that amorphous carbon can be used as a contact to graphene and as a step-flow barrier during its growth on SiC. This chapter starts by describing how to deposit and etch amorphous carbon, followed by its use for step-flow barriers and electrical contact to graphene.

3.1 Amorphous Carbon Evaporation

Solid carbon does not melt or have significant vapor pressure below 3000°C, higher than any solid at standard conditions. The Bradley point-contact source [77] is a simple but effective evaporation source for carbon. As seen in Figure 18, a point contact is made between two graphite rods. The rods are in a vacuum chamber that is pumped down to 10^{-6} mbar. See Figure 18(c) for a plot I prepared that determines the average deposition rate with 3.5V applied to the junction. The evaporation rate varies somewhat according to operator experience, as shown by the spread total deposited thickness. Roughly 1.5 seconds are required to heat the junction to the temperature of evaporation and the rate of deposition is roughly 4.3 nm/sec.

Reproducibility of the deposition is assured if the operator starts with a well defined rod tip geometry, shown in Figure 18(b), starts at the same voltage, and ends the deposition after the same duration. My standard practice is to use the same length of 1.6mm diameter rod for each deposition to ensure a repeatable deposition. 120A through the point contact for 6 seconds deposits a 30nm film. As calculated from conservation of mass this is consistent with the source being 5cm distant from

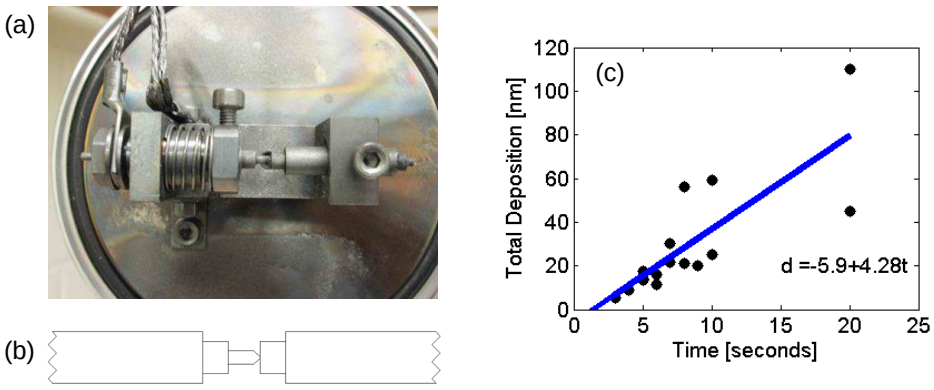

Figure 18: (a) and (b): Cressington 108A point contact carbon evaporator, based on the design by Bradley [77]. (c) Plot to determine the deposition rate.

the sample and 0.5mm of the rod vaporizing.

3.2 Etching

Patterned carbon pads are needed for graphene device fabrication. Attempts to lift-off the amorphous carbon on SiC, as is done with metals, have proven unsuccessful. This is possibly due to high pressure during evaporation, which reduces the directionality of the deposition and coats the sides of the resist. Poor adhesion to the substrate is another problem, as the carbon film will delaminate if lift-off is attempted. The process for patterning the carbon into useful structures proposed here is based on oxygen plasma etching, using standard e-beam or photoresists as an etch mask.

Amorphous carbon is etched using a 16W oxygen plasma RIE. As seen in Figure 19, the etch rate I observed is 0.3nm/sec. The etch self-limits at SiC surface since a silicon oxide passivation layer forms on the surface. To pattern the aC , any standard e-beam or photoresist may be used as an etch mask for etching the carbon, and aC may be patterned simultaneously with the graphene if needed.

3.3 Annealing Properties

As-deposited amorphous carbon has intrinsic stress [78], with an example shown in Figure 20. Delamination will occur if the film is too thick or not adhered well enough

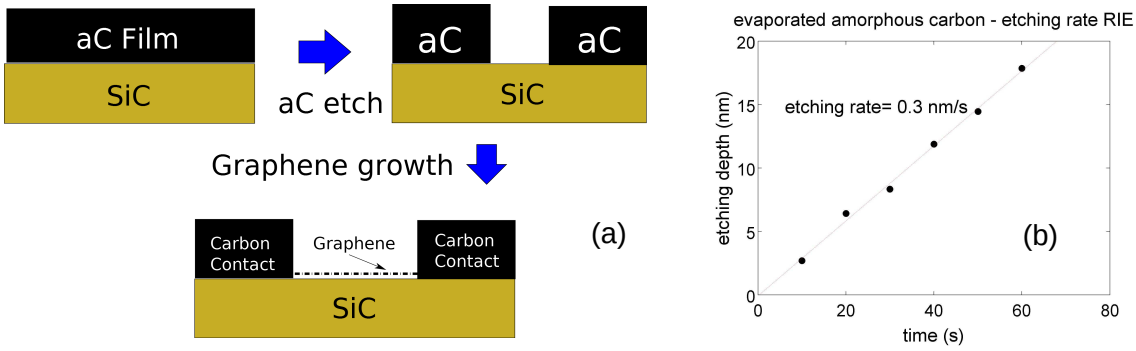

Figure 19: (a) Etch process for creating amorphous carbon contacts or step-flow corrals. (b) Experimental data for determining the etch rate in a 16W O_2 plasma.

to the substrate. Shown in Figure 20(a), released stress in the film is visible as bubbles. Relative thermal contraction to SiC may introduce additional stress has been been suggested[50]. The effect is more pronounced in larger area films where more material must deform. We have not noticed stress effects in microstructures, where the typical size is less than 50μm, as shown in Figure 20(b) where there are no bubbles or distortion in the patterned structure. In spite of the stress effects in the large area films, the amorphous carbon is still quite useful for graphene research.

Annealing the as-deposited amorphous carbon is very straightforward, and can be done in the same furnace system as for graphene growth (See Chapter II). Nanocrystalline graphite forms upon annealing, as evidenced by increasing order in the Raman spectra. Evaporated amorphous carbon films may also be annealed during the graphene growth.

We ran a series of anneals between 970°C and 2000°C on our evaporated amorphous carbon films for a starting point and to compare with previous studies on crystallized aC[6, 79]. In Figure 21, we plot the sheet resistance and Raman spectra of the deposited aC after successive heat treatments at higher temperatures. The Raman spectra of the as deposited aC shows a broad band between 1200-1700cm^{-1}, typical of amorphous carbon. With higher temperature heat treatments, the spectrum develops well defined peaks at the positions of the graphite D, G, and 2D peaks.

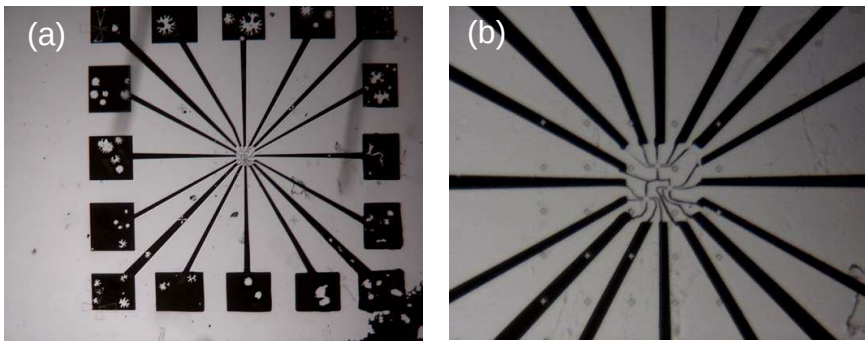

Figure 20: Optical micrograph of released stress features in patterned carbon structures. (a)At 10x magnification, the $100\times100\mu m^2$ contacts had bubbles form. (b)Micron-scale features were able to relieve stress without bubble formation, at 100x magnification.

The D to G peak ratio indicates that sp^2 hybridized crystallites grow as the annealing temperature is increased. From the Raman spectra at 1540°C, which is close to the graphene growth temperature, we find D to G peak ratio $\frac{I_D}{I_G} = 1.04$. This ratio corresponds to a graphitic crystallite size of 18nm[80].

We measured the as-deposited carbon film to have a bulk resistivity of 1.2Ωcm. As expected there is a decrease in resistance after annealing, as shown in Figure21(b) for the resistivity. At the highest temperatures the sheet resistance of the annealed carbon layer is 1.6kΩ□, corresponding to a resistivity ρ=4000$\mu\Omega$cm, close to values published for pyrolytic graphite after treatment[6] at 2000°C. Although this resistivity is much higher than for a metal, this is a low enough resistivity to use crystallized aC as a contact to graphene.

Figure 21(c) presents the resistivity as a function of temperature of a 25nm thick carbon pad after evaporation, patterning and heat treatment at 1540°C for graphene growth. The room temperature resistivity of 4750$\mu\Omega$cm and its negative temperature dependence with a moderate 50% increase from 300K to 4K are in agreement with the literature on nanocrystalline graphite for a 18nm crystallite size[79], as determined by the Raman spectra in Figure 21.

As shown here, the amorphous carbon behaves like nanocrystalline graphite, and

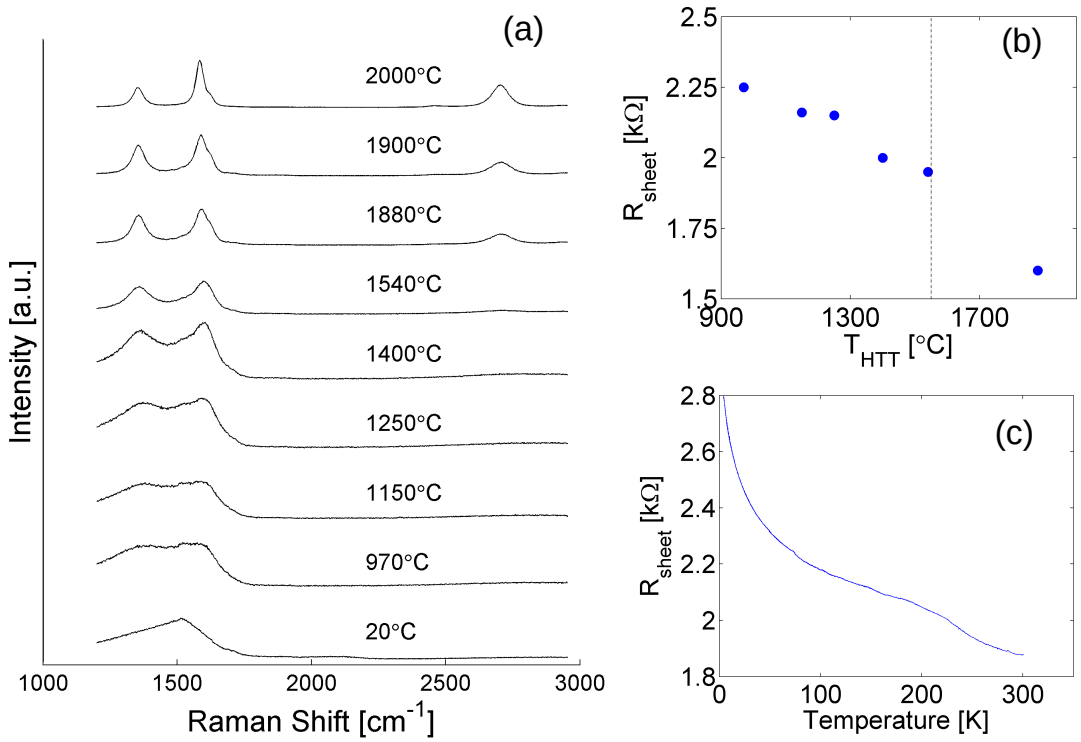

Figure 21: (a)Raman spectra of 25nm thick aC on SiC after successive heat treatments. (b) Sheet resistance of the aC on SiC after anneals. The dashed line marks the graphene growth temperature (1550°C). (c) Temperature dependence of the sheet resistance of aC film annealed at 1550°C.

we therefore expect it to be chemically and physically compatible with graphene growth. The rest of the chapter describes experiments using the amorphous carbon to control the growth of graphene and to make electrical contact to the graphene.

3.4 Amorphous carbon corrals

To be technologically viable, graphene must be grown in a well controlled manner. Beyond preparing well ordered 2-dimensional graphene films, growth needs to be tailored at the nanoscale to produce the desired devices at pre-defined locations. Although EG grows like an overlaying carpet on the stepped SiC surface, steps provide graphene nucleation sites that need to be controlled [81, 82, 83]. Furthermore, underlying SiC steps induce additional electronic scattering in graphene[84] .This section focuses on locally controlling the step bunching of SiC during EG growth.[85]

SiC step spacing depends on the miscut angle of the SiC crystal surface from the basal plane of the Si or C terminated faces, in addition to the thermodynamically favored step height. The smallest miscut angle of commercially available SiC wafers is at most 0.1°, but it varies throughout the wafer and leads to variations in the step density and orientation. Preparation of well-defined SiC surfaces with regularly spaced steps, by hydrogen etching, can be preserved in a range of growth parameters [64] but generally leads to further step bunching at the graphene growth temperature (T>1300°C in the confinement controlled sublimation method [86] or higher under atmospheric pressure argon [87]). These methods, however, cannot provide a precise alignment of the steps. Another way is to get rid of the steps altogether by step flow at the edges of etched mesas[83, 86, 88].

What is proposed here is to evaporated amorphous carbon and then etch corrals into the carbon film to prevent any movement of the steps. This is similar to barrier techniques used on silicon surfaces[89, 90]. See Figure 22 for a schematic of how the step-flow barriers work, before and after the graphene growth. This concept assumes

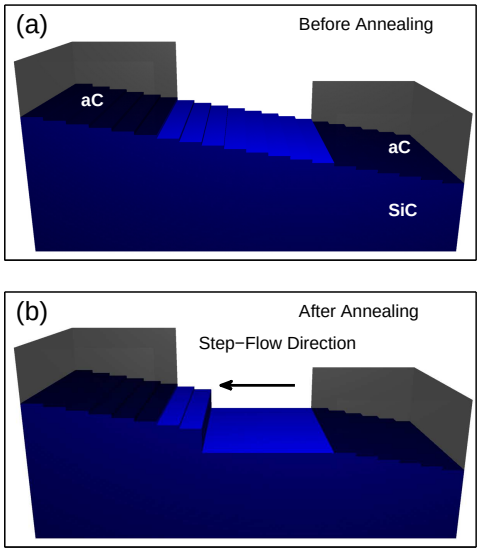

Figure 22: Schematic of the step-flow barrier concept before (a) and after (b) step-flow has occurred. Step bunching must occur for large step-free areas to form.

that the carbon corrals are stable during the SiC step-flow and graphene growth processes and that the aC will prevent step flow on the substate below it. This is a reasonable assumption first considering that bulk graphite and diamond have very high melting points, and have very low vapor pressures. Another important advantage of aC is that it is removable with oxygen plasma after growth so that it is compatible with processes requiring flat surfaces such as silicon wafer bonding or Si[42] and SiC electronics[91]. This is unlike mesa structures for step flow control[83], which cannot be removed after growth.

We prepared EG samples using nominally on-axis 4H SiC (0001) and $(000\bar{1})$ substrates . Sample G1 was hydrogen etched prior to the corral patterning graphene growth. Sample G2 and B1 was left CMP polished prior to the carbon deposition. Using the e-beam lithography and etching techniques described earlier in this thesis, $5{\times}5\mu\text{m}^2$ sized corrals are patterned into the SiC. For this pattern, MaN 2403 negative resist is used with a dose of 200 $\mu\text{C/cm}^2$, and the oxygen RIE discussed in section 3.2 is used to etch the pattern into the aC.

After aC deposition and patterning, the samples are cleaned overnight in acetone to dissolve the remaining resist, and then the samples are rinsed with isopropol alcohol. Graphene samples are grown using Confinement Controlled Sublimation (CCS) in a graphite enclosure in an induction heated furnace. [86] The sample is annealed at 1150°C for 20 minutes to remove silicon dioxide, and then the graphene growth step proceeds. The Si-face graphene sample G1 was grown at 1600°C for 40 minutes and the buffer layer sample B1 was grown at 1350° C for 30 minutes.

See Figures 23(f) 24(f), and 25 for the AFM topography after the sample growth. The step morphology aligns to the aC grid on all samples. An important, and indeed quite striking, feature to note is that the aC grid remains stable throughout the graphene growth process, despite being atop an active SiC surface. Comparing the width and size, as well as height (20nm) of the aC features in Figures 23 and 24 before and after growth yields no differences to within a nanometer. Furthermore, the original SiC step features are seen underneath the aC. See, for example, the SiC steps that remain under the aC in Figure 25 on the C-face. This means the aC is structurally more stable than the SiC surface it rests upon, and is providing the barrier to SiC step movement.

Before growth, the typical step width on sample G1 (Figure 23) is 0.96 μm. After growth and away from the grid, the typical step width is 0.22 μm, and within the grid the step width is increased to 1.9 μm. On sample B1 (Figure 24) the typical step width before growth is 0.2 μm. After growth the typical step width away from the grid is 1.4 μm and within the corral the step width is 3.3 μm. In both the hydrogen etched (G1) and non-hydrogen etched (B1) cases the presence of the step flow barrier increases the typical step width. In comparision, steps pinned by mesa edges on the Si-face yield step-free terraces up to 1 μm[83], whereas the use of the aC corral provides comparable if not larger step-free areas by using favorable growth conditions. Similar results are observed on sample G2.

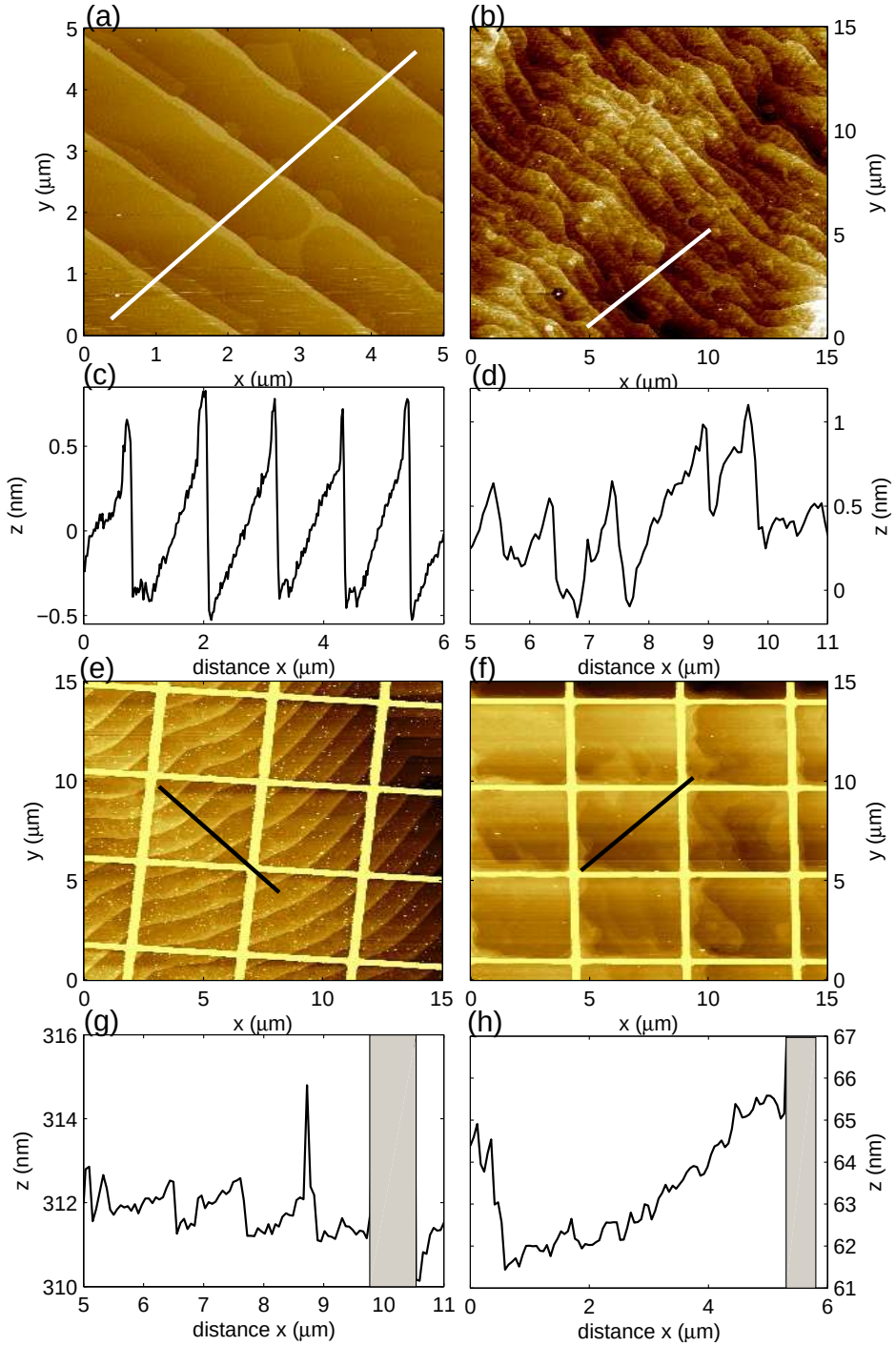

Figure 23: AFM images of the surface of hydrogen etched SiC(0001) (a) before and (b) after graphene growth. The corresponding step profiles taken along the step flow (white line in figures (a) and (b)) (c) before and (d) after graphene growth. The AFM images (e) and (f) and corresponding profiles along step flow (g) and (h), respectively, depict the morphology before and after graphene growth using the amorphous carbon grid.

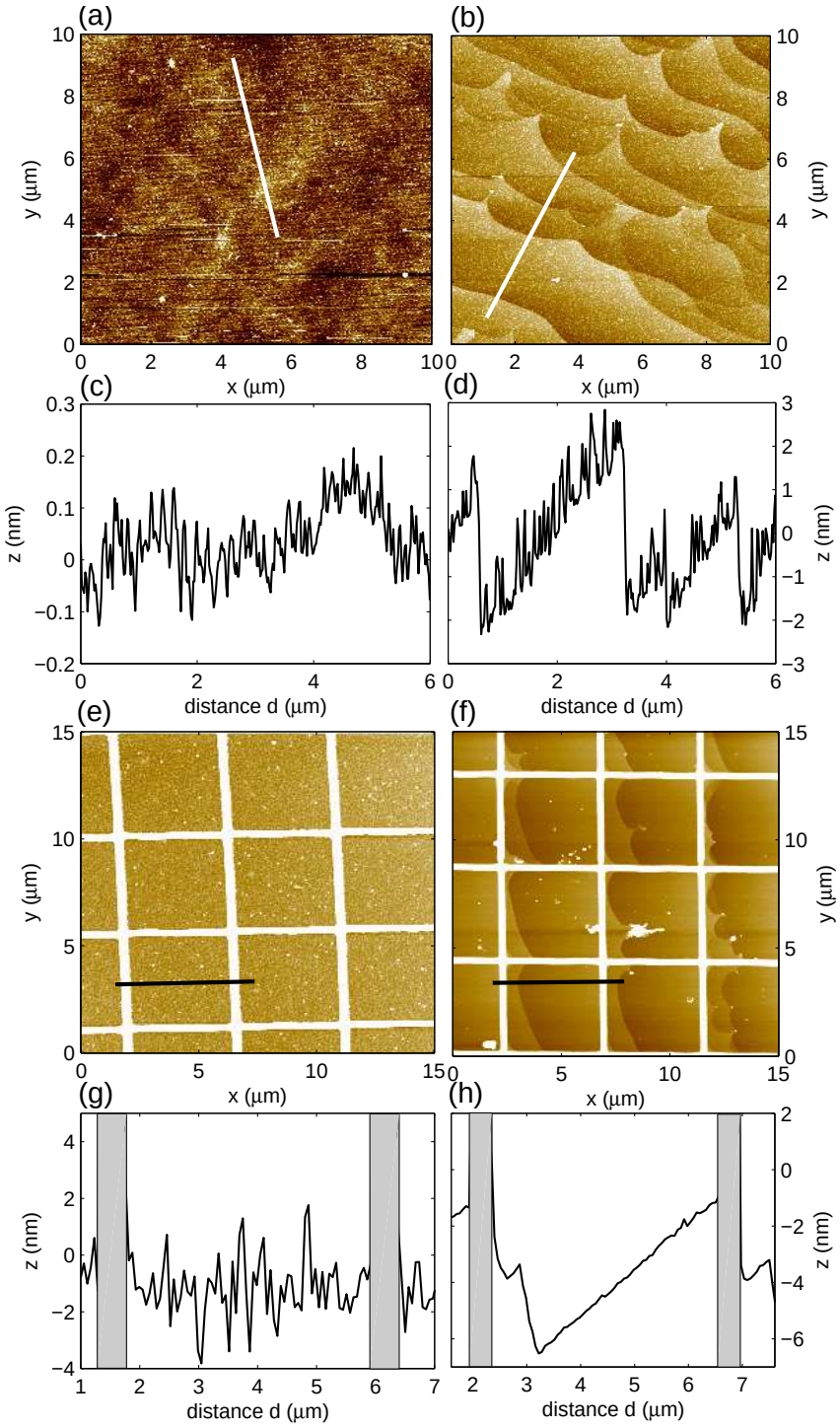

Figure 24: As in Figure 23, but here for sample B1. The SiC surface was chemically and mechanically etched prior to growth. The process of buffer formation without aC grid (a) before and (b) after buffer growth, corresponding profiles (c) and (d). The surface morphology using the aC grid (g) before and (h) after buffer growth. Corresponding step profiles along the step flow are shown in figures (g) before and (h) after buffer growth.

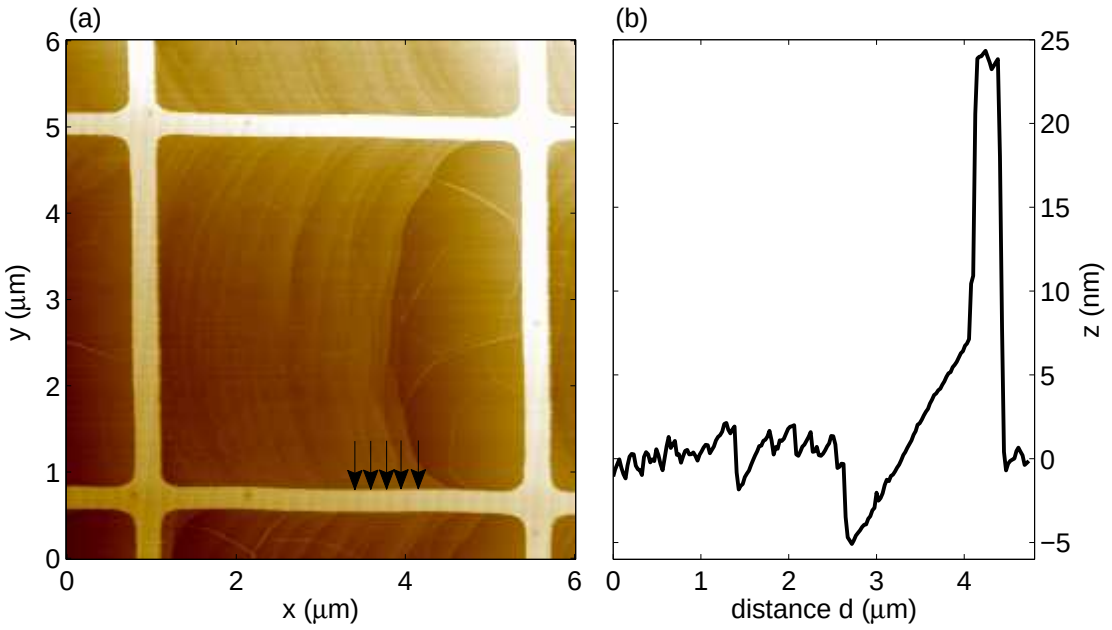

Figure 25: Carbon face pinning on sample G2. The arrows indicate the position of the SiC steps preserved beneath the aC layer.

The 0.5nm scale roughness seen in Figure 23(f) is due to contamination on top of the graphene after the graphene growth. Larger, nanometer sized aC particles from the aC deposition pin the steps seen in sample B1 away from the gridded area into a pinched shape (Figure 24(b)). Nanometer sized aC particles are deposited in greater numbers as the carbon rod source is heated to higher temperatures.

After the growth the Raman spectra is measured at various points on samples G1 and B1. Figure 26 shows Raman spectra for samples G1 and B1. The Raman laser spot was focused on the aC grid in Figure 26(a), and within the aC grid, for samples G1 and B1 in Figure 26(b) and (c), respectively. Using Non-negative Matrix Factorization (NMF) spectral decomposition the Raman spectra were separated into their principle components[68]. In each case two principal components are found, representing either the aC, graphene and buffer layer, respectively with SiC underneath. Notably, no graphene component is found for Figure 26(a), confirming that the aC effectively caps the SiC to prevent graphene growth.

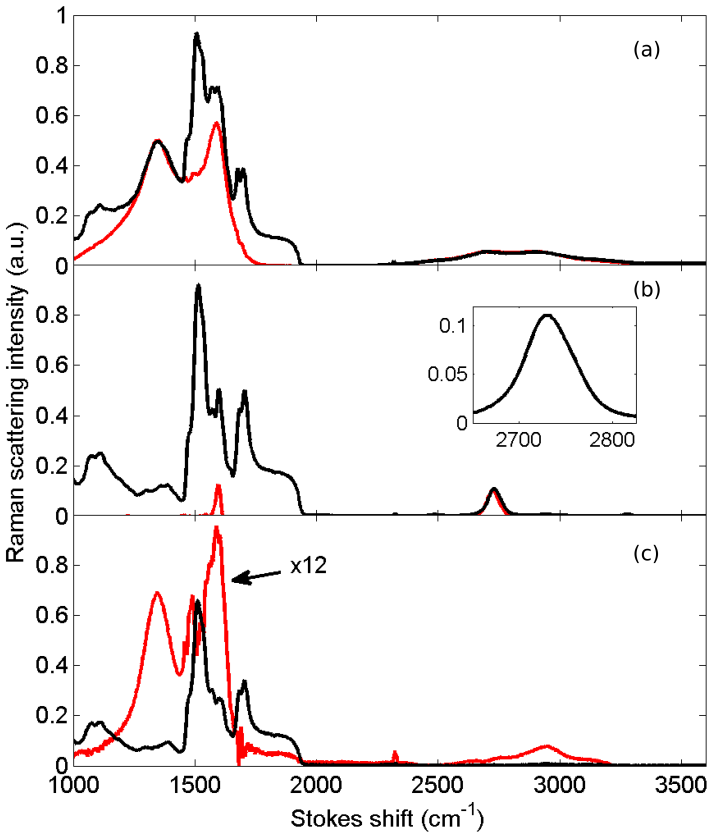

Figure 26: Raman scattering spectra (using a $\lambda = 532$nm laser) of (a) in red: aC and in black: aC and SiC, (b) in red: Sample G1 single layer graphene and in black: graphene and SiC (c) in red: sample B1 buffer layer on a Si-face 4H-SiC, and in black: SiC and buffer.

The Raman component that corresponds to the aC indicates nanocrystalline graphite. The ratio of the D to G peak intensity $\frac{I_D}{I_G} = 0.86$ corresponds to a graphitic crystallite size of 20 nm.[80]. This is expected since nanocrystals form upon annealing the aC at graphene growth temperatures. For the spectrum in Figure 26(b) of sample G1, the graphene component shows no D peak at 1350cm^{-1}, indicating excellent structural order. The 2D peak centered at 2730cm^{-1} has a FWHM of 63cm^{-1}. This width is consistent with Si-face bilayer [65]. The buffer layer Raman component in Figure 26(c) for sample B1 has a much weaker signal than graphene, and is similar to previously published buffer layer spectra. [92, 93] In both G1 and B1 cases Raman spectra show that good graphene or buffer were grown with aC nearby.

Further step-flow experiments include modifying the aC grid, the wafer miscut, and the growth conditions. Different aC step flow enclosures will tailor the step orientation according to the boundary conditions set by the grid. Additionally, an insulating alternative to aC, like oxides or diamond-like carbon, may be complementary to the conductive aC. Performing step flow control on vicinal cut wafers may yield more reproducible step bunching, since the total miscut angle will not be as sensitive to the miscut angle uncertainty. The step bunching is likely to be greater as well on vicinal cut wafers, thereby enhancing the step flow control.[94] Finally, by increasing the gas pressure in the CCS furnace it is possible to raise the onset temperature of graphene growth[86]. This would increase the step flow rates to possibly reach lower surface free energy before graphene forms and therefore inhibits step-flow during graphitization.

To conclude this section, it is seen that evaporated amorphous carbon is completely compatible with the CCS growth method. We have demonstrated that SiC step bunching is pinned by an aC cap that acts as a step flow barrier. The patterned aC grid is structurally stable on an active SiC surface and the step morphology is aligned to the aC grid. Good single layer graphene is grown on up to 4 μm wide

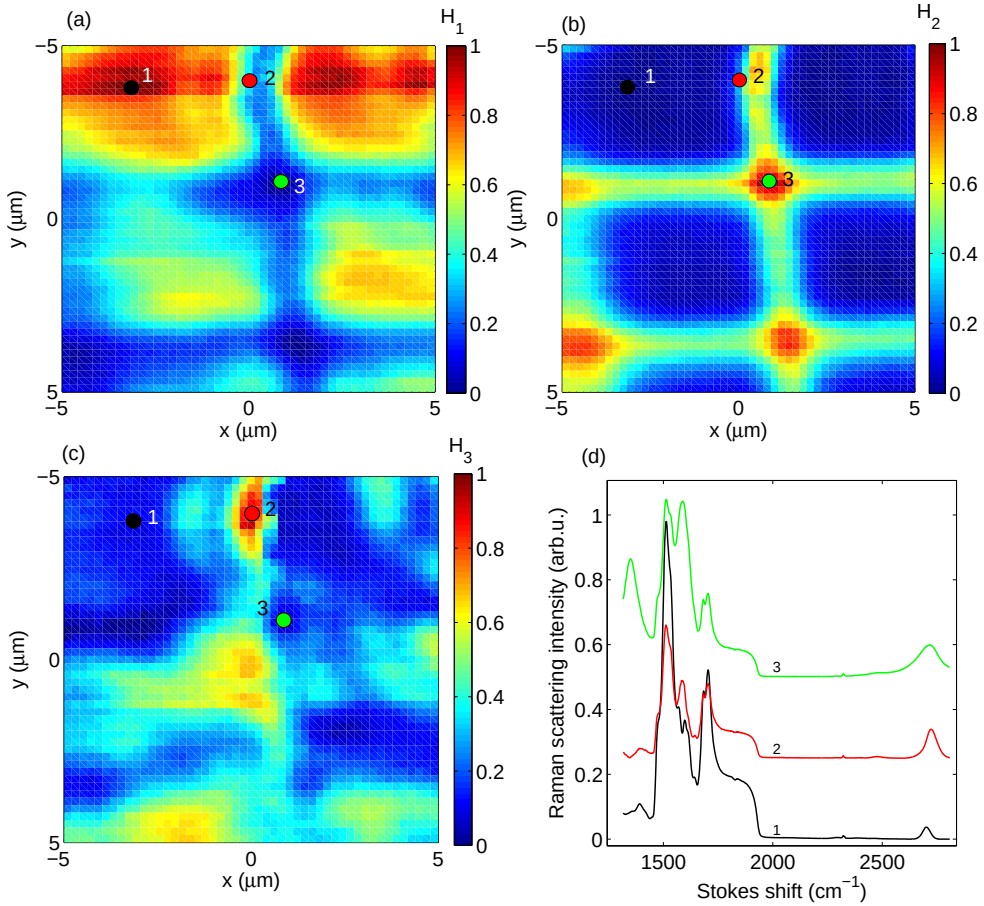

Figure 27: Spatial mapping of the Raman spectra of the Si-face sample G1. (a) Intensity of the Raman component corresponding to a single graphene layer, (b) the aC layer, (c) a bilayer graphene component. (d)Raman spectra corresponding to points 1, 2, and 3 in the spatial maps.

step-free areas, where the step-free areas are predefined by lithography. Lastly, we demonstrate that the great advantage of aC corrals is that they are selectively completely removable after growth for planar process compatibility. We now show that the recrystallized aC, evaporated prior to graphene growth, can also be used as electrical leads.

3.5 Amorphous carbon contact to graphene

Contamination related to device fabrication like lithographic resist residues are still a source of scattering and doping inhomogeneity in the graphene. Post-device fabrication forming-gas and vacuum anneals to clean the graphene of resist residues have been performed to realize higher mobility EG devices[20, 21]. However, with the usual metallic contacts, heat treatments are limited by the metal's melting point, metal diffusion and chemical reactivity. A method that permits positioning contacts prior to graphene growth is also desirable to avoid post-growth patterning. This would be especially valuable in the case of sidewall EG nanoribbons that can be grown on specific locations defined by the templated trenches etched in SiC[51, 95]. Once grown the sidewall can then be readily measured without further processing.

A contact to graphene that is stable at high temperatures is therefore desirable. Evaporation of amorphous carbon (aC) on bare SiC was demonstrated above as a SiC step-flow control technique compatible with graphene growth[85]. Owing to the good conductivity of annealed aC and its compatibility with graphene growth, we pursue evaporated aC for a high-temperature stable contact to graphene. In this section we show that evaporated aC that crystallizes into nanocrystalline graphite during EG growth forms a robust contact to the graphene with a good contact resistance.

To measure the annealed aC to graphene contact we have prepared a Si-face sample. For this, evaporated aC on the Si-face of SiC was patterned into Hall-bar contacts using a SC1813 resist photomask exposed at 365nm UV wavelength.

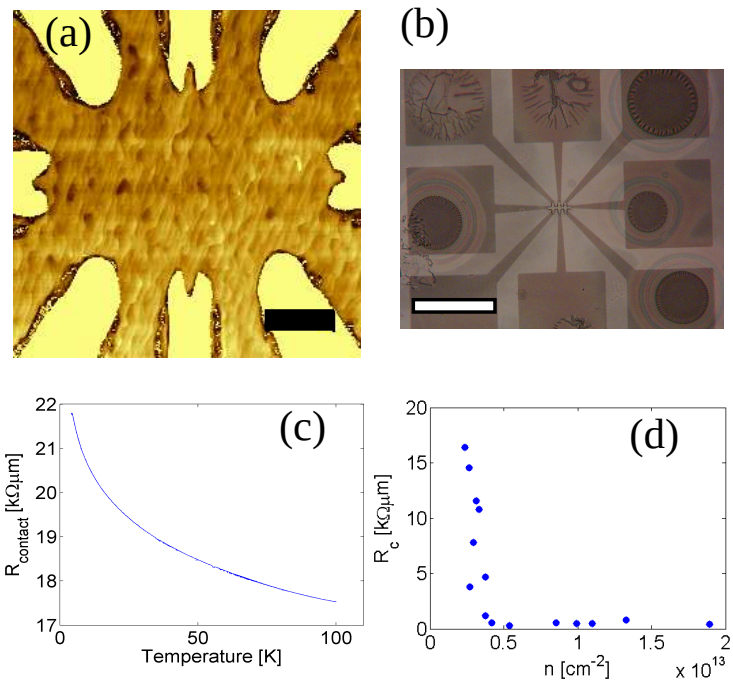

Figure 28: Si-face graphene sample with the carbon contacts. (a) AFM image of graphene with aC contact immediately after graphene growth. The scale bar is 5μm.(b) Optical micrograph of completed device. Circular features are 300nm high bubbles due to release of the intrinsic stress in the as-deposited aC film. The scale bar is 100μm. (c) Carbon contact resistance R_c to graphene measured by the TLM method as a function of temperature for graphene charge density $n = 1.4 \times 10^{12}\text{cm}^{-2}$. (d) R_c vs n at 300K.

Similarly to the aC corrals, the unmasked aC was etched in an RIE oxygen plasma for 100 seconds. Prior to growth, the samples with the patterned aC contacts were cleaned overnight and then rinsed with isopropol alcohol. Graphene was subsequently grown using the Confinement Controlled Sublimation (CCS) method [86] in a graphite enclosure in an inductively heated furnace. Samples were pre-annealed at 1150°C for 20 minutes to remove silicon dioxide, and then heated at 1550°C for 20 minutes to grow graphene.

After graphene growth, the graphene was lithographically patterned and RIE etched into Hall bars contacted by the pre-deposited carbon pads to be used as voltage probes and current leads. Figure 28 shows images of the Hall bars before (a) and after (b) patterning the graphene Hall bar channel. Step terrace widths of 0.5μm are typically seen after growth. This is consistent with free SiC step flow, since in the present Hall bar carbon pad configuration no area is enclosed by the crystallized aC (contrary to graphene in an aC corral[85]). We again note that there are signatures of stress released in the annealed aC film, manifested as 300nm high bubbles in large continuous films[78] (these are the dark round spots in Figure 28(b)). Small feature sizes (with a typical dimension less than 50μm) do not present noticeable structural changes due to released stress. Despite this stress, we show below that carbon pads make very good contact to graphene, and can sustain the thermal stress of low-temperature measurements.

The next step is to evaluate the crystallized aC to graphene contact properties. For this we have measured the 2- and 4-point longitudinal resistance and the 4-point Hall resistance of a series of Hall bars like that in Figure 28. The contact resistance between the crystallized aC and graphene is measured by the transmission line method (TLM)[15], using the Hall bar configuration with 7μm spacing between successive voltage probes and a W=2μm wide channel. The 3-point TLM resistance is $R_{TLM} = R_c + R_{sheet}L/W$, with R_c the contact resistance and R_{sheet} the graphene

sheet resistance for voltage probes separated by a distance L. The contact resistance is expected to be $R_c = R_{carbon} + R_{interface}$, where R_{carbon} is due to the carbon itself and $R_{interface}$ is the interface resistance between the graphene and the annealed carbon. Shown in Figure 28(d), the temperature dependence of R_c (measured at graphene charge density of $1.4\times10^{12}\text{cm}^{-2}$) follows closely that of the carbon pad sheet resistance shown earlier in the chapter in Figure 21(c) with a 25% increase from 100K down to 4K, indicating that the interface resistance doesn't vary much with temperature.

The plot in Figure 28(e) of the contact resistance vs. local graphene carrier density shows R_c values between 0.5kΩ and 18kΩ per μm width of the contact. The contact resistance increases by an order of magnitude at lower carrier densities. This is indicative of graphene's low density of states as a part of the graphene to carbon interface $R_{interface}$. [96] In this plot, the graphene carrier density was deduced from the Hall resistance. The charge density varies from 10^{12}cm^{-2} to 10^{13}cm^{-2}, which is consistent with the intrinsic negative doping from the SiC substrate [61], and is partially compensated by positive doping from resist residues. Consistent with this doping density[21], graphene sheet resistances of 0.5kΩ to 2kΩ are measured and room temperature mobilities around $2000\text{cm}^2\text{V}^{-1}\text{s}^{-1}$. These values are typical for EG on the Si-face[97].

In Figure 29(a), quantum Hall effect plateaus down to filling factor ν=6 are observed below 9T. The plateaus are in phase with the oscillations in the magnetoresistance as expected. The electronic mobility at 4K is $8200\text{cm}^2\text{V}^{-1}\text{s}^{-1}$, with carrier density $n = 1.4\text{x}10^{12}\text{cm}^{-2}$. The charge density determined from the slope of the Hall resistance matches that from the $1/B$ periodicity of the maxima in the magnetoresistance, showing here again that the transport measurements with aC contacts are valid and consistent. At low magnetic fields a weak (anti-) localization peak is observed below 15K. As shown in Figure 29(b) the temperature dependence of graphene sheet resistance is plotted as measured by both 4-point resistance and the TLM method.

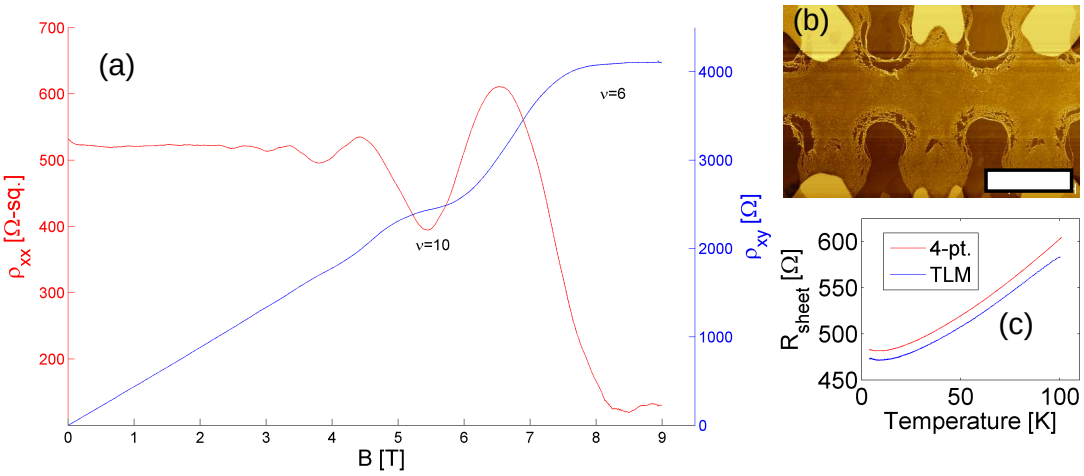

Figure 29: Carbon contacted Si-face graphene quantum Hall effect measured at 4K, with electronic mobility μ=8200cm^{2}V^{-1}s^{-1} and charge density $n = 1.4 \times 10^{12}$cm^{-2}. (a) Blue: Magnetoresistance. Red: Hall resistance. (b) AFM image of the Hall bar after fabrication by photolithography and RIE etching. The scale bar is 5 μm. (c) Sheet resistance of the graphene, measured with 4-point (red), and the TLM method (blue).

The good correspondence between both measurements further validates the TLM contact resistance measurement.

The quantum Hall effect observed here is consistent with high-quality graphene. Although the mobility is not as high as the C-face [54] graphene or post-processed Si-face graphene [21, 20] the method shows potential since this graphene has not even had any post-processing.

We have demonstrated crystallized amorphous carbon as a viable contact to epitaxial graphene on SiC. The contacts are deposited and patterned on SiC before graphene growth and crystallize alongside graphene growth by thermal decomposition of SiC around 1500°C. The carbon pads are stable at these temperatures and high quality graphene is grown along with the contacts. We demonstrate that these carbon pads make good contact to graphene, including for low-temperature measurements. Lastly, carbon contacts are an excellent candidate for post lithographic process annealing as a way to pyrolize residues or desorb impurities. Because nanocrystallized

graphite is a rather inert material, chemical treatments of fully contacted graphene samples can also be envisioned. In addition to post-lithographic treatment, the possibility of self-assembled graphene structures [51, 98, 99] being grown after contacts are placed means forming complete structures ready for transport measurements without exposing the graphene to resist. Finally, it will be interesting to investigate in detail the nature of the junction between graphene and crystallized aC. Because graphene grows while aC crystallizes, a continuous graphitic junction betwen graphene and the crystallized aC is a distinct possibility.

CHAPTER IV

BALLISTIC SIDEWALL NANORIBBONS

Graphene nanoribbons have been a topic of great interest. In the 1990's the tight-binding band structure on graphene nanoribbons was calculated, as it is a system related to carbon nanotubes[100]. What was shown was that certain armchair edge nanoribbons have an energy gap at the Fermi level and that zigzag edge nanoribbons have edge-states. If a nanoribbon with an energy gap could be produced, this would be very useful, because large-sheet graphene has no energy gap and there cannot be switched into an insulating state. Many groups sought to produce graphene nanoribbons by patterning the nanoribbons from bulk graphene with standard lithographic and plasma etching tools. These ribbons were able to be switched off and on, but ultimately no high performing field effect transistors were produced.

What was found with top-down patterned graphene nanoribbons was that edge-scattering effects reduced the performance of the devices and no energy gap was formed, but instead there is a mobility gap in the ribbons[101]. The effect is due to the line-edge roughness (LER) of the nanoribbons[18]. LER due to resist is on the order of a nanometer, but it is significant enough to dominate the scattering in 10nm wide ribbons. This is often illustrated by the Coulomb-blockade effect in some nanoribbons, where the LER is enough to create localized electronic states in the nanoribbon.

By contrast, ballistic transport in high-mobility semiconducting GaAs samples do not suffer from line-edge roughness because the channels are defined by gate-induced depletion[2], which has smooth edges due to the electrostatics. Carbon nanotubes similarly do not suffer from line-edge roughness and exhibit ballistic conduction even

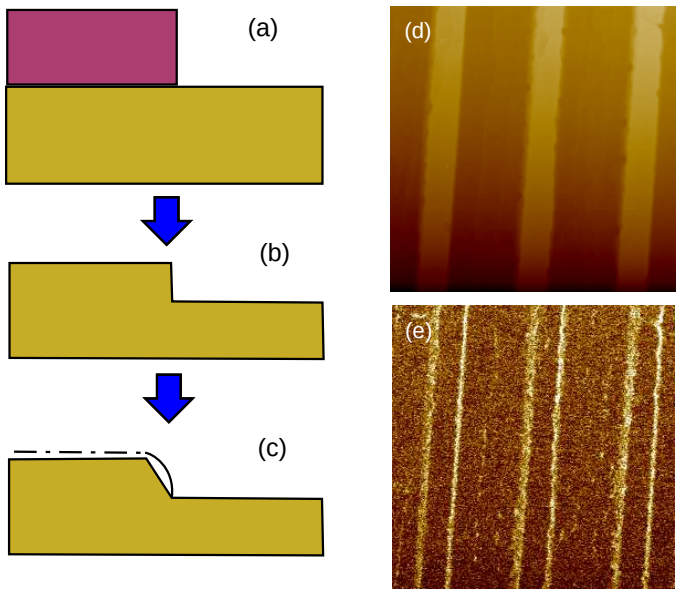

Figure 30: Growth process for sidewall graphene nanoribbons. (a) Patterned resist or hard mask to define the step edge. (b) The step is dry-etched into the SiC (c) Differential growth of graphene first onto the step edge, with a buffer layer on the base plane. This diagram is not to scale and is only an undetailed schematic of the growth results. Also shown are scanning-probe images of as-grown nanoribbons oriented along SiC $<1\bar{1}00>$: (d)AFM topography (e) EFM amplitude

at room-temperature[102]. However, carbon nanotubes also have backscattering protection due to conservation of pseudospin, as discussed in Chapter I. What is needed is a way to produce graphene nanoribbons with atomically smooth edges. LER is not the only factor affecting the quality of a nanoribbon. Besides LER, the substrate interaction (or lack thereof) and edge passivation of the nanoribbons must not induce additional scattering of the charge carriers. All of these features are possible by *growing* the graphene into nanoribbons, rather than cutting 2D graphene into shape.

4.1 Characteristics

Sidewall graphene nanoribbons (SWGNR's) on the Si-face are formed using a unique bottom-up based approach[51]. See Figure 30 for an illustration of the nanoribbon growth process. Prior to growth, mesas or trenches are etched on the Si-face (0001) face of the SiC substrate, using either masked RIE or ICP etches as described in

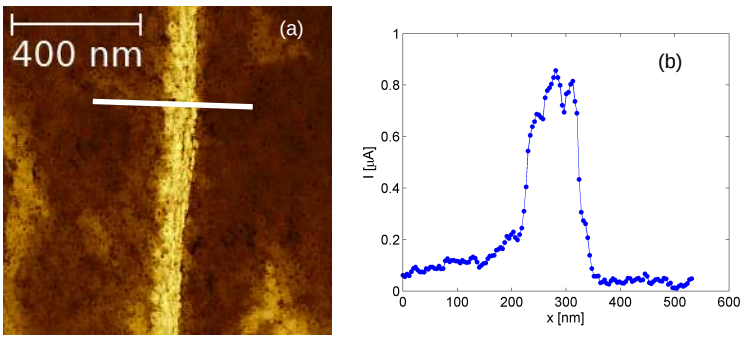

Figure 31: (a)Example of conducting AFM on a zigzag SWGNR oriented along SiC $<1\bar{1}00>$, with some overgrowth, imaged with 10nN applied to the tip. (b) Linecut.

Chapter II. The sidewall nanoribbon growth occurs in a very controlled version of the CCS method[86]. The ribbons grow first on the sidewall step and buffer layer grows on the basal plane. Typical growth processes are 1150°C to desorb the silicon oxide from the SiC, followed by graphene growth at 1480°C for 60-90seconds. The method is not limited to producing nanoribbons; many structures may be etched and grown from the step edges, including rings and Hall bars[103].

Characterization of the ribbon starts with EFM images, which is able to measure the work function and charge density difference between the graphene and buffer layer, or graphene and SiC. The width of nanoribbon may be estimated from the FWHM of the EFM signal taken transverse to the ribbon[104]. If growth is allowed to continue past the sidewall, eventually a monolayer of graphene will be grown on the (0001) basal plane. We define overgrowth of the nanoribbons to be any growth past the top edge of the nanoribbon, including naturally occurring nanoribbons that nucleate on natural steps that were not defined by the plasma etch. In addition to EFM imaging, there is a detectable Raman spectrum for the nanoribbons, where all graphene peaks are present. D-peaks are present in all ribbons, due to the symmetry breaking of the Raman scattering at the edges of the ribbons[104].

4.2 Transport Properties

The description of the electronic transport in the sidewall nanoribbons differs from that of bulk graphene, as I described in Chapter I. Due to the low dimensionality of the ribbons, there are fewer electronic states available for conduction. In fact, a single channel dominates the conduction of these ribbons[95], which is described by the Landauer equation [17, 2]. I base my description of the transport on Datta's excellent textbook on mesoscopic transport. Following the Landauer approach, the conductance for a one dimensional conductor with N channels is written:

$$G = \frac{e^2}{h} \sum_{n=1}^{N} g_n T_n \tag{14}$$

where T_n is the transmission probability for the electron to enter each mode from the contact reservoir, and g_n is the degeneracy of the mode. Simplifying for a single conducting channel with unit degeneracy the conductance is written:

$$G = \frac{e^2}{h} T \tag{15}$$

The prefactor $G_0 = e^2/h$ is the *quantum of conductance*. G_0 corresponds to 39μS or about $R_0 = 26\text{k}\Omega$. For a perfectly ballistic channel (no scattering along the channel) the conductance is therefore independent of the length of the channel. The conductance corresponds to an equilibration of the electron's energy at the contact, thus the resistance measured is referred to as a *contact resistance*.

An important case of reduced transmission between a contact reservoir and the conducting channel is observed while measuring conducting AFM, which was introduced in Chapter II. As mentioned there, the contact resistance of the tip, which may have a very small contact area, usually dominates the 2-point resistance measurement. Shown in Figure 31 is an example of conducting AFM, where the current on the ribbon biased at 1V is no more than 1μA, giving a 2-point resistance of $1\text{M}\Omega$. This indicates a transmission efficiency $T = 0.25$ for the platinum tip in this instance. The transmission efficiency is expected to increase as more force is applied to

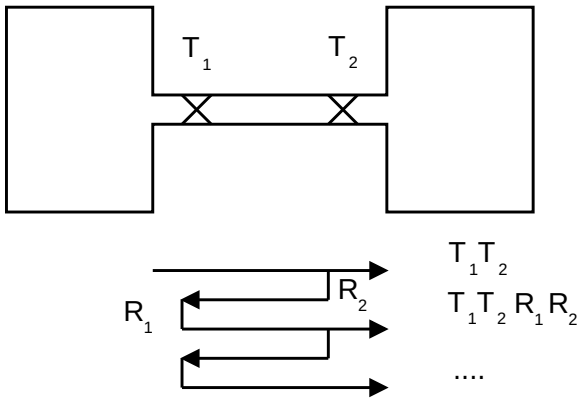

Figure 32: Multiple scattering from two scatterers in a ballistic channel, each with transmission coefficient T_1 and T_2, following the argument by Datta[17].

the tip, or for a larger contact area. The tip material could have a significant effect on transmission as well.

In addition to scattering of carriers from the contact reservoir to the channel, we can also account for scattering if there are scattering centers in an otherwise perfect channel. A single scatterer would split the conducting channel into two perfect conductors, and thus alter the overall transmission. But suppose there are two scatterers, each with transmission T_1 and T_2. We might first say that the cumulative transmission is just $T_{12} = T_1T_2$, but that is incorrect because reflections between the scatterers are not considered. Following Datta[17], neglecting phase information we can include successive reflections and retransmissions by writing a series expansion. Each contribution to the forward transmission of the electron, as I show in Figure 32, is added to give the total transmission:

$$T_{12} = T_1T_2 + T_1T_2 + T_1T_2R_1R_2 + T_1T_2R_1^2R_2^2 + ... = \frac{T_1T_2}{1 - R_1R_2} \tag{16}$$

Rewriting the final form of (16) suggests that we can relate the cumulative transmission and transmission of each scatterer by the following form:

$$\frac{1 - T_{12}}{T_{12}} = \frac{1 - T_1}{T_1} + \frac{1 - T_2}{T_2} \tag{17}$$

This implies that multiple scatterers can be calculated by adding terms of $\frac{1-T}{T}$. Again

following Datta[17], we can say that if there is a linear density ν of scatterers in the channel of length L, each with a transmission probability T. By adding the total number of scatterers $N = \nu L$ as was done in (17), their cumulative transmission is given by the relation:

$$\frac{1 - T(L)}{T(L)} = L\nu\frac{1 - T}{T} \tag{18}$$

This accounts for multiple reflections between all scattering centers in the channel. For this distribution of scatterers in the conducting channel we can think of a mean-free-path L_0, where $L_0 = T/\nu(1-T)$: The transmission probability through the entire channel is written:

$$T(L) = \frac{1}{1 + \frac{L}{L_0}} \tag{19}$$

The resistance is then:

$$R(L) = R_0\left(1 + \frac{L}{L_0}\right) = R_{contact} + R_{diffusive} \tag{20}$$

The resistance is meaningfully written as a quantum contact resistance $R_{contact}$ due to the limited number of conducting modes, as well as a diffusive component $R_{diffusive}$ that originates from scatterers in the channel, designated by L_0. The mean-free path is related to the density of scatterers along the sample. The physical meaning of L_0 in a 1D channel is the distance over which the carrier has a 50% chance of transmission. For comparison, mean-free-paths exceeding 10μm were observed on the sidewall graphene nanoribbons grown and measured by a four-probe technique in UHV[95]. A quality bulk-graphene sample may have mean-free-paths on the order of 100nm. In bulk metals the mean-free-path is closer to 10nm. What I intend to show next is how the mean-free-path is reduced by processing residues and environmental contamination in these ribbons.

4.3 Clean systems

This section is about the surface cleanliness of contacted sidewall graphene nanoribbons, which I consider extrinsic to the properties of the SWGNR's. Unlike the 4-probe

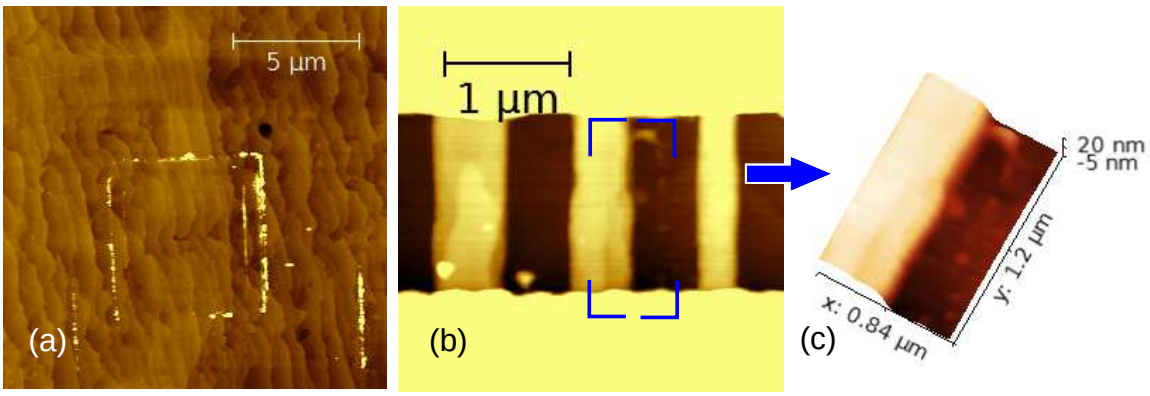

Figure 33: (a)Example of residues swept from an area by contact-mode AFM. This image was taken using non-contact AFM. (b) Example on a sidewall nanoribbon. $0.5\times1.0\mu$m area was cleaned in prior images, with swept residues accumulated as indicated by the blue brackets. (c) 3D rendering of an enlargement of bracketed area.

UHV work done in Hannover, or the ribbons contacted by large graphene pads[95], contact to the sidewall nanoribbon samples presented in this chapter involves using standard metal lift-off techniques. While the graphene patterning line-edge roughness scattering was avoided in these ribbons and the substrate-nanoribbon interactions are probably reduced on the sidewalls, scattering due to process residues on the ribbons is not avoided. It is well-known that processing residues, particularly that of PMMA e-beam resist, cause electronic scattering on graphene devices[20, 21]. The same is true for processed graphene nanoribbons, and the challenge now is to preserve the intrinsic properties of the nanoribbons with improved processes. It is critical to the further development of graphene electronics that processing residues are avoided, and that is why I devote a section to understanding what contributes to the scattering and how it may be removed.

To illustrate the pervasiveness of residues on lithographically contacted nanoribbons, I show here some images of residues on graphene samples. See Figure 33 for an example of the cleaning effect using contact mode AFM. To compare to others[105], tip cleaning was first attempted on bulk graphene in subfigure (a), where the piled-up residues are clearly seen as the bright lines from previous smaller AFM scan windows.

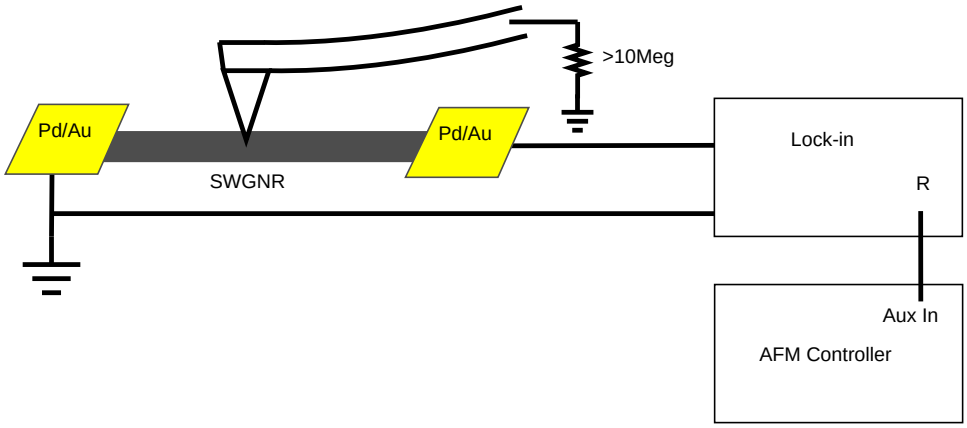

Figure 34: Measurement setup for the mechanical tip cleaning effect and invasive probe microscopy.

In subfigure (b) we also show an example on a single SWGNR, with the swept area indicated by the brackets. This demonstrates that the nanoribbons can be mechanically cleaned, with the intent of reducing the number of scatterers on top of the ribbon.

While mechanically cleaning a SWGNR grown along SiC $<1\bar{1}00>$, the two-point resistance of the ribbon was measured, as depicted by the schematic in Figure 34. See Figure 35(c) and (d) for 2D plot of the resistance of the ribbon. The slow-scan direction is shown by the large arrow. By sweeping an AFM tip the resistance of the resistance of the ribbon is lowered. As demonstrated in Figure 35, the resistance of the ribbon ultimately approaches 26KΩ as residues are swept away. Despite additional scans over the ribbon, no resistance below 26kΩ was observed, consistent with the quantum contact resistance to the single conducting channel.

This is direct evidence for adsorbed scatterers on lithographically processed sidewall nanoribbons. Sweeping the tip at small force setpoints will not damage the graphene itself, but is an effective "broom." Successive sweeps on the same ribbon in a short amount of time will have not lower the resistance any further. As I show will in the next cleaning experiment, additional impurities can adsorb onto the ribbon from the environment, which will increase the resistance over a longer period of time.

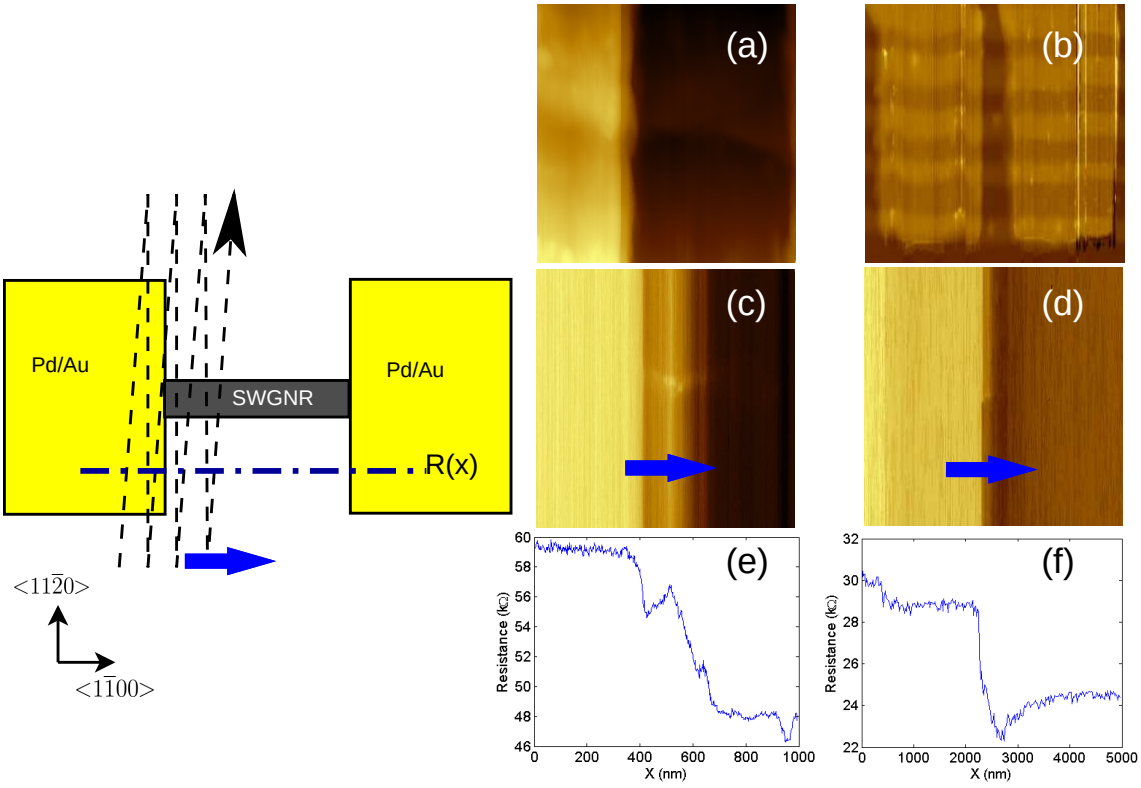

Figure 35: In-situ measurement of mechanical cleaning of sidewall graphene nanoribbons. The blue arrows indicate the slow-scan direction of the AFM tip. (a) AFM topography on Day 1. (b) AFM topography on Day 2. (c) Color map of the 2 point resistance of the ribbon on Day 1 (d) Color map for Day 2 (e) Drop in resistance on Day 1 (f) Drop in resistance on Day 2, culminating in a resistance of 25kΩ.

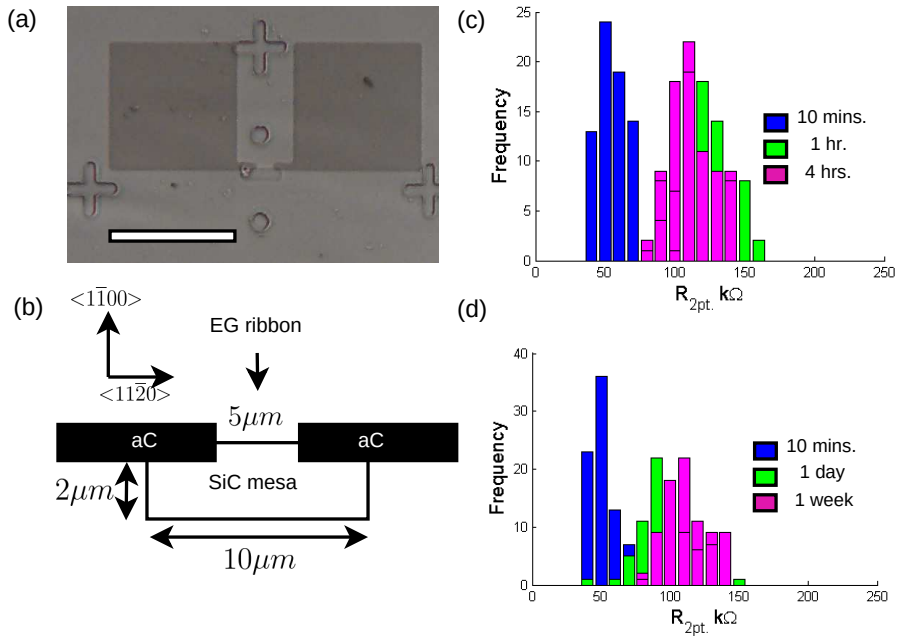

Figure 36: Vacuum desorption experiment. (a) Optical micrograph of a carbon contacted sidewall nanoribbon, one of 81 measured. (b) Schematic of the region measured, with ribbon orientation according to the SiC directions. (c) 2-point resistances measured immediately after growth. (d) 2-point resistances immediately following a 1000°C vacuum anneal to desorb water and other environmental impurities.

Here I attempt to estimate the effect of the scattering due to the PMMA residues. If we take, as an example, the size of PMMA molecules to be about 2nm, we can estimate the maximum linear density of scatterers to be $\nu = (1/2)\text{nm}^{-1} = 500\mu\text{m}^{-1}$ if the molecules are adsorbed end-to-end. A typical micron-long ribbon with resist residues on it that introduces scattering has a 2-point resistance of 120kΩ, exceeding R_0=26kΩ before cleaning, such that $L_0 = 280$nm. Assuming each molecule has a similar scattering probability, using $L_0 = T/\nu(1-T)$ we calculate that the product νL_0 gives a reflection probability for each molecule of about $1 - T = 0.8\%$. This is probably reasonable, since PMMA molecules do not have a strong dipole moment.

An additional experiment was performed to illustrate the adsorption of environmental impurities, as depicted in Figure 36. Using the techniques developed in Chapter III, amorphous carbon was deposited onto the etched SiC steps prior to nanoribbon growth. SWGNR's were then grown using the standard recipe in the presence of the carbon. The length of the measured ribbon, oriented along SiC $<11\bar{2}0>$, is about 5μm, and the longer 14μm segment on the rest of the etched mesa (raised SiC area, as opposed to a trench, which is a hole etched into the SiC) is assumed not to contribute to the transport. Within ten minutes of removal, 2-point resistance measurements were made on 81 nanoribbons, followed by 1 and then 4 hours later. The sample is then annealed at 1000°C for 30 minutes at 10^{-7}mbar to desorb contaminants. 2-point resistances are again made within 10 minutes followed by 1 day and 1 week after removal from the vacuum furnace.

What was observed was that immediately after growth, the resistance of the ribbons was centered around 40kΩ, followed by a saturation to a broader distribution centered around 110kΩ. The spread in the initial distribution is partially due to the speed at which the operator could measure the ribbon resistances. The saturation in resistance is expected from the adsorption of moisture onto the sample surface, consistent with observations on 2-dimensional graphene[106]. Using equation 20 to estimate the mean-free-path from the resistance, L_0 after prolonged exposure is about 1μm, a factor of four longer than for a SWGNR with PMMA present. Before adsorption L_0 in the 40kΩ ribbons is closer to 9μm. This shows that as-grown nanoribbons are very good conductors, but exposure to the air very quickly introduces scattering that can be reversibly removed.

The conclusion made here is that, although processing residues and environmental exposure reduces L_0 in these nanoribbons to around 1μm or less, good ballistic sidewall nanoribbons are still grown using the CCS technique, as shown by the ribbons with $L_0 = 9\mu$m as contacted by carbon. Looking forward, what is needed is a

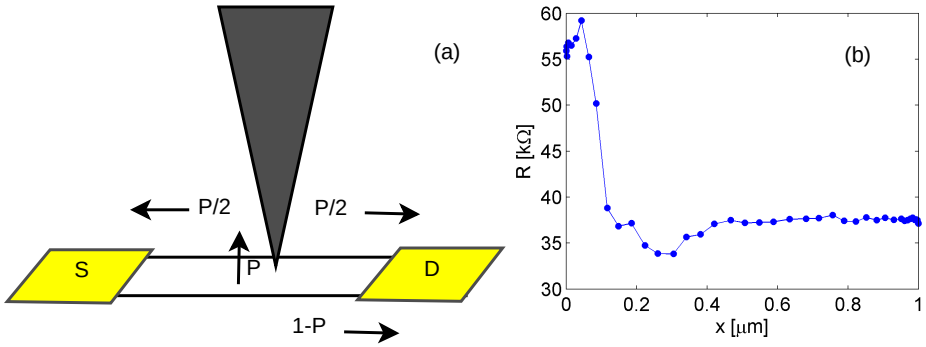

Figure 37: (a)Diagram of transition probabilities during for the single-probe invasive probe effect. (b)Test of the invasive probe effect recorded using an unsynchronized AFM setup. Distance x is estimated from time series data.

method to prevent scattering centers from ever contacting these ribbons, as if they are in a very clean environment like UHV. Eventually the use of carbon contacts and dielectric capping techniques, prepared in-situ after graphene growth, will enable residue-free graphene protected from the laboratory environment, in a manner similar to the buried semiconductor heterostructures.

4.4 Invasive Probe Microscopy

A kind of scattering that is unique to ballistic conduction can be introduced by a voltage probe, called the invasive probe effect. Depending on how strongly the voltage contact is coupled to the 1D ballistic channel, the invasive probe effect will increase[107]. This can also be accomplished by contacting the channel with an ungrounded probe. Following the argument by Baringhaus et al.[95], as shown in Figure 37, if there is some probability P for an electron to enter the probe, then the electron has probability $P/2$ of being ejected either forwards or backwards in the channel. The total probability for the electron to enter the drain contact becomes $T = 1 - P/2$. The conductance for a ballistic sidewall ribbon with injection efficiency T_{in} becomes:

$$G = G_0\left(1 - \frac{P}{2}\right)T_{in} \tag{21}$$

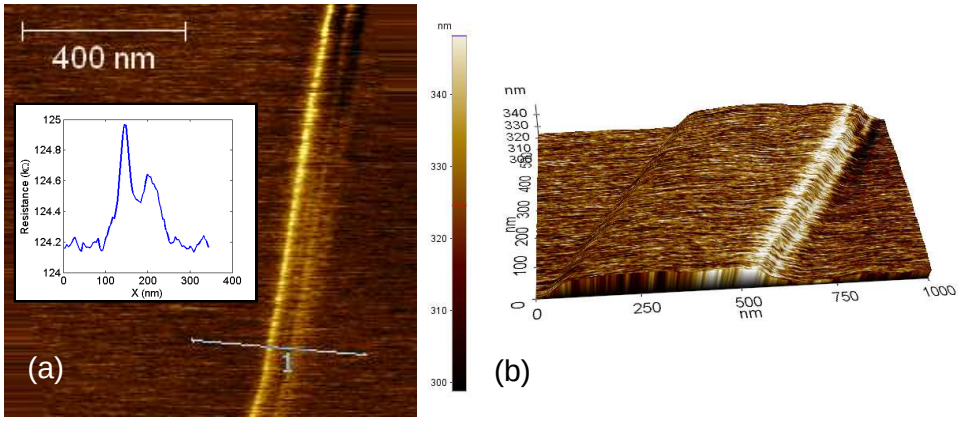

Figure 38: (a)Example of invasive probe microscopy. Effect is observed on both edges of the zigzag nanoribbon oriented along SiC <1$\bar{1}$00>. 200nN force using conducting NaDiamond tip. (b) 3D overlay of the resistance map onto the topography.

For a perfectly invasive contact ($P = 1$) a doubling of the conductance is expected, as demonstrated by the four-probe experiments. If there are scattering centers in the ribbon, designated by density ν, the situation can be more complicated. As long as the density of scatterers is low enough such that ballistic segments remain, the invasive effect of the tip only depends on the injection efficiency P into the tip. This is sensible for a 1D conductor, since the segments between scatterers may be thought of ballistic resistors in series. Following the argument in equation 18, $\frac{1-P}{P}$ must be added to $L\nu\frac{1-T}{T}$ in order to calculate the total transmission. This means the total change in resistance for a ribbon ΔR with a low density of scatterers is then added to the total resistance $R(L)$:

$$R = R_0\left(1 + \frac{L}{L_0} + \frac{P/2}{1 - P/2}\right) = R(L) + \Delta R \quad (L_0 >> d_{tip}) \tag{22}$$

The relevant size scales are the mean free path L_0 in the ribbon and the size of the probe d_{tip}. The effect of the invasive probe ΔR will be reduced if multiple scatterers are present within the contact area of the tip. In the limit of a classically diffusive conductor $L_0 << d_{tip}$, where $L_0 \approx 10$nm, the contact should have no effect on the overall resistance since the diameter of a typical probe is of the order 10nm or larger. The expression for ΔR in between the ballistic and diffusive limits likely depends on

the microscopic details of the scattering.

The invasive prove effect can be extended beyond a static probe by using an AFM system. As previously shown in Figure 34, a conducting AFM probe is set up with a very high resistance to ground (>10MΩ). The purpose of the resistance is to bleed off any accumulated charge. See Figure 37 for an initial line scan of the invasive probe effect. A 1μm wide line was scanned across a 40nm wide ribbon at 0.1Hz. Unlike the data that follows, this data was taken with a DC measurement was not synchronized to the X and Y positions in the microscope. The force on the tip was comparatively quite high (>200nN) compared to a typical imaging force of 10nN, and the tip itself was unstable, yielding a very poor topographic signal. As the tip passes across the nanoribbon, the ribbon resistance jumps from 35kΩ to 60kΩ, corresponding to R_0. Notably ΔR never exceeds R_0, as expected from equation 22. This means that in spite of the poor topography, the tip did make very good contact with the ribbon, with $P \approx 1$ as calculated in equation 22.

To synchronize the measurement of R with the X and Y positions on the AFM system, a lock-in amplifier technique is to used to input the measured resistance to an auxiliary port on the Park AFM system, as shown in Figure 34. See Appendix B for a detailed description of the setup. See Figure 38 for resistance images. Since the AFM tip is also cleaning the ribbon after each scan over the ribbon, thereby reducing $R(L)$, the images are leveled by subtracting $R(L)$ from each line. Leveling provides better contrast of the invasive probe effect in the images. Unlike the first line scan in Figure 37, care is taken to obtain a useful topographic image using a 10nN setpoint. What is known immediately from this image is that resistance change due to the invasive probe is at the edges of the ribbon. This includes both the top and the bottom edge of the ribbon. Not including any diffusive effects, P is calculated from ΔR using equation 22, such that P =0.058 at the top edge and $P = 0.029$ at the bottom edge, indicating a less than perfectly invasive probe.

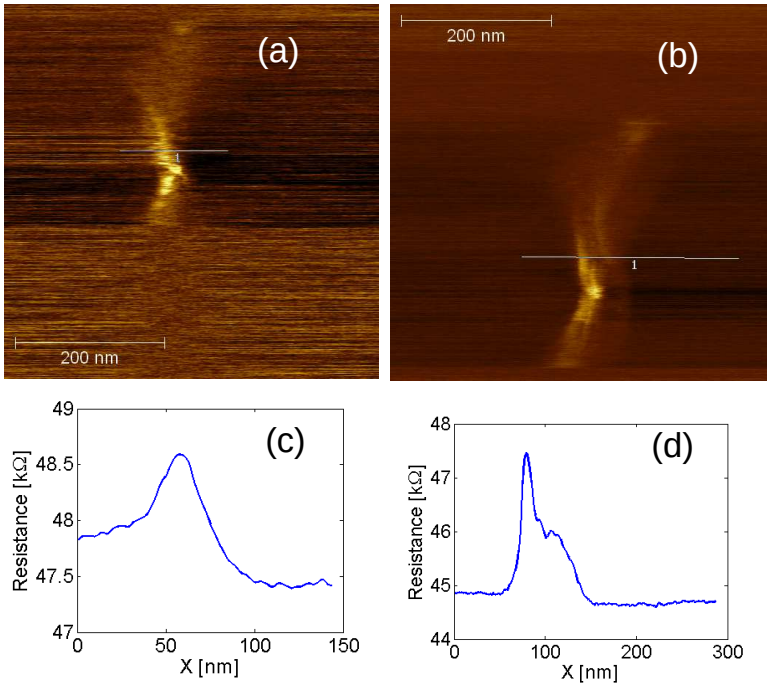

Figure 39: Effect of increased force on the tip in subsequent images, on a zigzag nanoribbon along SiC <1$\bar{1}$00>. Spatial map of ΔR at 10nN in (a),with a linecut in (c). Spatial map of ΔR at 60nN in (b), with a linecut in (d).

As another test of the invasiveness of the probe, the force on the tip is increased. First 10nN, with ΔR=0.5kΩ was measured, and then 60nN with ΔR of 3kΩ was measured, as shown in Figure 39. This increases P from 0.03 to 0.2, which is very clear. Another feature visible in the images in Figure 39 is that at 10nN (a) only the top edge of the ribbon is visible. At 60nN (b) features from the bottom edge begin to become visible. The increased force has probably made the bottom edge more visible as the tip is forced into the bottom edge of the sidewall step. In many of the invasive probe images, only the top edge is visible. The fact that increased force has accessed the lower edge is an indication that the geometry of the tip and sidewall bottom edge is a limitation of the measurement.

One other piece of information gained from the invasive probe microscopy is the spatial location of the ballistic channel. If the electrical contact between the ribbon surface corresponds to the point at which topography is measured, then as seen in

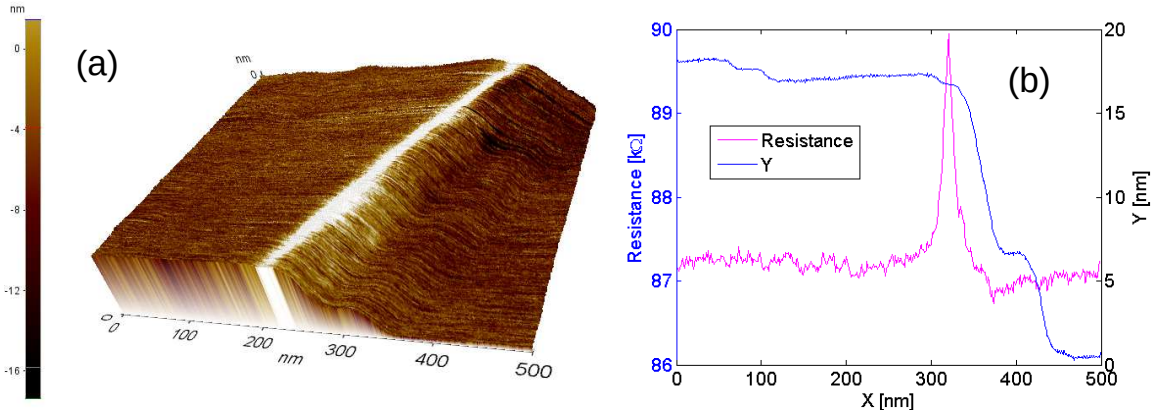

Figure 40: Detailed spatial dependence of the invasive probe effect, imaged using a Pt/Ir coated tip with 60nN force, on a zigzag nanoribbon oriented along SiC $<1\bar{1}00>$. (a) 3D overlay of ΔR over the topography. (b) Line profile of ΔR and the topography.

Figure 40, the peak in ΔR does not correspond to the topographic step edge, but instead to the graphene edge. The peak is very sharp with a FWHM of 12nm. The peak at the top of the step does agree with TEM showing that the graphene is least bound to the SiC near the top of the step[119]. STM measurements indicate the presence of graphene throughout the sidewall, but the strength of coupling between the graphene and the SiC on the sidewall is undoubtedly very important in determining the electronic properties of the ballistic state.

There are many more experiments proposed based on this technique, based on different nanoribbon morphologies and different AFM tips. If there is no tip effect, then the response to the invasive probe at the edges of the graphene nanoribbon is evidence that points to the ballistic channel being at the edge of the nanoribbon. Diffusive conductors are not expected to have an invasive probe effect, which is seen by lack of response from the gold contacts to the nanoribbons and from higher resistance nanoribbons. As discussed in the previous section the resistance of the ribbons will increase over time due to re-adsorption of contaminants on the SWGNR. This may bear directly on the measurement of the invasive probe effect on these samples as other scattering. This may be a reason to repeat the scanning invasive probe experiments

in vacuum or a controlled inert atmosphere.

In conclusion, the invasive probe microscopy technique provides a unique spatial mapping of the ballistic conducting state in SWGNR's. It is also another confirmation of the presence of a ballistic conducting state in these SWGNR's. The indications here are the ballistic conducting state is localized to the top and bottom edges of the nanoribbons. The structural and electronic details of this state await experimental determination.

CHAPTER V

JUNCTIONS

As was mentioned in the introduction to Chapter IV, bulk graphene does not have an energy gap, and therefore cannot be used as a switch. Bulk graphene itself cannot be switched off, and there is not good transport evidence for semiconducting graphene nanoribbons. There have been attempts to modify graphene into a material with a bandgap, via functionalizing the graphene lattice to have sp^3 hybridized components in a manner similar to diamond or by periodic modulation of the graphene lattice[108, 109]. These attempts are unlikely to produce sufficiently high carrier mobilities, though, due to the unordered bonding or adsorption of the molecules on the graphene. Going to materials beyond graphene, there has been considerable interest in molybdenum disulfide, for instance[110]. MoS_2 has been shown to have reasonable switching characteristics with lower carrier mobilities than graphene. Scalable epitaxy of high quality MoS_2 has not been demonstrated, however.

This chapter will begin by exploring the Si-face buffer layer as candidate for semiconducting switches, which like graphene on SiC can be scalably grown. Besides the buffer layer, junctions placed into sidewall graphene nanoribbons are shown as another candidate for electronic switches, which has very interesting prospects.

5.1 Buffer layer junctions

The Si-face buffer layer, also known as zero-layer graphene or the interface layer, has not received the same level of attention as has graphene for use as an electronic material. As I point out here in this section, the buffer layer may be usable as a semiconductor from what is shown in the literature and experiments presented

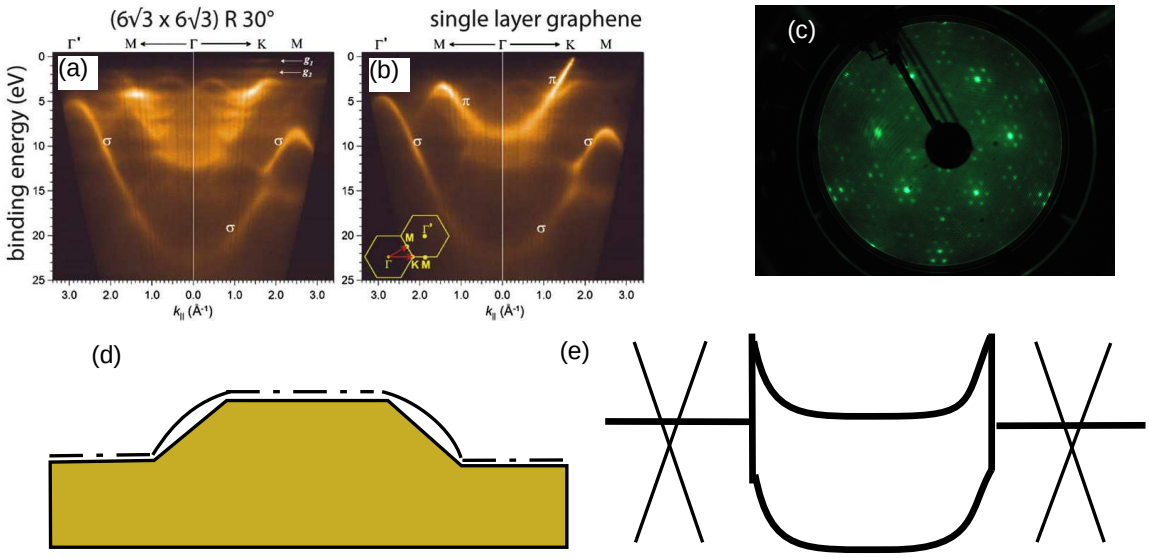

Figure 41: (a)ARPES measured on the buffer layer, taken from [111]. (b) ARPES measured on Si-face graphene, also from [111]. (c) LEED on a buffer layer sample, taken on a CCS grown sample, showing the $6\sqrt{3} \times 6\sqrt{3}$R30° reconstruction. (d) Possible seamless graphene-buffer-graphene junction (e) Band alignment suggested between graphene and the buffer layer conduction and valence bands.

later in the chapter. First, this is evidenced by the ARPES data around the K-point of the graphene, shown in Figure 41[111]. From the ARPES in subpanel (a) a bandgap around 1.0eV is indicated, unlike the linear bands that meet at the Dirac point in subpanel (b). Further evidence for an energy gap is available in the STS measurements, which show an energy gap of 1.0eV[95, 112]. 1.0eV is smaller than the 3.4eV bandgap of 4H or 6H SiC, so it is clear that there is a contribution from the buffer layer and not just the SiC.

The buffer layer can be hydrogen passivated by heating it to 900°C in 1 atmosphere of pure hydrogen[113]. Oxygen passivation is also possible by heading the buffer layer in air above a few hundred degrees[114]. Raman, ARPES, and transport measurements of the passivated buffer show that the quasi-freestanding graphene decoupled from the substrate are electronically the same as graphene. See Figure 42 for a conducting AFM image and Raman spectra example of hydrogen passivated buffer layer. These samples were grown using the CCS growth method as a test bed to show

that the buffer layer grows all over the sample surface. The samples were hydrogen passivated around 900°C in pure hydrogen, following Starke's method[113]. A hydrogen passivated graphene sample has a sheet resistance of about 6.5k$\Omega\,\square$, which is comparable to a typical graphene sample sheet resistance, showing indeed that passivated CCS grown buffer layers have the structure of graphene.

In order to understand the electronic structure of the buffer layer, here I try to describe what is known about its structure. The buffer layer is most often seen to have a $6\sqrt{3} \times 6\sqrt{3}$R30° reconstruction with respect to the SiC surface[23, 111]. As was shown, the structure of the buffer layer is of a carbon rich layer with essentially the same structure as graphene, but with some form of interaction or structural modification to the graphene lattice that gives rise to the $6\sqrt{3} \times 6\sqrt{3}$R30° reconstruction [115]. The $6\sqrt{3} \times 6\sqrt{3}$R30° could be energetically stable due to rehybridization of the sp^2 bonds in the graphene lattice towards sp^3 bonding with the SiC, rather than by strain[116]. What is clear is that the graphene layer can be distorted or altered in a very ordered way, as shown by STM and LEED measurements [95, 112]. The structural order is important, because unlike the disordered alteration of the graphene by chemical functionalization or adsorption[108, 109], the observed order of the buffer layer ought to form a good semiconductor, if the buffer layer is prepared properly. This bandgap indeed would be attributable to the periodic alteration of the graphene lattice[117].

If the buffer layer is a semiconductor, it is conveniently used with graphene to form devices, and here I explore how that could be. STM and TEM images directly show that graphene on the sidewall facets can contact the (0001) face and form into the buffer layer[95, 118, 119, 120]. The junction between semimetallic graphene and semiconductor buffer layer would be a Schottky barrier. Seamless and atomically smooth two-dimensional junctions are interesting as this means very thin (<10nm) Schottky barriers are possible, due to the electrostatics of thin conducting layers.

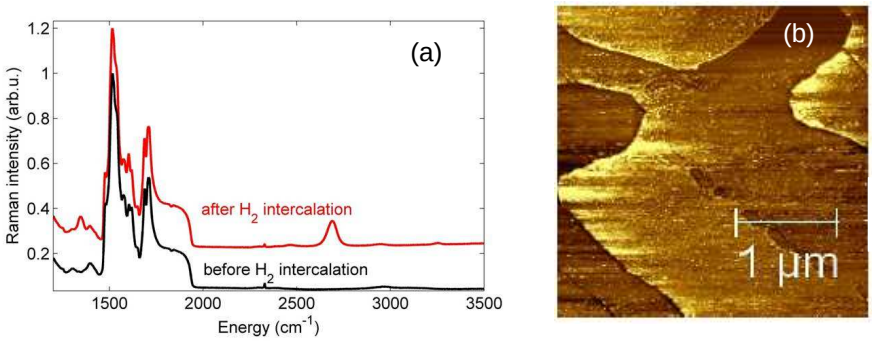

Figure 42: Example of hydrogen passivated buffer layer. (a) Raman Spectra showing the graphene 2D peak after hydrogen passivation. (b) Conducting AFM image showing that the passivated buffer layer is now a conducting graphene surface with a 100mV bias between the tip and sample.

The electrostatics of thin layers differ from bulk junctions due to the fringing electric fields, which are up to two orders of magnitude higher than the expected bulk field as discussed by Kunc et al[43]. Thin Schottky barriers are interesting from a transport point of view, because it means there is likely a strong tunneling contribution to the electronic transport[43] through the barrier. Furthermore, the junction would be tunable due to the semimetallic graphene contacts, similar to what has been shown with the graphene to silicon barristor[121] and between C-face graphene and a SiC 2DEG[43].

In order to better understand the incomplete understanding of the buffer layer, I show here some transport measurements made on graphene-buffer graphene junctions. These junctions exhibit switching behavior and gating behavior, which indicates that the buffer layer is a promising direction for graphene electronics.

5.1.1 Regraphitization Method

Described in this section are attempts to produce graphene to buffer layer junctions. What is desired is a seamless contact between the Si-face graphene and its buffer layer. What is developed here is a method to first grow graphene and then buffer, that I call regraphitization. A back-to-back junction structure is formed by regraphitizing buffer

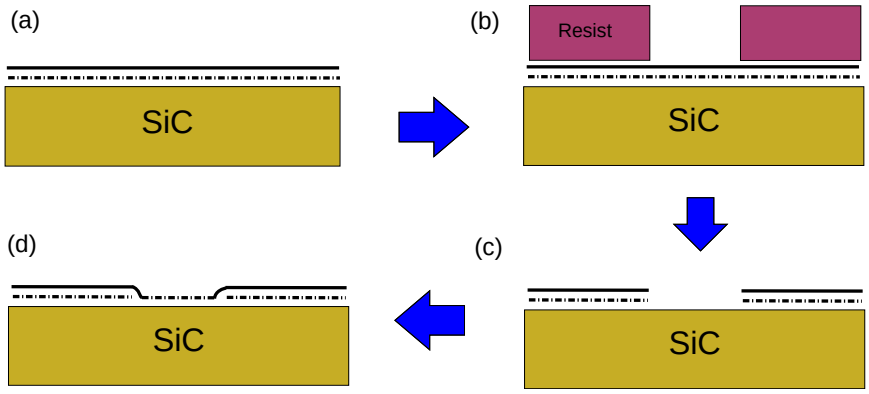

Figure 43: The regraphitization process. (a) Growth of a single-layer graphene on Si-face SiC. (b) Pattern an etch mask to protect the graphene contacts. (c) Oxygen RIE to remove graphene from the channel. (d) Re-growth at a lower temperature to grow the buffer layer.

between two graphene contacts. The transport through these junctions are studied using DC current versus voltage (IV) curves measured at various temperatures and in various configurations.

The formation method for these junctions are very similar to the back-to-back junctions on the C-face of SiC, though without the presence of the buffer layer or sidewall nanoribbons[43]. See Figure 43 for an illustration of the regraphitization process. Growth proceeds first (a) with a continuous coverage of a monolayer graphene. The graphene is then patterned into contact shapes as in (b) using oxygen plasma RIE. The sample is carefully soaked in acetone overnight and rinsed with IPA as in (c). Finally, growth at lower temperature occurs to form buffer layer between the junctions.

Samples are grown on vanadium compensated SiC(0001) from II-VI corporation. The vanadium compensated SiC is very important in these buffer layer junction experiments because defect-level compensation of the Fermi level (as used in SiC supplied by CREE) can be annealed away at high (>1700°C) growth temperatures. The Fermi level can then approach the conduction or valence band of SiC making it more conducting and thus electrically short the buffer layer junction, as determined by

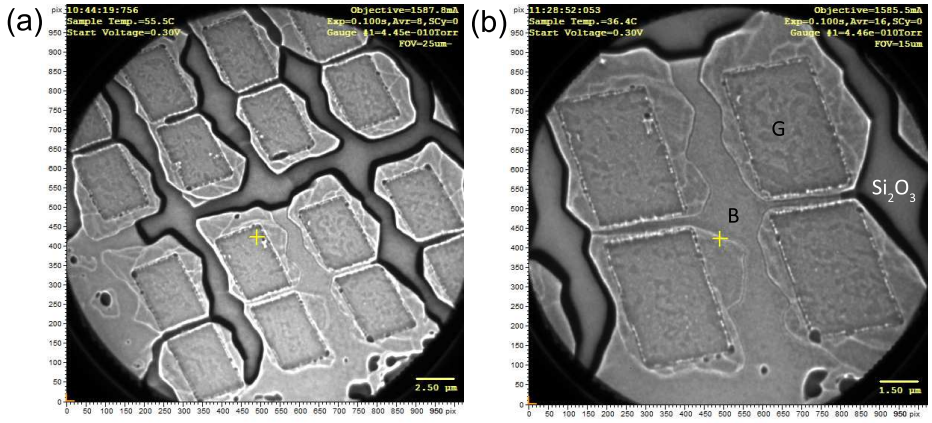

Figure 44: LEEM images of regraphitized junctions without HF processing, showing the presence of silicon dioxide (Si_2O_3) after regraphitization. (a)View of eight junctions, showing oxide between six pairs of graphene pads. (b) Detailed scan on the two junctions with buffer layer. Buffer indicated by B, graphene by G, and the oxide is labeled by Si_2O_3.

transport measurements on a SiC heated to 2000°C[122]. The initial graphene layer is typically grown at 1550°C for twenty minutes. Raman and EFM show what is typical of monolayer coverage. Before regrowth, the sample must be dipped in hydrofluoric acid (HF) to remove silicon dioxide from the surface. As shown by Low Energy Electron Microscopy (LEEM) in Figure 44, Si_2O_3 forms on the sample surface, most likely due to the oxygen plasma RIE. HF consistently removes the oxide, unlike annealing, which was unable to remove the oxide.

For regrowth of the buffer layer, a series of test growths were tried to find a buffer layer temperature that showed interesting transport properties. Growth temperatures between 1250°C and 1400°C were attempted with a growth duration of 20 minutes. No attempts were made to prevent inclusion of SiC step edges and sidewall ribbons in the junction areas, which are later found to contribute to the transport. A growth temperature of 1350°C was settled upon, giving I-V curves that showed greater than 10nA at less than 10V bias across the junction. Lower growth temperatures required up to 100V to see conduction and higher temperatures showed evidence of graphene

shorting the junction at low bias (<1V).

Because there are SiC steps between the graphene pads used in the regraphitization experiments presented in this section, and because nanoribbons can grow on the sidewalls of the steps, there may be graphene nanoribbons in addition to the buffer layer between the graphene pads. EFM measurements shown in Figure 45 indeed show the presence of nanoribbons in the junction area. The question of whether these nanoribbons are contributing to the electronic transport must next be addressed, since the nanoribbons are expected to be highly conducting relative to the buffer layer, and the geometry of the junction would be set by the width of the nanoribbons and their separation, rather than being set by the patterned size and separation of the graphene pads.

Typical sizes patterned for the buffer layer junctions (schematic in Figure 46(b)) to be regrown were $W = 4\mu$m wide and at various lengths from $L = 180$nm to 5μm long. The I-V characteristics are found to be independent of the patterned graphene pad geometry, but instead the I-V turn-on voltage, where I=10nA, correlates to the step orientation between the graphene pads as shown by the histogram in Figure 45(b). This histogram is taken from a sample where the SiC steps are parallel to half of the 66 pairs of source and drain graphene pads, and where the SiC steps cross between the graphene pads. Junctions with steps traversing the pads have lower turn-on voltages whereas when the steps are parallel to the pads the turn-on voltage is higher. To probe the spatial extent of these junctions scanning Kelvin Probe Microscopy (described in Chapter II) is measured on the devices while biased, shown in Figure 45(a). As described previously, SKPM is sensitive to the potential drop across the sample surface. The bias voltage is swept through both positive and negative bias to observe the voltage drop. Conducting AFM was measured on the junctions as well to determine which portions of the junction are more conducting.

The conclusion is that nanoribbons were grown in between the graphene pads in

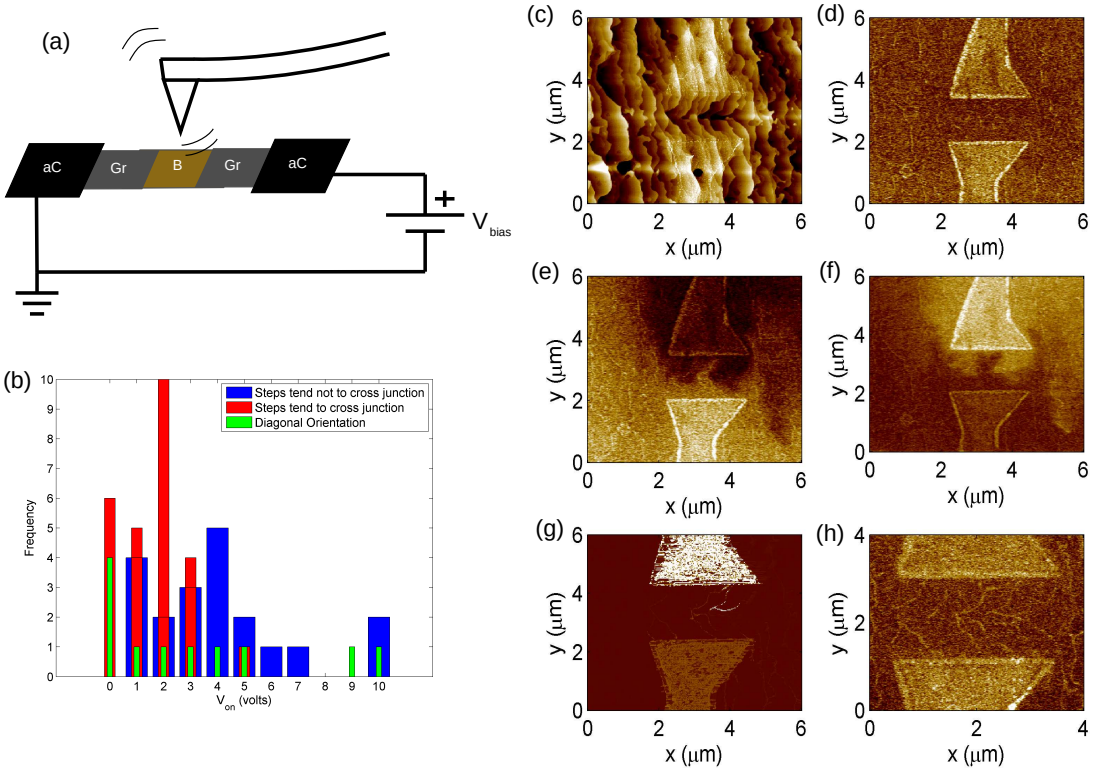

Figure 45: Demonstration that nanoribbons between the graphene pads contributes to the transport in regraphitized junctions. (a) Setup for measuring a series of scanning-probe images to describe the potential drop and conductivity of regraphitized nanoribbon-buffer-nanoribbon junctions. (b) Junction turn-on voltage histogram, with V_{on} defined by $I = 10$nA, for graphene pads where the nanoribbons tend to cross the junctions or run parallel to the junctions (c)NC-AFM topography of the junction area. (d) Scanning Kelvin probe microscopy (SKPM) with no bias applied to the junction. (e) SKPM with positive bias (f) SKPM with negative bias (g)Conducting AFM image of the junction area, showing higher conductivity of the nanoribbons. (h) EFM image detail on the junction area.

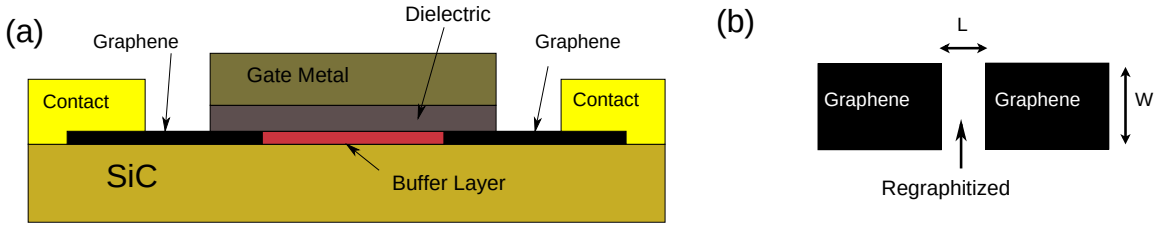

Figure 46: (a)Schematic profile of a gated regraphitized graphene-buffer-graphene junction. (b) Schematic layout of regraphitized junction of width W and length L.

all the regraphitized devices presented in this section. The forward and reverse bias measurements in Figure 45(e) and (f) show spatial inhomogeneity in the voltage drop between the graphene pads that is not expected from uniform conduction between the patterned graphene pads. If no nanoribbons were between the graphene pads, there would not be much variation of the potential along the width W of the graphene pads. The conducting AFM shown in Figure 45(g) also shows there are two conducting ribbons separated by roughly 100nm that are in the same location as the potential drop. EFM and SKPM taken with no bias on the junction in Figures 45(d) and (h) indicate that the distance between the sidewall nanoribbons between the graphene pads in this example is about 100nm, instead of the much longer 2μm distance patterned between graphene pads.

Knowing the general structure of the junctions, we now focus on the transport of the junctions. See Figure 46(a) for a schematic of a completed buffer layer device. The regraphitized junctions were measured using the cryogenic system between 4K and 300K. A few of these IV curves measured at different temperatures are plotted in Figure 47. The junction in Figure 47 (c) is indicative of a disordered graphene nanoribbon, which has a linear I-V high temperatures and a nonlinear I-V at low temperature[18]. The junctions in Figure 47(b) and (d) deviate distinctly from graphene nanoribbon behavior showing highly nonlinear behavior at all temperatures over a bias range greater than 1V. Another feature that is clear from the IV curves is that the IV is asymmetric in reverse and forward bias. This is due to inequivalent

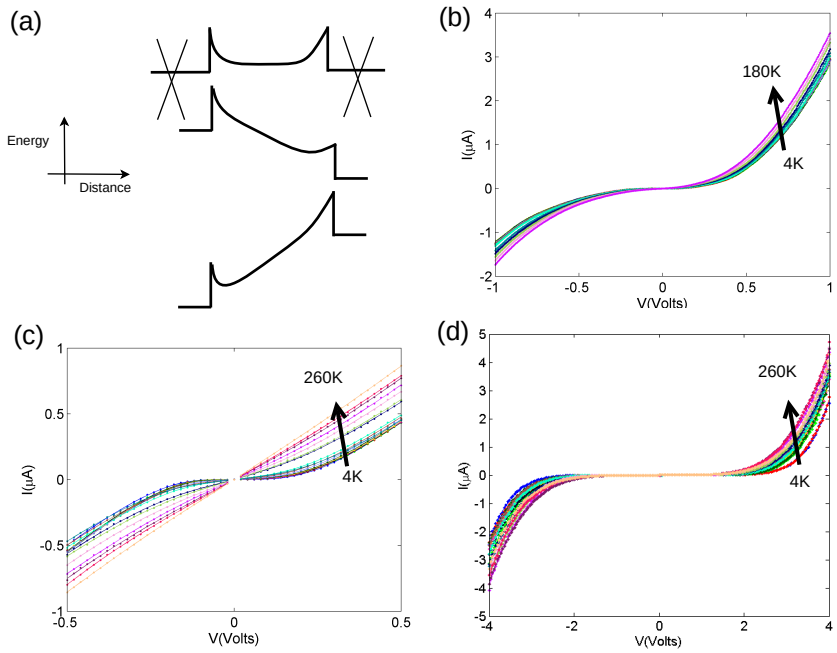

Figure 47: (a) Schematic energy diagram of two inequivalent barriers between graphene contacts to buffer layer in equilibrium and forward or reverse bias. (b)-(d): I-V curves versus temperature on regraphitized junctions.

barriers at the buffer and graphene interface, shown in Figure 47(a).

What is clear from the IV vs. T data is that the conduction in these devices is nearly temperature independent, unlike the junctions on the C-face where thermally activated transport into the SiC occurs between graphene pads[43]. This is one indication that transport is through a buffer layer and not into the SiC. Since a barrier is expected at the graphene to buffer interface, this also rules out thermal activation over the barrier dominating the transport, so we expect tunneling injection into the buffer layer channel. Furthermore, due to the asymmetry of the IV's, tunneling must contribute to the transport. The other possible temperature independent transport effect is space-charge limited current, a channel effect rather than a contact effect. Both effects can be present simultaneously[123], meaning that the IV curve can be asymmetric even though space charge limited current alone is symmetric with respect to bias. Again, tunneling is a necessary feature of the transport due to the asymmetry

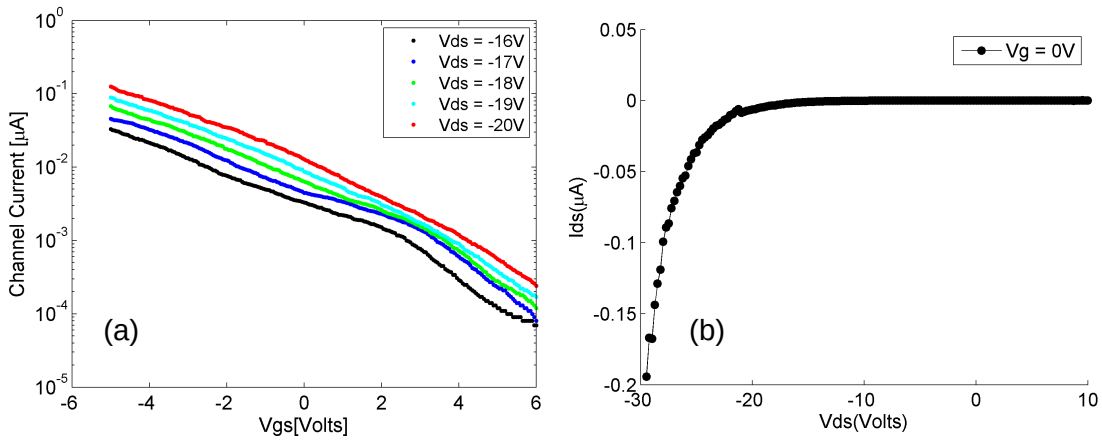

Figure 48: (a) Gate effect of a graphene-buffer-graphene junction measured at 300K. $\frac{I_{on}}{I_{off}}$ =10^3 (b) I_{ds} curve measured at 300K. The large asymmetry in the I_{ds} curve as compared with the devices in Figure 47 is probably due to the aluminum oxide layer altering one of the barriers.

of the I-V curves. Modeling the junctions with both effects for the low dimensionality of the junctions is beyond the scope of this work, though it may be necessary for a better understanding of the transport.

One other measurement made on these graphene-buffer-graphene junctions is to gate the junctions. For this, aluminum oxide dielectric is slow-evaporated onto a junction, followed by a faster aluminum gate contact evaporation, described by Figure 46(a). The residual oxygen gas in the e-beam evaporator chamber provides the oxygen source in the aluminum oxide. The $W = 2\mu$m wide graphene pads are $L = 2\mu$m apart, and this effect was measured on four devices. Shown in Figure 48(b) is the channel IV curve of one of the best device, showing a large asymmetry between forward and reverse bias, again an indication of a barrier effect. Shown in Figure 48(a), varying the gate voltage between -5V and 5V shows a 10^3 ratio between on and off currents, showing that there is a gate effect. Gate leakage was less than 1nA in this measurement. The gating effect is an indication that the barrier height or width can be tuned.

One other thing that is clear about these junctions is their relative structural

stability. Unlike the oxide dependent C-face devices[43], these junctions have been measured over a period of months while retaining essentially the same IV characteristics. This could be due to the stability of the buffer layer and because the buffer layer acts as a barrier to contamination. Unlike metal nanojunctions, there are no electromigration effects since the bonding energies are high, which allows high electric fields at the interfaces. What would be interesting to see is a graphene-buffer-graphene junction with a well-defined geometry. Some attempts to make these junctions in the following sections are described, as the regraphitization method presented here does not control the placement of SiC steps and any graphene grown from its edges.

To conclude this section, the buffer layer has the potential to be a good semiconductor with gate-tunable transport through its barrier to graphene indicated. Further exploration of the buffer is promising. What is promising about these junctions is that it is not a standard metal-semiconductor junction, but a *semimetal*-semiconductor junction. This provides an additional parameter to tune in the transport barrier, similar to the graphene-silicon barristor [121]. It is difficult to draw a conclusion about the overall nature of the buffer layer from the relatively complicated structure of the regraphitized nanoribbon and buffer junctions at this point, but more can be done with more consistently prepared junctions.

5.2 Interrupted sidewall nanoribbons

I now introduce another route towards producing graphene based switches in addition to the regraphitization method. From the work in the previous section, I know that graphene nanoribbons and tunneling play a role in the transport. Here I attempt to tunnel directly between graphene nanoribbons, though with a more controlled geometry than the regraphitization method. Etched sidewall grown graphene nanoribbons are chosen because of their controlled growth and because interesting transport effects

are expected from the ballistic conduction in the nanoribbon. The reduced backscattering in the nanoribbons may be apparent in the transport properties of a narrow junction in the nanoribbon.

Inserting a tunneling barrier into a nanoribbon requires the formation of a very small physical gap, which is challenging for the lithographic processes used today. Vertical tunneling between graphene layers has been realized using thin insulating layers with some ease[124]. Thin tunneling barriers are relatively simple to achieve in layered junctions, like layered graphene junctions or the Esaki tunneling diode, whereas etching a gap this narrow within a graphene nanoribbon is a challenging task for lithography. The necessary tunneling distance can be estimated from the de Broglie wavelength λ of the electronic wavefunction, which has a tail length λ at an energy barrier of height E. Let's assume a relatively high energy barrier of E=1eV to illustrate the example. For a massive electron, say $m^* = 0.1m_e$, then $\lambda = h/\sqrt{2m^*E} \approx 4$nm is expected for the wavefunction tail. For massless Dirac particles with velocity c^*, as expected in graphene, $\lambda = hc^*/E \approx 5$nm is expected. Since tunneling may be thought of as the overlap of electronic wavefunctions, tunneling gap distances in the range of 4-10nm are reasonable from the estimated lengths.

We propose here to use AFM-based lithography. In principle, preparing a nanogap is possible with either e-beam lithography or even careful bottom-up growth methods to grow a small section of buffer layer between ribbons. AFM lithography is excellent for in-situ measurements and very narrow linewidths are readily achieved. With the AFM system a sharp probe is used to cut the nanoribbons. As was mentioned in Chapter IV, because the tip may not penetrate the bottom edge of the ribbon on the sidewall, the entire nanoribbon may not be cut. From the geometry for a 28° sidewall step and a tip end-diameter of 10nm, a gap of 4Å is estimated between the end of the AFM tip and the bottom corner of the sidewall step, which is significant enough to prevent good contact without relatively high forces on the tip.

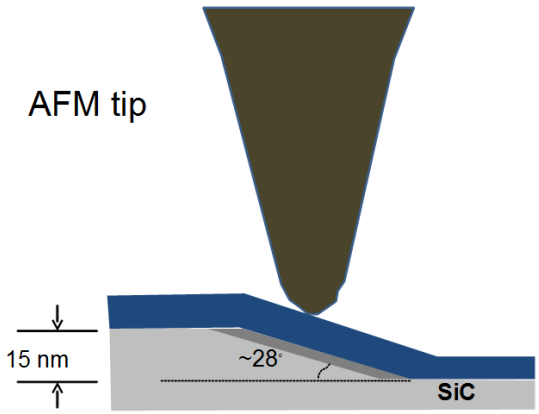

Figure 49: Schematic of set up for AFM lithography. With electrochemical lithography there a bias between the tip and the nanoribbon.

5.2.1 Physical scratching of nanoribbons

Some groups have attempted to pattern bulk graphene by physically ripping the bonds with AFM[125], but to date I have not seen anything considering graphene nanoribbons in the context of producing nanojunctions. Cutting likely depends on the lattice orientation of the graphene relative to the cutting direction and the presence of defects to reduce the forces necessary to rip apart the graphene lattice. Two types of AFM tip were used to cut, SiN based and diamond based in order to demonstrate the physical scratching method.

In the first series of measurements the SiN tips were chosen for their high hardness compared to readily available Si AFM tips. First the nanoribbon was cut using a force of 40nN, and subsequently the IV curve was measured ex-situ within 10 minutes. These cuts proved to be difficult to reproduce, and measurement was further made difficult because within one positive to negative cycle of the bias voltage the junction became insulating, with a resistance higher than 1GΩ. I show here in Figure 50(a) the best example of this junction. To reduce the effects of the degradation, the bias was only swept through one polarity. This junction remained stable for 2 hours because the bias voltage was not swept back through 0V. As soon as bias is swept back to the

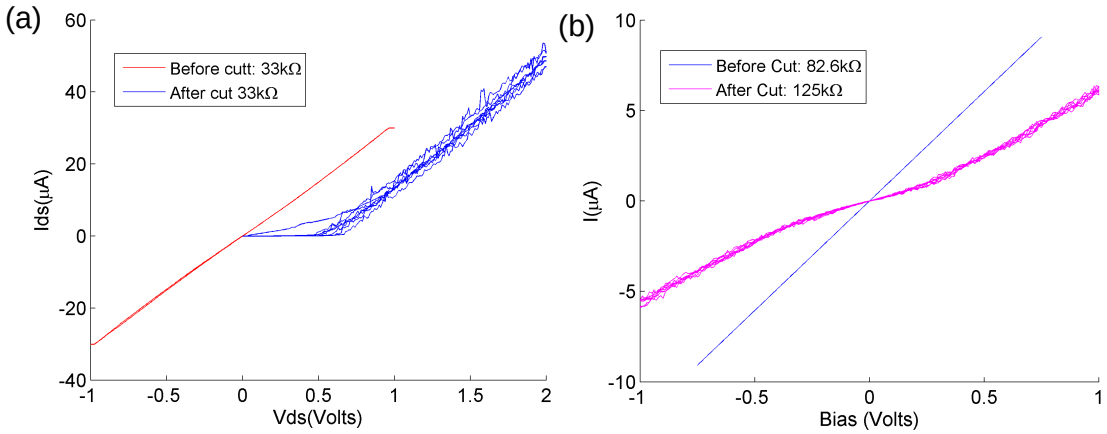

Figure 50: Examples of I-V curves from physically scratched of ribbons oriented along SiC <1$\bar{1}$00>. (a) 82kΩ initial resistance. (b) 33kΩ initial resistance.

negative region the junction becomes insulating. (Although the junction is physically symmetric before the I-V scan, the symmetry is broken as soon as bias is first swept in either polarity.) As seen from Figure 50(a), the original ballistic resistance of 33kΩ is intact after the bias is high enough to switch the junction into an on-state.

The second series of experiments used Nadiamond^{TM} diamond coated Pyrex AFM tips. Diamond was chosen specially because its superior hardness. These tips have an average end diameter between 10 and 30nm. The cutting procedure starts by mounting the sample and wirebonding to an AFM compatible chip carrier. For precise comparison an IV curve of the ribbon is measured before forming the nanogap. 10mV bias is applied to the ribbon, for roughly 300nA depending on the resistance of the nanoribbon. As the tip is scanned across the ribbon the current is monitored and the tip is stopped from scanning once the current through the ribbon drops below 1nA.

A few techniques were tried to see what IV curves result. Initially for tip setpoints of 150nN multiple passes of the tip are required. This results in weakly conducting IV curves, even at high bias. For tip setpoints of 180nN to 250nN the ribbon is cut with a single pass of the tip. I would say these are the best IV curves because the on-state resistance is closest to the resistance of the nanoribbon before forming the barrier.

See Figure 50(b) for an example of the best IV curve. Above 250nN only a single pass is necessary, but again the junction is weakly conducting. Single-pass cutting of the ribbon is sensible because the AFM stage drift does not broaden the width of the cut area, unlike a multiple cut junction. Furthermore, the best conduction comes from the narrow cuts, which are expected from the lowest necessary force on the tip. In the best cases, the original resistance of the graphene nanoribbon is nearly recovered, indicating almost no backscattering of the electrons at the junction.

As mentioned, some of the junctions degraded into an insulating state after several cycles of the bias voltage. This appears to be electrochemical changes to the structure of the tunneling barrier. An electrochemical modification of the junction is not unreasonable considering a) the presence of reactive molecules in the atmosphere (oxygen or water for instance) and b) the high electric field at the junction. For 1V applied to a 5nm wide junction this is 0.2V/nm, which is similar to the electric fields within molecules. This means the stability of the ends of the cut ribbons is extremely important and the formation of a stable junction requires bonding that is not affected by the chemical environment of the junction at the electric field strength in the on-state.

What is clear from these experiments is that graphene-nanoribbon based junctions presents a better controlled placement of the junction, unlike the regraphitization method where the junction between nanoribbons could form anywhere between the graphene pads. Unexpectedly, the junctions also exhibit highly-efficient tunneling in the on-state, because the original differential conductance $\frac{\partial I}{\partial V}$ of the nanoribbon is preserved. Higher on-state resistances would be expected from the insertion of a tunneling barrier in a conductor due to scattering by the barrier. More will be said about this at the end of the chapter.

5.2.2 Local electrochemical oxidation of nanoribbons

An alternative method to produce a tunneling junction that may not leave as many dangling bonds on the ends of the graphene ribbons is desirable. One method is to locally change the graphene into graphene oxide. This may be more stable than physically cutting ribbons as the gap is filled with graphene oxide material.

Table 3: Parameters used for successful electrochemical oxidation of nanoribbons.

Segment	Tip Bias	Relative Humidity
B1-B2	-3V	70%
B2-B3	-3.3V	68%
B3-B4	-3.25V	71%
A1-A2	-2.8V	65%
A2-A3	-3.9V	76%

Based on methods used for bulk graphene [126], conducting AFM is used in conjunction with the water meniscus formed at the end of the AFM tip to locally oxidize the graphene. The size of the affected area and the reaction rate therefore depend on the bias voltage and the humidity. The local humidity in the AFM acoustic enclosure was raised to between 50 and 70% humidity using a water reservoir within the AFM acoustic isolation chamber. See Table 3 for the cutting parameters that worked. The conducting AFM probe was scanned with a standard force of 10nN in all lithography attempts mentioned here. Current through the ribbons is monitored as the ribbon is physically modified by the tip, as was done in previous cases. Though the nanoribbon is biased to monitor the junction formation, this bias voltage on the ribbon is only 10mV, as compared to the 3V between the ribbon and the AFM tip so that only the bias between the tip and ribbon and not across the ribbon is considered.

Once again the IV curves are measured in-situ immediately following the oxidation. See Figure 51 for I-V scans of the system measured before and after junction formation. Similar behavior to what was seen with the scratched ribbons, with the on-state resistance of the ribbons approaching that of the original resistance of the

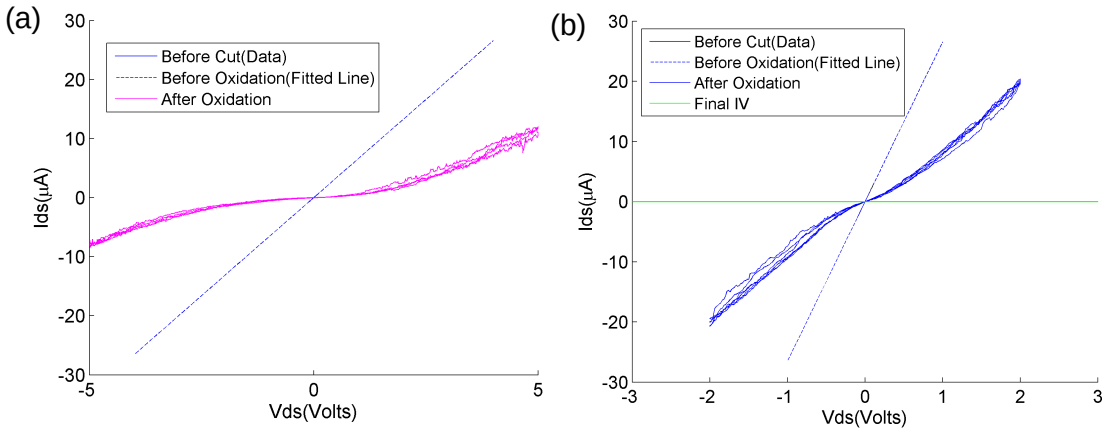

Figure 51: Examples of I-V curves after local electrochemical oxidation of nanoribbons oriented along SiC <1$\bar{1}$00>. (a) An initially 143kΩ nanoribbon with an on-state resistance of 300kΩ after junction formation. (b) An initially 40kΩ ribbon with an on-state resistance of 100kΩ after forming a junction. Evolution of the oxide increases the junction resistance to 833MΩ after an hour.

nanoribbon. The difficulty with this method is that the oxidized area evolves, where the switching behavior has an on-state resistance similar to the unmodified ribbon but ultimately having a resistance of gigaohms at all bias voltages after a day has passed. As was considered with the physically scratched nanoribbons, what has evolved is most likely an electrochemical effect that degrades the physical gap in the ribbons, such that the gap material is not well defined.

The characteristics of the IV curves are all despite the differences in formation of the junction. What is clear is that this tunneling mechanism is present without regard to the formation method of junction, and carrier backscattering is suppressed in the on-state of the junction. This is an indication that the on-state resistance is more a property of the nanoribbons and not the barrier. The suppressed backscattering in the junction is probably related to the chirality of the charge carriers in the ribbons. Somewhat related calculations have been made based on gated ideal graphene nanoribbons.[127, 128] These studies determined protection against backscattering at the energy barrier. Though the details of these calculations are not the same as for sidewall nanoribbons, what is clear is that a backscattering protection mechanism is

commonly attributed to graphene nanoribbons, and would be expected given the exceptional ballistic transport seen in these nanoribbons. This backscatter mechanism can have a profound influence on transport through a tunnel barrier.

Further experiments may involve preparing the samples in vacuum or an inert environment, similar to the regraphitized graphene-buffer junctions from the beginning of the chapter. Understanding how to created permanent chemical bonds at the junction will increase its stability. Beyond preparing stable junctions, finding a way to gate these highly efficient switches is desired, because the subthreshold rises are expected to exceed the 60mV/decade limit in thermionically activated devices used in the semiconductor industry. A faster and reproducible lithographic method, perhaps using standard e-beam techniques, is also desired to produce the barrier region. Finally, the role of the buffer layer and the SiC in the nature of the junction is not clear, and understanding the buffer layer may also improve stability of these junctions.

CHAPTER VI

CONCLUSION

Following the previous work on EG on SiC, this thesis is about harnessing top down and bottom up approaches to form new graphene devices. If graphene is to be a viable platform for electronics, stable and mass-produced structures are necessary. Processes that preserve the integrity of the graphene's transport must be used as well, meaning cleaner or protected fabrication process as compared to traditional bulk-semiconductor processes. This includes pre-growth structuring of the SiC and contacts to the graphene.

In addition to the templated growth from etched SiC steps, evaporated carbon based structures are an additional tool for structured growth. Amorphous carbon as a step-flow control mechanism demonstrated, showing that aligned placement of the SiC steps beneath the graphene surface is possible. Carbon electronic contacts are demonstrated to work with graphene growth. In both the step-flow control experiments and the carbon contacts the graphene grown is proved to be of high structural and electronic quality.

Improvement to the formation of nanojunctions between the ballistic ribbons are important, and it may be possible self-assemble such junctions using guide SiC templates. As indicated by the regraphitization experiments, further understanding of the buffer layer formation can lead to better 2D semiconductors. Temperature independent transport is measured on these devices, strongly suggesting tunneling processes. Gated junctions show high on-off ratios, suggesting tunable barriers.

Evidence for backscattering protected tunneling is presented from the nanometer wide tunneling gaps etched into sidewall graphene nanoribbons, formed from the

high-quality nanoribbons. Evidence for the high quality of these ballistic nanoribbons at room temperature and ambient conditions was presented by invasive probe experiments. The spatial properties of the long carrier mean-free path states are probed using invasive probe microscopy, and further exploration of these experiments will lead to greater understand of these electronic states. Cleaning experiments demonstrate that structurally these nanoribbons are high-quality, and that a method to protect them from processing residues and the environment is necessary.

All the research here points towards promising nanoelectronic structures based on EG on SiC. Perhaps the greatest takeaway from the research presented here is that *graphene structures should be self-assembled* and *graphene structures should be protected after growth.*

APPENDIX A

HIGH TEMPERATURE STABLE SAMPLES

This appendix explains how to create EG on SiC samples that can be used in a variety of machines before and after the graphene growth. These instructions are written to use e-beam lithography, but the applicable lithographic steps may be replaced by photolithography.

A.1 Formation of SiC alignment markers

Proper pattern alignment is important for e-beam lithography. High step heights are necessary if high Z materials cannot be used for alignment with an e-beam.

1. MMA/PMMA Pattern
2. 100nm Ni deposition and lift-off
3. 600nm deep SiC ICP etch
4. Strip the Ni by ultrasonicating in nitric acid, then clean sample with acetone and IPA

A.2 SiC Structures for nanoribbons

It is better that the SiC is structured prior to the carbon contact formation, because SiC structures are more robust in the oxygen plasma used to etch aC, whereas aC will be aggressively etched by the SF_6 based plasmas.

1. PMMA or MaN pattern for mesas or trenches
2. SF_6 etch to desired depth (typically 15nm)

3. Ultrasonicate in acetone and IPA to strip the resist.

4. Strip the resist by carefully immersing in acetone overnight, or ultrasonicating, followed by a rinse in IPA

A.3 Carbon Contact formation

As discussed in chapter III, annealed amorphous carbon is an ideal contact for high temperature stable samples.

1. 40nm deposition of aC

2. MaN 2403 pattern of aC into contact shape

3. 150 sec O2 plasma to etch aC

Cleaning of the samples proceeds with immersion of the sample into acetone and subsequently isopropyl alcohol. The graphene growth recipe is in principle the same as for samples without already prepared structures. Hydrogen etching is not possible on these structures as the etching procedure removes carbon atoms and will remove the aC, as confirmed by attempting to etch an aC test sample. Hydrogen etching will also remove nanostructures etched into the SiC.

APPENDIX B

INVASIVE PROBE MICROSCOPY

This appendix gives detailed instructions on how to measure invasive probe microscopy with the Park Systems XE-70 AFM.

1. Prepared a wirebonded device on the AFM stage and connect it to the lock-in amplifier.

2. Connect the X channel of the lockin to AUX1 on the Park system. Connect the Y channel to AUX2.

3. Before performing a scan, include the AUX1 and AUX2 inputs to be record by the Park software.

4. It is important to balance between scan rate and lock-in excitation frequency so that the excitation signal is not so high as to see capacitive effects, but not so low that the integration time τ in the lock-in amplifier is too long for a single pixel. Scanning at 0.2Hz with 256 pixels gives 200ms per pixel. τ must be below that. The excitation frequency cannot be above 1kHz due to capacitive losses from the cables. (BNC has a capacitance of 100pF/m, which with 1MΩ so we expect a pole around 10kHz.) 103Hz is found to be a good balance that is faster than the AFM scan rate, but over a decade below the cutoff frequency.

APPENDIX C

FURNACE VAPOR PRESSURE

This calculation is intended to estimate the silicon vapor pressure equilibrium in the CCS graphene furnace.

Flux F due to a pressure:

$$F = \frac{1}{A}\frac{dN_{vap}}{dt} = \frac{1}{4}\rho v_{RMS} \tag{23}$$

Estimate ρ from the ideal gas equation. $v_{RMS} = \sqrt{\frac{3k_BT}{m_{Si}}}$.

$$\rho = \frac{P_{vap}}{k_BT} \tag{24}$$

Set up the rate equation to include particles introduced by the vaporization from the sample and interior crucible surfaces. Assume that the crucible has a similar Si vapor pressure as the sample. Particles adsorbed depend on actual pressure P. Particles lost depend on the leak rate.

$$V_{tot}\frac{dP}{dt} = \left[\frac{dN_{vap}}{dt} - \frac{dN_{absorbed}}{dt} - \frac{dN_{leak}}{dt}\right]k_BT \tag{25}$$

$$V_{tot}\frac{dP}{dt} = \left[\frac{1}{4}v_{RMS}\frac{P_{vap}}{k_BT}A_{tot} - \frac{1}{4}v_{RMS}\frac{P}{k_BT}A_{tot} - \frac{1}{4}v_{RMS}\frac{P-P_{vac}}{k_BT}A_{ap}\right]k_BT \tag{26}$$

Assume $P_{vac} \approx 0$ for now. A_{tot} is the internal surface area of the crucible plus the area of the sample, A_{ap} is the effective area of the calibrated leak. V_{tot} is the internal volume of the crucible. P_{vap} is the vapor pressure of the SiC, which is known from work by Lilov[129].

$$V_{tot}\frac{dP}{dt} = \frac{1}{4}v_{RMS}\Big[P_{vap}A_{tot} - P(A_{tot} + A_{ap})\Big] \tag{27}$$

Taking $P(t=0) = 0$ and integrating to get:

$$P(t) = \frac{P_{vap}A_{tot}}{A_{tot} - A_{ap}}(1 - e^{-\frac{t}{t_0}}) \tag{28}$$

$$t_0 = \frac{4V_{tot}}{v_{RMS}(A_{tot} - A_{ap})} \tag{29}$$

Pressure equilibration is the balance of volume to surface area ratio along with the thermal speed of the gas. Note that for $A_{tot} >> A_{ap}$ the gas pressure is independent of the sample surface area.

For a typical $3.5\times4.5\text{mm}^2$ sample in a crucible with inner diameter 4.6mm and length 10mm, grown at 1480°C, assuming $A_{tot} >> A_{ap}$, we have $t_0 = 5\mu$s. Pressure equilibrates very quickly, and ultimately doesn't depend on the number or size of the samples for small leaks.

REFERENCES

[1] "The international technology roadmap for semiconductors." http://www.itrs.net/reports.html, 2013.

[2] C. Beenakker and H. van Houten, "Quantum transport in semiconductor nanostructures," in *Semiconductor Heterostructures and Nanostructures* (H. Ehrenreich and D. Turnbull, eds.), vol. 44 of *Solid State Physics*, pp. 1 – 228, Academic Press, 1991.

[3] Z. Ren, Y. Lan, and Y. Wang, *Aligned Carbon Nanotubes*. Springer, 2013.

[4] H. W. Kroto, J. R. Heath, S. C. O'Brien, R. F. Curl, and R. E. Smalley, "C60: Buckminsterfullerene," *Nature*, vol. 318, pp. 162–163, Nov. 1985.

[5] S. Iijima, "Helical microtubules of graphitic carbon," *Nature*, vol. 354, pp. 56–58, Nov. 1991.

[6] B. T. Kelly, *Physics of Graphite*. Applied Science Publishers, 1981.

[7] L. Pauling, "The structure and properties of graphite and boron nitride," *Proceedings of the National Academy of Sciences*, vol. 56, no. 6, pp. 1646–1652, 1966.

[8] P. R. Wallace, "The band theory of graphite," *Phys. Rev.*, vol. 71, pp. 622–634, May 1947.

[9] C. Hwang, D. A. Siegel, S.-K. Mo, W. Regan, A. Ismach, Y. Zhang, A. Zettl, and A. Lanzara, "Fermi velocity engineering in graphene by substrate modification," *Sci. Rep.*, vol. 2, Aug. 2012.

[10] P. L. McEuen, M. Bockrath, D. H. Cobden, Y.-G. Yoon, and S. G. Louie, "Disorder, pseudospins, and backscattering in carbon nanotubes," *Phys. Rev. Lett.*, vol. 83, pp. 5098–5101, Dec 1999.

[11] T. Ando and T. Nakanishi, "Impurity scattering in carbon nanotubes absence of back scattering ," *Journal of the Physical Society of Japan*, vol. 67, no. 5, pp. 1704–1713, 1998.

[12] X. Wu, X. Li, Z. Song, C. Berger, and W. A. de Heer, "Weak antilocalization in epitaxial graphene: Evidence for chiral electrons," *Phys. Rev. Lett.*, vol. 98, p. 136801, Mar 2007.

[13] S. Das Sarma, S. Adam, E. H. Hwang, and E. Rossi, "Electronic transport in two-dimensional graphene," *Rev. Mod. Phys.*, vol. 83, pp. 407–470, May 2011.

[14] N. Ashcroft and N. Mermin, *Solid State Physics*. Philadelphia: Saunders College, 1976.

[15] D. K. Schroder, *Semiconductor Material and Device Characterization*. Wiley-Interscience, 2006.

[16] S. M. Sze, *Semiconductor Devices - Physics and Technology*. McGraw-Hill New York, 1985.

[17] S. Datta, *Electronic Transport In Mesoscopic Systems*. New York, NY: Cambridge, 1995.

[18] M. Y. Han, J. C. Brant, and P. Kim, "Electron transport in disordered graphene nanoribbons," *Phys. Rev. Lett.*, vol. 104, p. 056801, Feb 2010.

[19] Y. Yang and R. Murali, "Impact of size effect on graphene nanoribbon transport," *Electron Device Letters, IEEE*, vol. 31, pp. 237–239, March 2010.

[20] Y. Yang, L.-I. Huang, Y. Fukuyama, F.-H. Liu, M. A. Real, P. Barbara, C.-T. Liang, D. B. Newell, and R. E. Elmquist, "Low Carrier Density Epitaxial Graphene Devices On SiC," *ArXiv*, Apr. 2014.

[21] E. Pallecchi, F. Lafont, V. Cavaliere, F. Schopfer, D. Mailly, W. Poirier, and A. Ouerghi, "High electron mobility in epitaxial graphene on 4h-SiC(0001) via post-growth annealing under hydrogen," *Sci. Rep.*, vol. 4, Apr. 2014.

[22] H. Boehm, A. Clauss, U. Hofmann, and F. G, "Dunnste kohlenstof-folien," *Z Naturforsch Pt B*, vol. 17, pp. 150–153, 1962.

[23] C. Berger, Z. Song, T. Li, X. Li, A. Y. Ogbazghi, R. Feng, Z. Dai, A. N. Marchenkov, E. H. Conrad, P. N. First, and W. A. de Heer, "Ultrathin epitaxial graphite: 2d electron gas properties and a route toward graphene-based nanoelectronics," *The Journal of Physical Chemistry B*, vol. 108, no. 52, pp. 19912–19916, 2004.

[24] K. S. Novoselov, A. K. Geim, S. V. Morozov, D. Jiang, Y. Zhang, S. V. Dubonos, I. V. Grigorieva, and A. A. Firsov, "Electric field effect in atomically thin carbon films," *Science*, vol. 306, no. 5696, pp. 666–669, 2004.

[25] K. Bolotin, K. Sikes, Z. Jiang, M. Klima, G. Fudenberg, J. Hone, P. Kim, and H. Stormer, "Ultrahigh electron mobility in suspended graphene," *Solid State Communications*, vol. 146, no. 910, pp. 351 – 355, 2008.

[26] H. Zhou, W. J. Yu, L. Liu, R. Cheng, Y. Chen, X. Huang, Y. Liu, Y. Wang, Y. Huang, and X. Duan, "Chemical vapour deposition growth of large single crystals of monolayer and bilayer graphene," *Nat Commun*, vol. 4, June 2013.

[27] DeanC. R., YoungA. F., MericI., LeeC., WangL., SorgenfreiS., WatanabeK., TaniguchiT., KimP., ShepardK. L., and HoneJ., "Boron nitride substrates for high-quality graphene electronics," *Nat Nano*, vol. 5, pp. 722–726, Oct. 2010.

[28] K. I. Bolotin, F. Ghahari, M. D. Shulman, H. L. Stormer, and P. Kim, "Observation of the fractional quantum hall effect in graphene," *Nature*, vol. 462, pp. 196–199, Nov. 2009.

[29] Y. Wang, X. Tong, X. Guo, Y. Wang, G. Jin, and X. Guo, "Large scale production of highly-qualified graphene by ultrasonic exfoliation of expanded graphite under the promotion of (nh 4) 2 co 3 decomposition," *Nanotechnology*, vol. 24, no. 47, p. 475602, 2013.

[30] N. R. Gall, E. V. Rut'kov, and A. Y. Tontegode, "Two dimensional graphite films on metals and their intercalation," *International Journal of Modern Physics B*, vol. 11, no. 16, pp. 1865–1911, 1997.

[31] Q. Yu, J. Lian, S. Siriponglert, H. Li, Y. P. Chen, and S.-S. Pei, "Graphene segregated on ni surfaces and transferred to insulators," *Applied Physics Letters*, vol. 93, no. 11, pp. –, 2008.

[32] K. S. Kim, Y. Zhao, H. Jang, S. Y. Lee, J. M. Kim, K. S. Kim, J.-H. Ahn, P. Kim, J.-Y. Choi, and B. H. Hong, "Large-scale pattern growth of graphene films for stretchable transparent electrodes," *Nature*, vol. 457, pp. 706–710, Feb. 2009.

[33] A. Reina, X. Jia, J. Ho, D. Nezich, H. Son, V. Bulovic, M. S. Dresselhaus, and J. Kong, "Large area, few-layer graphene films on arbitrary substrates by chemical vapor deposition," *Nano Letters*, vol. 9, no. 1, pp. 30–35, 2009. PMID: 19046078.

[34] X. Li, W. Cai, J. An, S. Kim, J. Nah, D. Yang, R. Piner, A. Velamakanni, I. Jung, E. Tutuc, S. K. Banerjee, L. Colombo, and R. S. Ruoff, "Large-area synthesis of high-quality and uniform graphene films on copper foils," *Science*, vol. 324, no. 5932, pp. 1312–1314, 2009.

[35] G. Ruan, Z. Sun, Z. Peng, and J. M. Tour, "Growth of graphene from food, insects, and waste," *ACS Nano*, vol. 5, no. 9, pp. 7601–7607, 2011. PMID: 21800842.

[36] A. Reina, H. Son, L. Jiao, B. Fan, M. S. Dresselhaus, Z. Liu, and J. Kong, "Transferring and identification of single- and few-layer graphene on arbitrary substrates," *The Journal of Physical Chemistry C*, vol. 112, no. 46, pp. 17741–17744, 2008.

[37] E. Acheson, "Deflocculated graphite," *Journal Of The Franklin Institute*, vol. 164, pp. 0375–0382, 1907.

[38] A. V. Bommel, J. Crombeen, and A. V. Tooren, "{LEED} and auger electron observations of the sic(0001) surface," *Surface Science*, vol. 48, no. 2, pp. 463 – 472, 1975.

[39] I. Forbeaux, J.-M. Themlin, and J.-M. Debever, "Heteroepitaxial graphite on $6h-\mathrm{SiC}(0001)$: interface formation through conduction-band electronic structure," *Phys. Rev. B*, vol. 58, pp. 16396–16406, Dec 1998.

[40] C. Berger, Z. Song, X. Li, X. Wu, N. Brown, C. Naud, D. Mayou, T. Li, J. Hass, A. N. Marchenkov, E. H. Conrad, P. N. First, and W. A. de Heer, "Electronic confinement and coherence in patterned epitaxial graphene," *Science*, vol. 312, no. 5777, pp. 1191–1196, 2006.

[41] K. V. Emtsev, A. Bostwick, K. Horn, J. Jobst, G. L. Kellogg, L. Ley, J. L. McChesney, T. Ohta, S. A. Reshanov, J. Rohrl, E. Rotenberg, A. K. Schmid, D. Waldmann, H. B. Weber, and T. Seyller, "Towards wafer-size graphene layers by atmospheric pressure graphitization of silicon carbide," *Nat Mater*, vol. 8, pp. 203–207, Mar. 2009.

[42] R. Dong, Z. Guo, J. Palmer, Y. Hu, M. Ruan, J. Hankinson, J. Kunc, S. K. Bhattacharya, C. Berger, and W. A. de Heer, "Wafer bonding solution to epitaxial graphenesilicon integration," *Journal of Physics D: Applied Physics*, vol. 47, no. 9, p. 094001, 2014.

[43] J. Kunc, Y. Hu, J. Palmer, Z. Guo, J. Hankinson, S. H. Gamal, C. Berger, and W. A. de Heer, "Planar edge schottky barrier-tunneling transistors using epitaxial graphene/sic junctions," *Nano Letters*, vol. 14, no. 9, pp. 5170–5175, 2014. PMID: 25115623.

[44] F. Krach, S. Hertel, D. Waldmann, J. Jobst, M. Krieger, S. Reshanov, A. Schner, and H. B. Weber, "A switch for epitaxial graphene electronics: Utilizing the silicon carbide substrate as transistor channel," *Applied Physics Letters*, vol. 100, no. 12, pp. –, 2012.

[45] B. Dlubak, M.-B. Martin, C. Deranlot, B. Servet, S. Xavier, R. Mattana, M. Sprinkle, C. Berger, W. A. De Heer, F. Petroff, A. Anane, P. Seneor, and A. Fert, "Highly efficient spin transport in epitaxial graphene on SiC," *Nat Phys*, vol. 8, pp. 557–561, July 2012.

[46] J.-S. Moon, D. Curtis, S. Bui, M. Hu, D. Gaskill, J. Tedesco, P. Asbeck, G. Jernigan, B. L. VanMil, R. L. Myers-Ward, J. Eddy, C.R., P. Campbell, and X. Weng, "Top-gated epitaxial graphene fets on si-face sic wafers with a peak transconductance of 600 ms/mm," *Electron Device Letters, IEEE*, vol. 31, pp. 260–262, April 2010.

[47] Y.-M. Lin, A. Valdes-Garcia, S.-J. Han, D. B. Farmer, I. Meric, Y. Sun, Y. Wu, C. Dimitrakopoulos, A. Grill, P. Avouris, and K. A. Jenkins, "Wafer-scale graphene integrated circuit," *Science*, vol. 332, no. 6035, pp. 1294–1297, 2011.

[48] S. E. Saddow and A. Agarwal, *Advances in Silicon Carbide Processing and Applications*. Artech House, Inc., 2004.

[49] F. Ming, *Theoretical studies of the epitaxial growth of graphene*. PhD thesis, Georgia Institute of Technology, 2011.

[50] J. Hass, W. A. de Heer, and E. H. Conrad, "The growth and morphology of epitaxial multilayer graphene," *Journal of Physics: Condensed Matter*, vol. 20, no. 32, p. 323202, 2008.

[51] Sprinkle M., Ruan M., Hu Y., Hankinson J., Rubio-Roy M., Zhang B., Wu X., Berger C., and de Heer W. A., "Scalable templated growth of graphene nanoribbons on SiC," *Nat Nano*, vol. 5, pp. 727–731, Oct. 2010.

[52] J. Hicks, A. Tejeda, A. Taleb-Ibrahimi, M. S. Nevius, F. Wang, K. Shepperd, J. Palmer, F. Bertran, P. Le Fevre, J. Kunc, W. A. de Heer, C. Berger, and E. H. Conrad, "A wide-bandgap metal-semiconductor-metal nanostructure made entirely from graphene," *Nat Phys*, vol. 9, pp. 49–54, Jan. 2013.

[53] T. Shen, J. J. Gu, M. Xu, Y. Q. Wu, M. L. Bolen, M. A. Capano, L. W. Engel, and P. D. Ye, "Observation of quantum-hall effect in gated epitaxial graphene grown on sic (0001)," *Applied Physics Letters*, vol. 95, no. 17, pp. –, 2009.

[54] X. Wu, Y. Hu, M. Ruan, N. K. Madiomanana, J. Hankinson, M. Sprinkle, C. Berger, and W. A. de Heer, "Half integer quantum hall effect in high mobility single layer epitaxial graphene," *Applied Physics Letters*, vol. 95, no. 22, pp. –, 2009.

[55] M. Sprinkle, D. Siegel, Y. Hu, J. Hicks, A. Tejeda, A. Taleb-Ibrahimi, P. Le Fèvre, F. Bertran, S. Vizzini, H. Enriquez, S. Chiang, P. Soukiassian, C. Berger, W. A. de Heer, A. Lanzara, and E. H. Conrad, "First direct observation of a nearly ideal graphene band structure," *Phys. Rev. Lett.*, vol. 103, p. 226803, Nov 2009.

[56] M. Sprinkle, J. Hicks, A. Tejeda, A. Taleb-Ibrahimi, P. L. Fvre, F. Bertran, H. Tinkey, M. C. Clark, P. Soukiassian, D. Martinotti, J. Hass, and E. H. Conrad, "Multilayer epitaxial graphene grown on the (SiC $000\bar{1}$) surface; structure and electronic properties," *Journal of Physics D: Applied Physics*, vol. 43, no. 37, p. 374006, 2010.

[57] D. L. Miller, K. D. Kubista, G. M. Rutter, M. Ruan, W. A. de Heer, P. N. First, and J. A. Stroscio, "Structural analysis of multilayer graphene via atomic moiré interferometry," *Phys. Rev. B*, vol. 81, p. 125427, Mar 2010.

[58] Y. Hu, *Production and properties of epitaxial graphene on the carbon terminated face of hexagonal silicon carbide*. PhD thesis, Georgia Institute of Technology, 2013.

[59] P. N. First, W. A. de Heer, T. Seyller, C. Berger, J. A. Stroscio, and J.-S. Moon, "Epitaxial graphenes on silicon carbide," *MRS Bulletin*, vol. 35, pp. 296–305, 4 2010.

[60] Z. Guo, R. Dong, P. S. Chakraborty, N. Lourenco, J. Palmer, Y. Hu, M. Ruan, J. Hankinson, J. Kunc, J. D. Cressler, C. Berger, and W. A. de Heer, "Record maximum oscillation frequency in c-face epitaxial graphene transistors," *Nano Letters*, vol. 13, no. 3, pp. 942–947, 2013.

[61] J. Ristein, S. Mammadov, and T. Seyller, "Origin of doping in quasi-free-standing graphene on silicon carbide," *Phys. Rev. Lett.*, vol. 108, p. 246104, Jun 2012.

[62] R. S. Nasyrov, V. M. Lopatin, and B. S. Lunin, "Optical transmission and internal friction in fused quartz melted from natural raw materials," *Mendeleev Communications*, vol. 22, no. 6, pp. 334 – 335, 2012.

[63] V. Ramachandran, M. Brady, A. Smith, R. Feenstra, and D. Greve, "Preparation of atomically flat surfaces on silicon carbide using hydrogen etching," *Journal of Electronic Materials*, vol. 27, no. 4, pp. 308–312, 1998.

[64] M. H. Oliveira, T. Schumann, M. Ramsteiner, J. M. J. Lopes, and H. Riechert, "Influence of the silicon carbide surface morphology on the epitaxial graphene formation," *Applied Physics Letters*, vol. 99, no. 11, pp. –, 2011.

[65] L. Malard, M. Pimenta, G. Dresselhaus, and M. Dresselhaus, "Raman spectroscopy in graphene," *Physics Reports*, vol. 473, no. 56, pp. 51 – 87, 2009.

[66] A. C. Ferrari, J. C. Meyer, V. Scardaci, C. Casiraghi, M. Lazzeri, F. Mauri, S. Piscanec, D. Jiang, K. S. Novoselov, S. Roth, and A. K. Geim, "Raman spectrum of graphene and graphene layers," *Phys. Rev. Lett.*, vol. 97, p. 187401, Oct 2006.

[67] C. Faugeras, A. Nerrire, M. Potemski, A. Mahmood, E. Dujardin, C. Berger, and W. A. de Heer, "Few-layer graphene on sic, pyrolitic graphite, and graphene: A raman scattering study," *Applied Physics Letters*, vol. 92, no. 1, pp. –, 2008.

[68] J. Kunc, Y. Hu, J. Palmer, C. Berger, and W. A. de Heer, "A method to extract pure raman spectrum of epitaxial graphene on sic," *Applied Physics Letters*, vol. 103, no. 20, pp. –, 2013.

[69] P. Girard, "Electrostatic force microscopy: principles and some applications to semiconductors," *Nanotechnology*, vol. 12, no. 4, p. 485, 2001.

[70] V. Panchal, R. Pearce, R. Yakimova, A. Tzalenchuk, and O. Kazakova, "Standardization of surface potential measurements of graphene domains," *Sci. Rep.*, vol. 3, Sept. 2013.

[71] B. Nikolić and P. B. Allen, "Electron transport through a circular constriction," *Phys. Rev. B*, vol. 60, pp. 3963–3969, Aug 1999.

[72] Z. Ye, H. Moon, M. H. Lee, and A. Martini, "Size and load dependence of nanoscale electric contact resistance," *Tribology International*, vol. 71, no. 0, pp. 109 – 113, 2014.

[73] A. G. Emslie, F. T. Bonner, and L. G. Peck, "Flow of a viscous liquid on a rotating disk," *Journal of Applied Physics*, vol. 29, no. 5, 1958.

[74] C. Mack, *Fundamental Principles of Optical Lithography: The Science of Microfabrication.* Wiley-Interscience.

[75] J. E. Mahan, *Physical vapor deposition of thin films.* New York, NY: Wiley, 2000.

[76] J. D. Hicks, *A combined top-down/bottom-up route to fabricating graphene devices.* PhD thesis, Georgia Institute of Technology, 2013.

[77] D. E. Bradley, "Evaporated carbon films for use in electron microscopy," *Br J Appl Phys*, vol. 5, pp. 65–66, 1954.

[78] A. C. Ferrari, B. Kleinsorge, N. A. Morrison, A. Hart, V. Stolojan, and J. Robertson, "Stress reduction and bond stability during thermal annealing of tetrahedral amorphous carbon," *Journal of Applied Physics*, vol. 85, no. 10, 1999.

[79] K. Takai, M. Oga, H. Sato, T. Enoki, Y. Ohki, A. Taomoto, K. Suenaga, and S. Iijima, "Structure and electronic properties of a nongraphitic disordered carbon system and its heat-treatment effects," *Phys. Rev. B*, vol. 67, p. 214202, Jun 2003.

[80] L. G. Cançado, K. Takai, T. Enoki, M. Endo, Y. A. Kim, H. Mizusaki, A. Jorio, L. N. Coelho, R. M. aes Paniago, and M. A. Pimenta, "General equation for the determination of the crystallite size l[sub a] of nanographite by raman spectroscopy," *Applied Physics Letters*, vol. 88, no. 16, p. 163106, 2006.

[81] T. Ohta, N. C. Bartelt, S. Nie, K. Thürmer, and G. L. Kellogg, "Role of carbon surface diffusion on the growth of epitaxial graphene on sic," *Phys. Rev. B*, vol. 81, p. 121411, Mar 2010.

[82] F. Ming and A. Zangwill, "Model and simulations of the epitaxial growth of graphene on non-planar 6hsic surfaces," *Journal of Physics D: Applied Physics*, vol. 45, no. 15, p. 154007, 2012.

[83] H. Fukidome, Y. Kawai, F. Fromm, M. Kotsugi, H. Handa, T. Ide, T. Ohkouchi, H. Miyashita, Y. Enta, T. Kinoshita, T. Seyller, and M. Suemitsu, "Precise control of epitaxy of graphene by microfabricating sic substrate," *Applied Physics Letters*, vol. 101, no. 4, pp. –, 2012.

[84] S.-H. Ji, J. B. Hannon, R. M. Tromp, V. Perebeinos, J. Tersoff, and F. M. Ross, "Atomic-scale transport in epitaxial graphene," *Nat Mater*, vol. 11, pp. 114–119, Feb. 2012.

[85] J. Palmer, J. Kunc, Y. Hu, J. Hankinson, Z. Guo, C. Berger, and W. A. de Heer, "Controlled epitaxial graphene growth within removable amorphous carbon corrals," *Applied Physics Letters*, vol. 105, no. 2, pp. –, 2014.

[86] W. A. de Heer, C. Berger, M. Ruan, M. Sprinkle, X. Li, Y. Hu, B. Zhang, J. Hankinson, and E. Conrad, "Large area and structured epitaxial graphene produced by confinement controlled sublimation of silicon carbide," *Proceedings of the National Academy of Sciences*, vol. 108, no. 41, pp. 16900–16905, 2011.

[87] K. V. Emtsev, A. Bostwick, K. Horn, J. Jobst, G. L. Kellogg, L. Ley, J. L. McChesney, T. Ohta, S. A. Reshanov, J. Rohrl, E. Rotenberg, A. K. Schmid, D. Waldmann, H. B. Weber, and T. Seyller, "Towards wafer-size graphene layers by atmospheric pressure graphitization of silicon carbide," *Nat Mater*, vol. 8, pp. 203–207, Mar. 2009.

[88] J. A. Powell, P. G. Neudeck, A. J. Trunek, G. M. Beheim, L. G. Matus, R. W. Hoffman, and L. J. Keys, "Growth of step-free surfaces on device-size (0001)sic mesas," *Applied Physics Letters*, vol. 77, no. 10, 2000.

[89] D. Lee and J. Blakely, "Formation and stability of large step-free areas on si(001) and si(111)," *Surface Science*, vol. 445, no. 1, pp. 32 – 40, 2000.

[90] S. Tanaka, C. C. Umbach, J. M. Blakely, R. M. Tromp, and M. Mankos, "Fabrication of arrays of large stepfree regions on si(001)," *Applied Physics Letters*, vol. 69, no. 9, 1996.

[91] S. Hertel, D. Waldmann, J. Jobst, A. Albert, M. Albrecht, S. Reshanov, A. Schner, M. Krieger, and H. Weber, "Tailoring the graphene/silicon carbide interface for monolithic wafer-scale electronics," *Nat Commun*, vol. 3, p. 957, July 2012.

[92] F. Fromm, M. H. O. Jr, A. Molina-Snchez, M. Hundhausen, J. M. J. Lopes, H. Riechert, L. Wirtz, and T. Seyller, "Contribution of the buffer layer to the raman spectrum of epitaxial graphene on sic(0001)," *New Journal of Physics*, vol. 15, no. 4, p. 043031, 2013.

[93] A. Tiberj, J. R. Huntzinger, N. Camara, P. Godignon, and J. Camassel, "Raman spectrum and optical extinction of graphene buffer layers on the Si-face of 6H-SiC," *ArXiv*, Dec. 2012.

[94] V. Borovikov and A. Zangwill, "Step bunching of vicinal 6h-SiC0001 surfaces," *Phys. Rev. B*, vol. 79, p. 245413, Jun 2009.

[95] J. Baringhaus, M. Ruan, F. Edler, A. Tejeda, M. Sicot, Taleb-IbrahimiAmina, A.-P. Li, Z. Jiang, E. H. Conrad, C. Berger, C. Tegenkamp, and W. A. de Heer, "Exceptional ballistic transport in epitaxial graphene nanoribbons," *Nature*, vol. 506, pp. 349–354, Feb. 2014.

[96] F. Xia, V. Perebeinos, Y.-m. Lin, Y. Wu, and P. Avouris, "The origins and limits of metal-graphene junction resistance," *Nat Nano*, vol. 6, pp. 179–184, Mar. 2011.

[97] J. Jobst, D. Waldmann, F. Speck, R. Hirner, D. K. Maude, T. Seyller, and H. B. Weber, "Quantum oscillations and quantum hall effect in epitaxial graphene," *Phys. Rev. B*, vol. 81, p. 195434, May 2010.

[98] M. Rubio-Roy, F. Zaman, Y. Hu, C. Berger, M. W. Moseley, J. D. Meindl, and W. A. de Heer, "Structured epitaxial graphene growth on sic by selective graphitization using a patterned aln cap," *Applied Physics Letters*, vol. 96, no. 8, pp. –, 2010.

[99] R. Puybaret, J. Hankinson, A. Ougazzaden, P. L. Voss, C. Berger, and W. A. de Heer, "Local tuning of graphene thickness on 4H-SiC C-face using decomposing silicon nitride masks," *ArXiv*, July 2013.

[100] K. Nakada, M. Fujita, G. Dresselhaus, and M. S. Dresselhaus, "Edge state in graphene ribbons: Nanometer size effect and edge shape dependence," *Phys. Rev. B*, vol. 54, pp. 17954–17961, Dec 1996.

[101] P. Gallagher, K. Todd, and D. Goldhaber-Gordon, "Disorder-induced gap behavior in graphene nanoribbons," *Phys. Rev. B*, vol. 81, p. 115409, Mar 2010.

[102] S. Frank, P. Poncharal, Z. L. Wang, and W. A. d. Heer, "Carbon nanotube quantum resistors," *Science*, vol. 280, no. 5370, pp. 1744–1746, 1998.

[103] Y. Hu, M. Ruan, Z. Guo, R. Dong, J. Palmer, J. Hankinson, C. Berger, and W. A. de Heer, "Structured epitaxial graphene: growth and properties," *Journal of Physics D: Applied Physics*, vol. 45, no. 15, p. 154010, 2012.

[104] M. Ruan, *Structured Epitaxial Graphene for Electronics*. PhD thesis, Georgia Institute of Technology, 2012.

[105] A. M. Goossens, V. E. Calado, A. Barreiro, K. Watanabe, T. Taniguchi, and L. M. K. Vandersypen, "Mechanical cleaning of graphene," *Applied Physics Letters*, vol. 100, no. 7, pp. –, 2012.

[106] H. Tinkey and C. Berger, "Unpublished graphene humidity effect experiment." 2009.

[107] R. de Picciotto, H. L. Stormer, L. N. Pfeiffer, K. W. Baldwin, and K. W. West, "Four-terminal resistance of a ballistic quantum wire," *Nature*, vol. 411, pp. 51–54, May 2001.

[108] S. Niyogi, E. Bekyarova, M. E. Itkis, H. Zhang, K. Shepperd, J. Hicks, M. Sprinkle, C. Berger, C. N. Lau, W. A. deHeer, E. H. Conrad, and R. C. Haddon, "Spectroscopy of covalently functionalized graphene," *Nano Letters*, vol. 10, no. 10, pp. 4061–4066, 2010. PMID: 20738114.

[109] R. Balog, B. Jorgensen, L. Nilsson, M. Andersen, E. Rienks, M. Bianchi, M. Fanetti, E. Laegsgaard, A. Baraldi, S. Lizzit, Z. Sljivancanin, F. Besenbacher, B. Hammer, T. G. Pedersen, P. Hofmann, and L. Hornekaer, "Bandgap opening in graphene induced by patterned hydrogen adsorption," *Nat Mater*, vol. 9, pp. 315–319, Apr. 2010.

[110] RadisavljevicB., RadenovicA., BrivioJ., GiacomettiV., and KisA., "Single-layer MoS2 transistors," *Nat Nano*, vol. 6, pp. 147–150, Mar. 2011.

[111] A. Bostwick, J. McChesney, T. Ohta, E. Rotenberg, T. Seyller, and K. Horn, "Experimental studies of the electronic structure of graphene," *Progress in Surface Science*, vol. 84, no. 1112, pp. 380 – 413, 2009.

[112] S. Goler, C. Coletti, V. Piazza, P. Pingue, F. Colangelo, V. Pellegrini, K. V. Emtsev, S. Forti, U. Starke, F. Beltram, and S. Heun, "Revealing the atomic structure of the buffer layer between sic(0001) and epitaxial graphene," *Carbon*, vol. 51, no. 0, pp. 249 – 254, 2013.

[113] C. Riedl, C. Coletti, T. Iwasaki, A. A. Zakharov, and U. Starke, "Quasi-free-standing epitaxial graphene on sic obtained by hydrogen intercalation," *Phys. Rev. Lett.*, vol. 103, p. 246804, Dec 2009.

[114] M. H. O. Jr., T. Schumann, F. Fromm, R. Koch, M. Ostler, M. Ramsteiner, T. Seyller, J. M. J. Lopes, and H. Riechert, "Formation of high-quality quasi-free-standing bilayer graphene on sic(0001) by oxygen intercalation upon annealing in air," *Carbon*, vol. 52, no. 0, pp. 83 – 89, 2013.

[115] J. Hass, J. E. Millán-Otoya, P. N. First, and E. H. Conrad, "Interface structure of epitaxial graphene grown on 4h-sic(0001)," *Phys. Rev. B*, vol. 78, p. 205424, Nov 2008.

[116] G. Sclauzero and A. Pasquarello, "Carbon rehybridization at the graphene/sic(0001) interface: Effect on stability and atomic-scale corrugation," *Phys. Rev. B*, vol. 85, p. 161405, Apr 2012.

[117] S.-H. Lee, H.-J. Chung, J. Heo, H. Yang, J. Shin, U.-I. Chung, and S. Seo, "Band gap opening by two-dimensional manifestation of peierls instability in graphene," *ACS Nano*, vol. 5, no. 4, pp. 2964–2969, 2011. PMID: 21405129.

[118] W. Norimatsu and M. Kusunoki, "Formation process of graphene on sic (0001)," *Physica E: Low-dimensional Systems and Nanostructures*, vol. 42, no. 4, pp. 691 – 694, 2010. 18th International Conference on Electron Properties of Two-Dimensional Systems.

[119] I. Palacio, A. Celis, M. N. Nair, A. Gloter, A. Zobelli, M. Sicot, D. Malterre, M. S. Nevius, C. Berger, W. A. de Heer, E. H. Conrad, A. Taleb-Ibrahimi, and A. Tejeda, "Atomic structure in armchair graphene nanoribbons and quantum confinement gap opening." 2014.

[120] F. Giannazzo, I. Deretzis, G. Nicotra, G. Fisichella, Q. Ramasse, C. Spinella, F. Roccaforte, and A. L. Magna, "High resolution study of structural and electronic properties of epitaxial graphene grown on off-axis 4hsic (0001)," *Journal of Crystal Growth*, vol. 393, no. 0, pp. 150 – 155, 2014.

[121] H. Yang, J. Heo, S. Park, H. J. Song, D. H. Seo, K.-E. Byun, P. Kim, I. Yoo, H.-J. Chung, and K. Kim, "Graphene barristor, a triode device with a gate-controlled schottky barrier," *Science*, vol. 336, no. 6085, pp. 1140–1143, 2012.

[122] J. Palmer, J. Hankinson, and C. Berger, "Unpublished transport measurement of SiC annealed at 2000°C." 2012.

[123] D. V. Geppert, "Spacechargelimited tunnel emission into an insulating film," *Journal of Applied Physics*, vol. 33, no. 10, 1962.

[124] C. Zeng, E. B. Song, M. Wang, S. Lee, C. M. Torres, J. Tang, B. H. Weiller, and K. L. Wang, "Vertical graphene-base hot-electron transistor," *Nano Letters*, vol. 13, no. 6, pp. 2370–2375, 2013. PMID: 23668939.

[125] Y. Zhang, Y. Gao, L. Liu, N. Xi, Y. Wang, L. Ma, Z. Dong, and U. C. Wejinya, "Cutting forces related with lattice orientations of graphene using an atomic force microscopy based nanorobot," *Applied Physics Letters*, vol. 101, no. 21, pp. –, 2012.

[126] R. K. Puddy, P. H. Scard, D. Tyndall, M. R. Connolly, C. G. Smith, G. A. C. Jones, A. Lombardo, A. C. Ferrari, and M. R. Buitelaar, "Atomic force microscope nanolithography of graphene: Cuts, pseudocuts, and tip current measurements," *Applied Physics Letters*, vol. 98, no. 13, pp. –, 2011.

[127] J. Oh and D. Ahn, "Klein tunneling through an oblique barrier in graphene ribbons," *Journal of the Korean Physical Society*, vol. 59, no. 4, pp. 2786 – 2791, 2011.

[128] Q.-w. Shi, Z.-f. Wang, Q.-x. Li, and J.-l. Yang, "Chiral selective tunneling induced graphene nanoribbon switch," *Frontiers of Physics in China*, vol. 4, no. 3, pp. 373–377, 2009.

[129] S. Lilov, "Study of the equilibrium processes in the gas phase during silicon carbide sublimation," *Materials Science and Engineering: B*, vol. 21, no. 1, pp. 65 – 69, 1993.

VITA

James Matthew Palmer was born in Plano, Texas in 1988. His childhood was spent on a farm near Leonard, Texas. He enjoys figuring out things, and there he learned how many things work and how these things are built. His interest in radio electronics eventually led him to want to learn how transistors work. Having not known about physics and seeing Maxwell's equations, he "got it." There he stumbled upon the great beauty of physics, and he wanted to see more. The study of physics led to him towards understanding transistors, and eventually towards seeking new processes for producing transistors. After earning a bachelors degree in physics from Texas A&M University in 2009, he joined the Epitaxial Graphene Group at Georgia Tech to further his goal. He will now learn about integration of transistors by working in the semiconductor industry.